In-silico clinical trials for assessment of intracranial flow diverters

Ali Sarrami Foroushani

A thesis submitted in partial fulfilment of the requirements for the degree of

Doctor of Philosophy (PhD)

2018

In-silico clinical trials for assessment of intracranial
flow diverters

Ali Sarrami Foroushani

Department of Electronic and Electrical Engineering
The University of Sheffield

A thesis submitted in partial fulfilment of the requirements for the degree of

Doctor of Philosophy (PhD)

March, 2019

To my parents and sister

Abstract

In-silico trials refer to pre-clinical trials performed, entirely or in part, using individualised computer models that simulate some aspect of drug effect, medical device, or clinical intervention. Such virtual trials reduce and optimise animal and clinical trials, and enable exploring a wider range of anatomies and physiologies. In the context of endovascular treatment of intracranial aneurysms, *in-silico* trials can be used to evaluate the effectiveness of endovascular devices over virtual populations of patients with different aneurysm morphologies and physiologies. However, this requires (i) a virtual endovascular treatment model to evaluate device performance based on a reliable performance indicator, (ii) models that represent intra- and inter-subject variations of a virtual population, and (iii) creation of cost-effective and fully-automatic workflows to enable a large number of simulations at a reasonable computational cost and time.

Flow-diverting stents have been proven safe and effective in the treatment of large wide-necked intracranial aneurysms. The presented thesis aims to provide the ingredient models of a workflow for *in-silico* trials of flow-diverting stents and to enhance the general knowledge of how the ingredient models can be streamlined and accelerated to allow large-scale trials. This work contributed to the following aspects: 1) To understand the key ingredient models of a virtual treatment workflow for evaluation of the flow-diverter performance. 2) To understand the effect of input uncertainty and variability on the workflow outputs, 3) To develop generative statistical models that describe variability in internal carotid artery flow waveforms, and investigate the effect of uncertainties on quantification of aneurysmal wall shear stress, 4) As part of a metric to evaluate success of flow diversion, to develop and validate a thrombosis model to assess FD-induced clot stability, and 5) To understand how a fully-automatic aneurysm flow modelling workflow can be built and how computationally inexpensive models can reduce the computational costs.

Acknowledgement

I would like to express my gratitude to my supervisors Prof. Alejandro F. Frangi and Dr. Toni Lassila for providing me the opportunity to work in an ambitious research group, advising me throughout the years, and giving me lessons that go far beyond the scientific research.

Thanks to Dr. Jose M. Pozo and Dr. Ali Gooya that collaborated to the MICCAI paper. Thanks to Dr. Sanjoy Nagaraja and Mr. Andrew Bacon for providing clinical insight into my research. To Dr. Arjan Geers for his invaluable advice and supports at different stages of my PhD life. Special thanks to Dr. M. Shakiba for encouraging me to get into this field of research and the several discussions we had on the clinical aspects of this research. I also thank the software development team at CISTIB, particularly Mr. Milton Hoz de Vila for all the support in using computational tools and resources, and the MULTIX platform.

iv

DECLARATION

Hereby, I (Ali Sarrami Foroushani) affirm that the thesis is the result of my own work and includes nothing which is the outcome of work done in collaboration except as specified in the following.

- The within-subject flow variability model used in Chapter 5, section 5.2, was originally developed by Dr. Toni Lassila. I used the model to generate flow waveforms at rest/exercise states. These waveforms were used as inlet boundary conditions in the subsequent flow simulations. I am the second author of the manuscript that has been written based on this work and is now under review at the Annals of Biomedical Engineering.

- The statistical model used in Chapter 5, section 5.3, was originally developed by Dr. Ali Gooya. I trained the model using wall shear stress (WSS) quantifications obtained from my computational fluid dynamics (CFD) models. Then, I used the trained model to predict aneurysm WSS patterns and compared the predictions to the CFD-based results.

The work presented in this thesis was partially adapted from publications number 1 to 5 of the list presented in Publications section with all permissions acquired. Authorisations from the major contributing co-authors were obtained. Permissions and authorisations are presented at the end of the thesis.

Publications

Journal articles

[1] **Sarrami-Foroushani, A.**; Lassila, T.; Gooya, A.; Geers, A. G.; Frangi, A. F., "Uncertainty quantification of wall shear stress in intracranial aneurysms using a data-driven statistical model of systemic blood flow variability." *Journal of Biomechanics* 49(11):3815-3823, 2016.

[2] **Sarrami-Foroushani, A.**; Lassila, T.; Frangi, A. F., "Virtual endovascular treatment of intracranial aneurysms: models and uncertainty." *Wiley Interdisciplinary Reviews: Systems Biology and Medicine* 9(4):e1385, 2017.

[3] **Sarrami-Foroushani, A.**; Lassila, T.; Hejazi, S. M.; Nagaraja, S.; Bacon, A.; Frangi, A. F., "A computational model for prediction of clot platelet content in flow-diverted intracranial aneurysms." under review, 2018.

[4] Lassila, T.; **Sarrami-Foroushani, A.**; Hejazi, S. M.; Frangi, A. F., "Population-Specific Flow Modelling: Between/Within-Subject Variability in the Internal Carotid Arteries of Elderly Volunteers." under review, 2018.

Peer-reviewed international conferences

[5] **Sarrami-Foroushani, A.**; Lassila, T.; Pozo, J. M.; Gooya, A.; Frangi, A. F., "Direct Estimation of Wall Shear Stress from Aneurysmal Morphology: A Statistical Approach." *International Conference on Medical Image Computing and Computer-Assisted Intervention (MICCAI)* pp. 201-209, 2016

Conference abstracts

[6] **Sarrami-Foroushani, A.**; Lassila, T.; Frangi, A. F., "Modelling the effect of flow variability on intracranial aneurysms with Gaussian processes and lumped parameter models." *8th World Congress of Biomechanics, Dublin, Ireland*, 2018

[7] Lassila, T.; **Sarrami-Foroushani, A.**; Frangi, A. F., "Modelling of Red and White Thrombus Formation in Intracranial Aneurysms After Flow Diversion." *13th World Congress on Computational Mechanics, New York, United States*, 2018

[8] **Sarrami-Foroushani, A.**; Nagaraja, S.; Lassila, T.; Hejazi, S. M.; Bacon, A.; Frangi, A. F., "In-silico flow diversion in intracranial aneurysms: computational prediction of clot platelet content." *British Neurosurgical Research Group Meeting, Sheffield, United Kingdom*, 2018

Contents

List of Figures

xiv

List of Tables

Chapter 1

Introduction

1.1 *In-silico* clinical trials for medical devices

The European medical technologies market in 2014 was estimated at 100 billion with a compound annual growth rate (CAGR) of around 4.5% during the period of 2014-2020 [2, 3]. This was the second largest medical technologies market in the world after the United States [3]. The development and assessment process of medical devices includes: 1) concept definition and preliminary planning, 2) design development and verification through, for example, in-vitro safety tests such as mechanical and biocompatibility tests, 3) design validation stage, where the design is tested for efficacy in animal trials and clinical trials, and, 4) launch and post-market surveillance [2]. In the United States, according to the Food and Drug Administration (FDA) regulations, any medical device that supports or sustains human life, prevents impairment of human health, or presents a potential, unreasonable risk to human is characterised as a *high-risk* device [4, 5]. Manufacturers must obtain a premarket approval (PMA) before marketing high-risk medical devices. Similar pathways are followed by the European regulatory authorities to approve marketing of novel medical devices. The approval processes include all the laboratory and animal testing, and the clinical trials performed in stages three and four [4]. In a survey of over 200 manufacturers [6], a FDA PMA, from the first communication to the final approval, took 54 months on average. For an equivalent device, the European authorities took 11 months to grant a CE mark certification [6]. It was reported that the activities performed as part of the FDA approval account for 79% of the total cost of bringing a product to market [6].

Recent advancements in computer modelling and simulation have drawn attention towards simulation-based trials to reduce and optimise the animal and conventional clinical trials and alleviate the economical, ethical, and environmental issues. *In-silico* clinical trials refer to pre-clinical trials performed, entirely or in part, using individualised computer models that simulate some aspect of drug effect, medical device, or clinical intervention. Such virtual trials reduce and optimise the required animal and clinical trials and lower costs of testing new devices [2]. They enable exploring the performance of devices over a wider range of anatomies and physiologies (e.g., for rare conditions when recruiting large trial populations is impossible). These large-scale trials extend the cohort beyond what would be available with purely patient-specific data collection. In an *in-silico* trial framework, by combining models of anatomy from a real cohort of patients and an inter-subject variability model of physiology, a population of *virtual patients* is generated. It has been acknowledged that virtual patient models must incorporate both patient variability and the model uncertainty to augment clinical trials [7]. A virtual treatment workflow can then deploy the device in the virtual

patients and assess the treatment effectiveness. A detailed description of how the in-gredient models are combined to build an *in-silico* trial space is presented in Chapter 5.

Therefore, in creation of a framework for *in-silico* trials, the first challenge is to develop models of variability and uncertainty and to generate a population of virtual patients that captures inter-/intra-subject variabilities in morphology and physiology of real pathologies. A virtual treatment model should also be developed to simulate different aspects of a treatment and to measure the treatment efficacy in the population of virtual patients. Finally, a large-scale *in-silico* trial includes simultaneous simulation of the treatment in multiple virtual patients and can include computationally expensive processes. Hence, the third challenge is to automate and streamline the ingredient processes as workflows on a computational platform that allows simultaneous execution of several processes (e.g., `MULTIX`[1], `www.multi-x.org`). This is also important to invest in development of computationally inexpensive models to replace costly models and accelerate the trials. The focus of this thesis is to contribute to addressing the above challenges. I demonstrated my developments in an exemplar challenging unmet clinical need: the assessment of the effectiveness of flow-diverting stents in the treatment of intracranial aneurysms.

1.2 Flow diversion of intracranial aneurysms

Intracranial aneurysms are localised pathological dilatations of the intracranial arteries that commonly occur at various locations around the circle of Willis in approximately 5-8% of the general population [8]. Although most aneurysms remain stable through-out the patient's life, their ruptures are associated with high rates of mortality (around 50%) and permanent disability [8]. While the ruptured aneurysms must be immedi-ately treated, unruptured aneurysms present a challenge to the clinicians whether the aneurysm must be treated or only observed. Treatment of these vascular pathologies aims at isolating the aneurysm from the circulatory system and is performed through surgical clipping of the aneurysm neck or endovascular techniques (e.g., coiling, and flow diversion).

Endovascular stents have been used in treatment of intracranial aneurysms since 1990's [9]. This included stents used to assist aneurysm coiling or the use of a sin-gle stent to induce stasis in the sac [9, 10]. High porosity of the intracranial stents,

---

[1]MULTIX is a cross-domain research-oriented platform for accessible, collaborative and reproducible computational and data-intensive analysis. It has been constructed as an engine to enable clinical researchers to collaborate and translate research ideas into products, platforms, and services for the community. It has been designed focusing on three aspects: usability, scalability, and reproducibility.

however, limited the their effectiveness in isolation of the aneurysm [9]. FDs, introduced around 2008 [9, 10, 11], are woven stent-like endovascular devices. Unlike some intracranial stents, FDs have low radial opening force and great metal coverage [9]. Upon deployment in the parent vessel at the aneurysm neck, FDs are expected to reconstruct the parent vessel and redirect flow towards the longitudinal axis of the parent vessel reducing the blood exchange between the aneurysm and the parent vessel [9, 10]. The reduced blood flow in the aneurysm after flow diversion helps to form an occlusive clot in the sac and, ultimately triggers the process of aneurysm healing [9, 10].

SILK and Pipeline Embolisation Device (PED) were the first two flow diverters to receive the CE mark approval in 2008 [10, 11]. However, PED is the only FD approved by the FDA for embolisation of intracranial aneurysms [12]. Since premarket approval of the first-generation PED in 2011, two other generations of this device were introduced [13]. The second-generation PED, called Pipeline Flex Embolisation Device received approvals from the European community and the FDA in 2014 and 2015, respectively [13]. Pipeline Flex allows repositioning and redeployment of the device once implanted [13]. The third-generation of PED, called Pipeline Shield and is the same as Pipeline Flex, but coated with a polymer to reduce its surface thrombogenicity [13]. Pipeline Shield received the CE mark approval in 2015 [13].

In the past decade, flow-diverting stents have shown promise in effective treatment of large/giant and wide-necked aneurysms. The efficacy of FDs has been studied in several clinical studies. Byrne *et al.* [14] reported a complete occlusion rate of 49% in 70 aneurysms treated with SILK flow diverters (9-528 days follow up). In the PUFS study, Becske *et al.* [15] reported the same occlusion rate for 109 aneurysm (3 years follow up). In the FIAT study, Raymond *et al.* [16] reported an occlusion rate of 58% in 75 aneurysms treated with PED and SILK (3-12 months follow up). In a meta-analysis of 29 studies with 1654 aneurysms, Brinjikji *et al.* [17] reported complete occlusion rates of 74% (95% CI, 63%–83%) and 76% (95% CI, 53%–90.0%) for large and giant aneurysms, respectively. In the PARAT study, Liu *et al.* [18] reported an occlusion rate of 75.3% in 82 aneurysms treated with Tubridge flow diverter (6 months follow up). Risk of post-treatment ischaemic and haemorrhagic strokes reported to be approximately 2% and 5%, respectively [9, 14, 18]. Haemorrhagic strokes can be parenchymal or intracerebral haemorrhage (ICH) remote from the aneurysm or subarachnoid haemorrhage (SAH) due to the aneurysm rupture [14]. The SAH rate due to post-FD rupture of the aneurysms was reported to be as high as 8% in giant aneurysms [9, 18].

Despite several studies aimed at assessing FD performance in inducing a complete and stable aneurysm occlusion, there are only two randomised trials reported so far (the PARAT [18] and the FIAT [16] studies) and both trials reported below-expectation

efficacies and high complication rates [18]. More randomised trials are required to better understand mechanisms behind flow diversion success and failure and to determine the true safety and efficacy of FDs [16, 18]. Such trials are costly, include animal testing, and can take years to be performed. As mentioned in Section 1.1, *in-silico* trials can help to alleviate such issues. *In-silico* clinical trials can be part of flow diverters' pre/post-market studies (e.g., randomised clinical trials) to enable comparative investigation of different devices performance in a wider and more comprehensive population of patients. Such virtual trials can accelerate the evolution of flow diverters, that has already taken more than 20 years, and help making new FDs available faster and at a lower cost.

In-silico trials allow *population-specific* optimisation of the treatment procedure (device selection and sizing, level of compaction, anti-coagulant and anti-platelet prescription) and provide insight into the process of clot development after flow diversion. The biological mechanisms of FD-induced thrombosis and aneurysm healing, and the underlying mechanisms of complications like delayed post-FD aneurysm rupture are not fully understood [19]. While conventional clinical trials are limited in answering *why* failures happen, virtual trials can help to understand why flow diversion sometimes fails or why flow diversion sometimes leads to post-treatment complications.

1.3   Aim and research questions

The aim of the work presented in this thesis was to identify and address the main challenges in creating an *in-silico* trial framework for assessment of flow diverters' performance in treatment of intracranial aneurysms. Although most methods developed in this work are general to any *in-silico* trial framework in vascular flow, the models were demonstrated on aneurysm flow and aneurysm flow diversion. I also note that in personalised medicine, models and workflows developed in this work can be used in patient selection and treatment planing of aneurysms with indication of flow diversion. I addressed these questions:

- What are the key ingredients of a model for virtual treatment of aneurysms? How can uncertainty and variability in inputs of each ingredient model affect the model outputs? – Literature review

- How can statistical models be used to quantify uncertainty in internal carotid artery blood flow waveforms and to generate a virtual population of ICA waveforms? In addition, how can these uncertainties affect the quantification of WSS on the aneurysm sac?

- As part of a metric to evaluate success of flow diversion, how can a virtual treatment model assess FD-induced clot stability?

- How can a fully automatic flow-modelling framework be built to enable *in-silico* clinical trials of flow diverters? In addition, how can computationally inexpensive models be used to reduce the computational costs of such frameworks?

Figure 1.1 provides a diagram illustrating the research questions and thesis structure.

1.4 Contributions

Chapters 2 to 5 each present a study addressing the above research questions. The chapters are adapted from published or submitted journal or peer-reviewed conference papers and are self-contained. Therefore, some concepts might be repeated but reformulated according to the specific interests of each chapter. In this section, I provide an outline of the thesis, and summarise its contributions.

- *Chapter 2* – As part of a FD *in-silico* clinical trial framework, a virtual endovascular treatment model is needed to treat the virtual patients and perform the virtual experiments. In this chapter, I presented an advanced review of the key ingredient models of a virtual endovascular treatment workflow for device assessment in terms of inducing a stable clot inside the aneurysm. As discussed in section 1.1, when creating a framework for *in-silico* clinical trials, it is important to incorporate variability and uncertainty of the input variables to the models used in the framework. The sources of variability and uncertainty in virtual endovascular treatment workflows were reviewed, and where possible, I quantified the effects of these variabilities and uncertainties using a meta-analysis of works published in the literature.

    Sarrami-Foroushani, A.; Lassila, T.; Frangi, A. F., "Virtual endovascular treatment of intracranial aneurysms: models and uncertainty." Wiley Interdisciplinary Reviews: Systems Biology and Medicine *9(4):e1385, 2017.*

- *Chapter 3* – Intrinsic to creating *virtual populations* needed for *in-silico* trials is collecting and analysing clinical data and developing generative statistical models to populate *envelopes*[2] of patient physiology. The literature review (presented in Chapter 2), showed that aneurysmal haemodynamics is sensitive to the variations in inflow boundary conditions. However, these variations can occur in both the time-averaged magnitude of the pulsatile flow or the waveform itself. In this chapter, I

---

[2]The term envelope is used to refer to the entire range of possible variation of a variable (e.g., vascular blood flow rate) under a specific condition

develop a method for statistical modelling of waveform variability in internal carotid blood flow waves used as inflow boundary conditions in aneurysm flow simulations. The uncertainties arising from inter-subject variability of internal carotid blood flow were quantified; a virtual population of 50 flow waveforms were created, and the uncertainties were propagated to the model output space (aneurysm wall shear stress). Using this approach, it was also studied that what happens to the aneurysm rupture likelihood predictions made by deterministic models, if one incorporates the flow uncertainties.

Sarrami-Foroushani, A.; Lassila, T.; Gooya, A.; Geers, A. G.; Frangi, A. F., "Uncertainty quantification of wall shear stress in intracranial aneurysms using a data-driven statistical model of systemic blood flow variability." Journal of Biomechanics *49(11):3815-3823, 2016.*

- *Chapter 4* – An *in-silico* trial framework needs a *device performance indicator* to assess effectiveness of the FDs in inducing a stable clot inside the aneurysm sac. In chapter 2, I argued that prediction of post-FD biochemistry and the clot composition is essential for assessing FD success. In this chapter, I developed a new model of thrombus formation and platelet dynamics inside intracranial aneurysms that enabled characterising stable and unstable thrombus.

  Sarrami-Foroushani, A.; Lassila, T.; Hejazi, S. M.; Nagaraja, S.; Bacon, A.; Frangi, A. F., "A computational model for prediction of clot platelet content in flow-diverted intracranial aneurysms." under review, 2018.

- *Chapter 5* – To enable large-scale *in-silico* trials, there is a need for (i) an automated workflow implemented on a computational platform that provides the capability of streamlining the virtual experiments and running them in parallel (ii) making simulations computationally inexpensive, for example, by replacing the costly mechanistic models with data-driven phenomenological models. In this chapter, I presented two proof of concept studies to show how each of these needs can be met. In the first study, I built a fully automatic aneurysm flow-modelling framework and utilised a parallel-processing platform (`MULTIX`, `www.multi-x.org`) to simulate flow in a cohort of aneurysms at rest and exercise conditions. In the second study, a computationally inexpensive, statistical framework was developed to predict the aneurysmal wall shear stress patterns directly from the aneurysm shape.

  Lassila, T.; Sarrami-Foroushani, A.; Hejazi, S. M.; Frangi, A. F., "Population-Specific Flow Modelling: Between/Within-Subject Variability in the Internal Carotid Arteries of Elderly Volunteers." under review, 2018.

Sarrami-Foroushani, A.; Lassila, T.; Pozo J. M.; Gooya, A.; Frangi, A. F., "Direct Estimation of Wall Shear Stress from Aneurysmal Morphology: A Statistical Approach." International Conference on Medical Image Computing and Computer-Assisted Intervention – MICCAI 2016 *pp. 201-209, 2016*
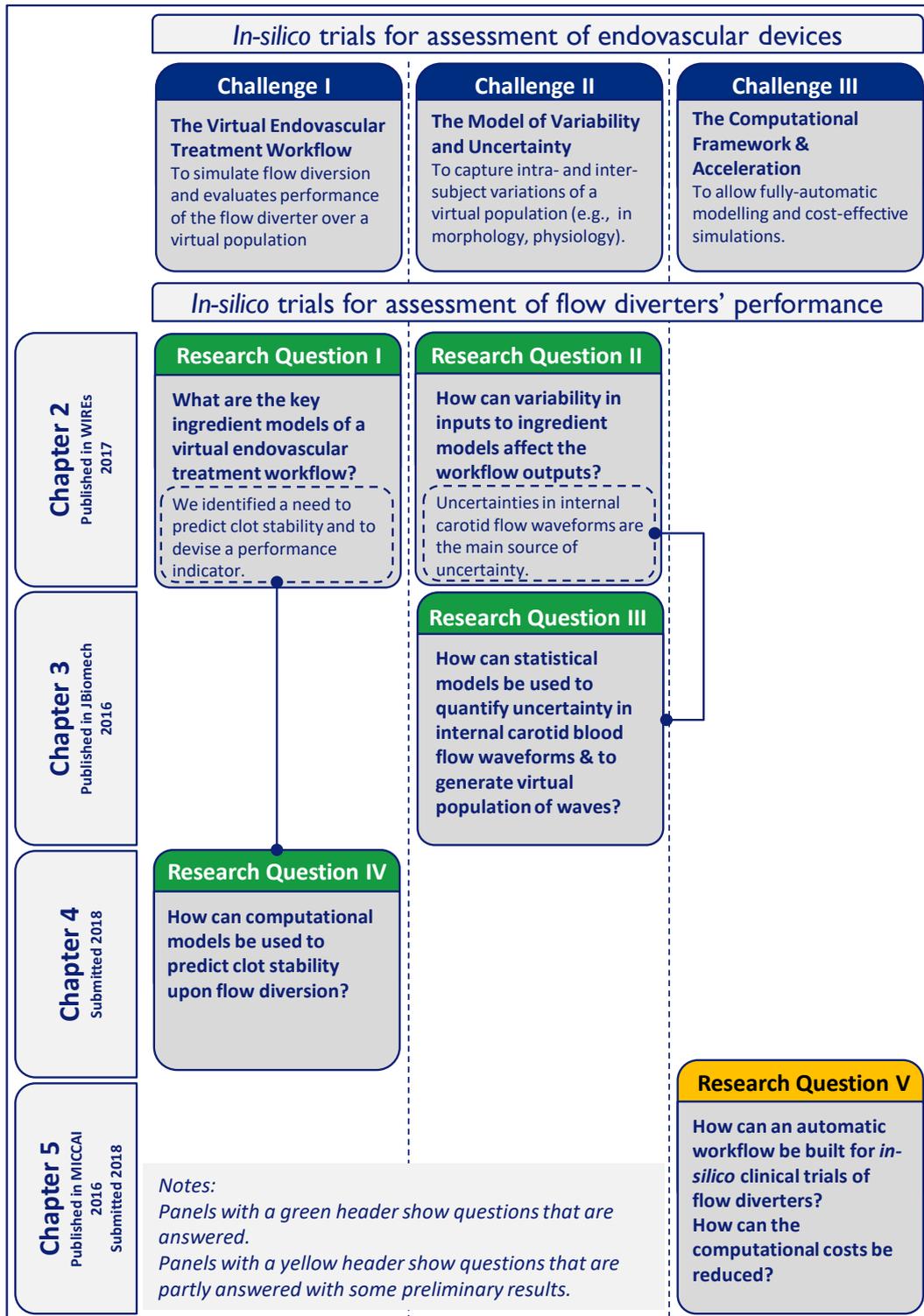
Figure 1.1: A graphical representation of the thesis structure, and the contribution of each chapter.

Chapter 2

Virtual endovascular treatment of intracranial aneurysms: models and uncertainty

Abstract — Virtual endovascular treatment models (VETMs) have been developed with the view to aid interventional neuroradiologists and neurosurgeons to preoperatively analyse the comparative efficacy and safety of endovascular treatments for intracranial aneurysms. Based on the current state of VETMs in aneurysm rupture risk stratification and in patient-specific prediction of treatment outcomes, I argue there is a need to go beyond personalised biomechanical flow modelling assuming deterministic parameters and error-free measurements. The mechanobiological effects associated with blood clot formation are important factors in therapeutic decision making and models of post-treatment intra-aneurysmal biology and biochemistry should be linked to the current purely haemodynamic models to improve the predictive power of current VETMs. The influence of model and parameter uncertainties associated to each component of a VETM are, where feasible, quantified via a random-effects meta-analysis of the literature. This allows estimating the pooled effect size of these uncertainties on aneurysmal wall shear stress. From such meta-analyses, two main sources of uncertainty emerge where research efforts have so far been limited: i) vascular wall distensibility, and ii) intra/inter-subject systemic flow variations. In the future, I suggest that current deterministic computational simulations need to be extended with strategies for uncertainty mitigation, uncertainty exploration, and sensitivity reduction techniques.

1

---

[1]Adapted from: Sarrami-Foroushani, A., Lassila, T., & Frangi, A.F.: Virtual endovascular treatment of intracranial aneurysms: models and uncertainty. Wiley Interdisciplinary Reviews: Systems Biology and Medicine, 9(4):e1385, 2017.

2.1   Introduction

Intracranial aneurysms (IAs) are pathological dilatations of the intracranial arteries that commonly occur in various locations around the circle of Willis in approximately 5-8% of the general population [8]. Aneurysm rupture causes subarachnoid haemorrhage, which is associated with high rates of morbidity, mortality, and long term disability [8]. The clinical strategy for treating aneurysms is to isolate them from the circulation, which is commonly performed either by open surgery (clipping the aneurysm), or by endovascular treatment (catheter insertion of a flow diverter or a coil within the aneurysm). In each method, isolation is aimed at creating conditions of blood stasis leading to the generation of a stable clot in the aneurysm sac (embolisation). Once the aneurysm has occluded completely, a neo-intimal layer forms over the aneurysm neck and separates the aneurysm from the circulatory system (endothelialisation). Although it might be addressed as more advanced interventional techniques become available, currently, aneurysms treated with endovascular techniques are more likely to recur than those treated surgically [20]. However, the non-invasiveness of the endovascular approaches has made them more favourable options for treatment of IAs.

Recent progress made in diagnostic techniques over the past few decades has increased the detection rate of unruptured IAs [21]. This has consequently posed the dilemma of whether every unruptured aneurysm must be treated immediately upon discovery, and if so, which treatment option represents the least risk to the patient [20, 22, 23]. The challenge is therefore to evaluate the safety and efficacy of different endovascular treatments in a patient-specific context. Post-treatment ruptures, aneurysm recurrence or incomplete occlusion, and thromboembolic complications after endovascular treatment further magnify the importance of choosing an appropriate endovascular treatment option. Clinicians' attempts at answering such questions has revealed the need for tools that help them in reliable risk assessment and designing appropriate patient-specific treatment plans for each individual aneurysm.

The important role of haemodynamics in the initiation, progression, and rupture of aneurysms has drawn the research community's attention to image-based computational fluid dynamics simulations. Such tools would allow researchers to study the haemodynamic variables in each specific aneurysm pre- and post-operation. Exploiting recent advancements in image segmentation and computational mechanics, virtual endovascular treatment models (VETMs) have been developed to create image-based patient-specific models of aneurysm geometries [24, 25, 26], to virtually deploy endovascular devices [27, 28, 29, 30], and to simulate intra-aneurysmal blood flow [31, 32, 33]. This has allowed investigating how safely and effectively each device deployment strat-
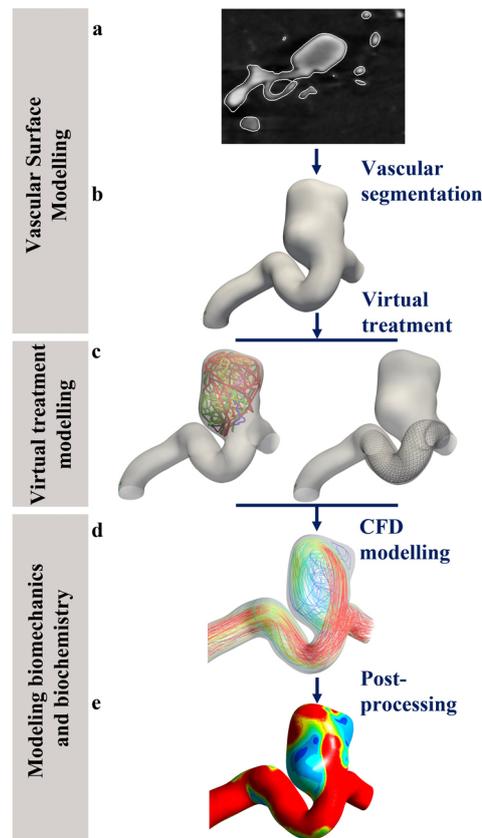
Figure 2.1: An ideal virtual endovascular treatment model is comprised of sub-models in which the vascular surface, virtual treatment, and biomechanics and biochemistry are modelled, respectively. Patient's angiogram (a) is segmented and a vascular surface model (b) is reconstructed and used for virtual treatment with coils or flow diverting stents (c). Computational simulations then are performed to calculate blood velocity field (d) in the presence of device-induced intra-aneurysmal clot, from which the shear stresses on the vessel wall (e) can be computed.

egy alters the intra-aneurysmal haemodynamics, and to what extent the altered intra-aneurysmal flow is favourable to the formation of a stable clot, leading finally to complete aneurysm occlusion and elimination [33, 34]. Moreover, such endovascular treatment models help clinicians to pre-operatively assess the candidate treatment options and deployment strategies; especially in complex cases like anatomically complex and surgically inaccessible vertebrobasilar dolichoectasia with fusiform aneurysms [35, 36], or aneurysms at/near bifurcations where the neighbouring branches/perforators are at the risk of being covered and occluded [37].

The identification of an appropriate metric to assess post-operative performance of the endovascular treatment is still an active area of research. Different flow and wall shear stress-related quantities have been proposed for this purpose. Localised low and

oscillatory aneurysmal wall shear stress (WSS) is hypothesised to lead to pathological endothelial responses, thrombosis, wall degeneration, and eventual aneurysm rupture [38]. On the other hand, endovascular devices are shown to trigger the aneurysm healing process by inducing flow stasis and thrombosis inside the aneurysm sac [20]. However, it is not clear why low shear-induced thrombosis may lead to complete embolisation in some aneurysms, but incomplete embolisation and rupture in some others [39, 40]. Kulcsar *et al.* [39] hypothesised that the quality, quantity, and evolution of the thrombus and consequently the thrombus-induced autolytic activities in the wall, determine whether intra-aneurysmal thrombus generation leads to aneurysm healing or rupture. This implies that the endovascular device performance should be assessed in terms of the capability to induce a stable clot, which triggers the process of reverse remodelling and aneurysm healing, possibly accounting for the effect of coadjuvant blood-thinning pharmacological agents. Therefore, although post-operative aneurysmal haemodynamics play an important role in the outcome of the intervention, a VETM should incorporate information about device-induced biochemistry and mechanobiology for assessing its performance for making predictions about aneurysm occlusion and treatment outcomes. Such information can be provided either by phenomenological sub-models that use haemodynamics as a surrogate of intra-aneurysmal biochemistry and biology [41, 42, 43], or by more complex mechanistic sub-models, which are coupled to the haemodynamic sub-models and describe the ongoing biological process [41, 44, 45]. Consequently, as shown in Figure 2.1, an ideal VETM is comprised of: 1) a computational blood flow simulation in an image-based vascular surface model coupled with proper boundary conditions, 2) an endovascular device deployment model, and 3) a blood coagulation model, which describes the intra-aneurysmal clot formation process in the presence of endovascular devices.

In 2012, Kallmes *et al.* [46] raised concerns about the clinical relevance of computational models by arguing that they are prone to several sources of uncertainty and error that influence the model predictions. Despite many advancements bridging some of the gaps between model predictions and actual physiological phenomena, the characterisation of the uncertainties and errors associated with the model inputs, and the sensitivity of personalised haemodynamic predictions require more detailed investigation. Uncertainties arise from lack of personalised information about some model inputs, imprecise model structures, e.g. mathematical descriptions of the biological phenomena, and inherent inter- and intra-subject variabilities of physiological variables. As depicted in Figure 2.2, uncertainty quantification can be performed to identify and quantify uncertainties in the model inputs. Similarly, error analyses can be performed to identify and quantify errors in the deterministic inputs that are not
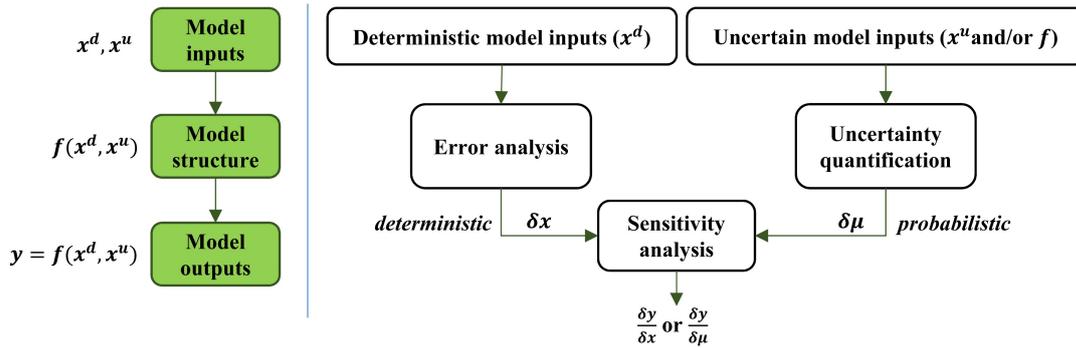
Figure 2.2: The left panel shows overall structure of a typical mathematical model with x_d and x_u as vectors of deterministic and uncertain model inputs, respectively; f describing the model structure; and y as vector of model outputs. The right panel shows error analysis and uncertainty quantification as processes to identify and quantify errors and uncertainties, respectively; and sensitivity analysis as a process to propagate the quantified errors and uncertainties to the model outputs.

uncertain but can produce errors if not selected properly, e.g. computational meshes. In order to reliably represent the patient-specific physiological processes and achieve truly clinically relevant predictions, it is important that these uncertainties and errors be propagated into the model predictions through sensitivity analyses, and be eliminated when possible.

I address the state of different sub-models of a typical VETM based on a comprehensive literature review of the articles focused on computational models of intracranial aneurysms and published online before June 2016. For each sub-model, the possible sources of uncertainty and error were discussed, and, where they exist, review the sensitivity analyses that have been done to show how model predictions are affected by either the uncertain inputs or errors in the deterministic inputs. For simplicity, from now on, I denote both uncertain inputs and errors in deterministic inputs as uncertainty throughout the paper. In order to summarise the effect of uncertain inputs, meta-analyses are conducted where the following criteria are met: 1) the study was numerical, performed on the intracranial aneurysms, and published between January 2006 to June 2016, 2) at least 3 cases were studied, and 3) the effect of uncertain model inputs on the aneurysmal WSS was investigated and quantitative values of WSS were reported. For those sources of uncertainties where a sufficient number of studies provided evidence, effect sizes are calculated as standardised mean differences (Hedges' g) between the two non-independent groups in each study and then are pooled across studies using random-effects meta-analysis [47]. Finally, I summarise the most important uncertainties that should be addressed in order to present patient-specific predictions

to enable such simulations to be reliably used in clinical practice.

2.2 Vascular surface and blood flow modelling

2.2.1 Image-based patient-specific vascular surface modelling

Creating vascular surface models from medical images is the first and most important step in developing a patient-specific model for endovascular treatment of aneurysms [31], on which all the other steps depend. Vascular angiograms are usually acquired using computed tomography angiography (CTA) [48], magnetic resonance angiography (MRA) [49], or three-dimensional rotational angiography (3DRA) [50]. The spatial resolution of 3DRA ($128^2 - 512^2$ matrix with voxel size of 0.42-1 mm) is usually higher than CTA (512^2 matrix with pixel size of 0.23-0.45 mm and slice thickness of 0.5-1.3 mm) and MRA (256^2 matrix with pixel size of 0.78-1.25 mm and slice thickness of 0.7-1.6 mm) [24]. Piontin *et al.* [51] assessed the accuracy of 3DRA, CTA, and MRA techniques for measuring the volume of an in vitro model of an anterior communicating artery aneurysm. They showed that CTA is more accurate than MRA (p-value = 0.0019), and 3DRA is more accurate than CTA, (p-value = 0.1605; not statistically significant). They observed that aneurysm volume was overestimated by 7% and 11.3% in 3DRA and CTA, respectively, and underestimated by 15% in MRA images. Ramachandran *et al.* [52] reported that errors in measuring aneurysm characteristic lengths (e.g., height and maximum diameter) by any of the 3DRA, CTA, and MRA were 0.8-4%, with no significant differences between the modalities. In clinical practice, due to the less invasive nature of CTA and MRA, these imaging techniques are favoured for the diagnosis and monitoring of intracranial aneurysms; however, 3DRA provides the highest spatial resolution and is consequently favoured for surgical or endovascular treatment planning [53, 54, 55]. On the other hand, high spatial and contrast resolution and no interference of bony structures and surrounding tissues in 3DRA images, and consequently their ease of reconstruction, make them more appropriate for construction of 3D aneurysm surface models that can subsequently be used in computational fluid dynamics (CFD) analyses and virtual treatment models [24, 51, 56, 57].

Starting from volumetric medical images, different techniques have been proposed for segmentation and creation of vascular surface models, which can then be used for generating a computational volumetric mesh and solving blood flow equations. In this paper, I only reviewed methods which have been tested and evaluated on intracranial aneurysms. The need for contrast injection into the feeding artery of the aneurysm exposes the 3DRA modality to limitations when aneurysms with multiple feeding arteries are being scanned. Castro *et al.* [56] proposed a segmentation methodology,

which combined image co-registration and surface merging techniques to overcome this limitation, and provided surface models for aneurysms with multiple inlet branches such as those located on the anterior communicating arteries. They evaluated their method on a virtual 3D rotational angiogram of a digital phantom of an anterior communicating artery aneurysm. The maximum distance between the segmented and phantom model (0.2 mm) was reported as a measure of accuracy. Chang *et al.* [24] proposed another segmentation methodology called charged fluid-based aneurysm segmentation (CFAS), which combined a region-growing method with the 3D extension of a deformable contour based on a charged fluid model. Their method was particularly designed for segmentation of aneurysms with different geometrical complexity levels and was evaluated on 3DRA images of 15 aneurysms. Comparing segmented surfaces with the manually delineated contours, a conformity score of 68.36% was reported. A knowledge-based segmentation algorithm based on the geodesic active regions (GAR) was presented by Hernandez *et al.* [26] and evaluated by segmentation of intracranial aneurysms from CTA (10 aneurysms) and 3DRA (5 aneurysms) images. They reported average dice similarity coefficient (DSC) of 91.13% and 73.31% as measures of accuracy for 3DRA and CTA images, respectively. Bogunovic *et al.* [58] proposed another methodology for segmenting 3DRA images based on an image intensity standardisation (IIS) –method, which improved the automation of knowledge-based vascular segmentation algorithms by standardisation of image intensity ranges of tissue classes in routine medical images. They evaluated the method on 10 patients that underwent both 3DRA and time-of-flight magnetic resonance angiography (TOF-MRA). DSC scores of 92% and 91% was achieved for segmentations from 3DRA and MRA images, respectively. Firouzian *et al.* [25] proposed another segmentation technique for segmenting aneurysms from CTA modality, which worked based on geodesic active contours (GAC) and did not require image intensity training unlike when working with knowledge-based methods. They evaluated the method on 11 aneurysms and reported a DSC score of 82.1% as a measure of accuracy. A detailed review of the above mentioned methods can be found in Refs [31, 32, 33, 59]. Comparisons of different segmentation techniques for intracranial aneurysms can also be found in Refs [58, 60].

2.2.2 Uncertainty in vascular surface modelling

Uncertainties in the vascular geometric models can originate from images used to reconstruct the vascular surfaces. Such uncertainties include the inherent noise in the acquired images, registration artefacts, and motion of arteries during the cardiac cycle. Depending on the operator's experience and skill, manual operations during image acquisition may also lead to errors in the acquired images. Another more important

source of uncertainty in vascular surface modelling are segmentation errors. Despite automation of the segmentation process in most state-of-the-art segmentation methods, manual editing operations are still required in the final stages, especially where complex structures like small or kissing branches are present in the region of interest.

Cebral *et al.* [31] performed a sensitivity analysis on different uncertain aspects of an image-based model. They qualitatively showed that the geometric uncertainties arising from segmentation of aneurysm surfaces by different operators has the greatest effect on the intra-aneurysmal flow when compared to uncertainties in other variables. Castro *et al.* [61] investigated the effect of parent vessel reconstruction on the flow in the aneurysm sac. For each aneurysm they constructed two different models; one with the original parent vessel and the other with a truncated parent vessel, which was replaced with a straight tube. They observed an underestimation of aneurysmal WSS in geometric models with a truncated parent vessel and showed that segmentation of the parent vessel can highly affect the characteristic flow patterns inside aneurysm. As a future work, they suggested a sensitivity analysis for typical aneurysms of different locations, which gives an estimation of the length of the upstream parent vessel needed for an appropriate simulation of flow inside the aneurysm. Gambaruto *et al.* [62] compared the effect of the smoothing level, as part of the segmentation procedure, with the effect of the blood rheological model on the intra-aneurysmal flow and aneurysmal WSS. They showed that geometric uncertainties due to the use of different smoothing levels resulted in greater errors (of order of 15%), although this was comparable with errors arising from using different blood rheological models (of order of 5%). Geers *et al.* [57, 63] performed CFD simulations in aneurysm models reconstructed from CTA and 3DRA images. They showed that the main flow characteristics remains the same in aneurysms obtained from both modalities but a difference of up to 44.2% was observed in the absolute value of mean WSS on the aneurysm sac.

2.2.3   Blood flow modelling

In order to simulate blood flow in the reconstructed vascular volume, equations of motion for blood flow need to be discretised and solved. This requires a volumetric mesh over the domain confined by the vascular surface mesh. Vascular surface meshes are usually extruded at the truncated boundaries to minimise the effects of boundary conditions on the domain of interest (i.e., the aneurysm) Tetrahedral or polyhedral elements are commonly used to discretise the volume [64]. To accurately address high velocity radial gradients in vicinity of the wall, and thus to accurately estimate the WSS, three to five layers of prismatic boundary layer elements are required in near-wall regions [31, 65, 66]. Unstructured meshes in the context of aneurysm flow

modelling are commonly comprised of elements of 0.1-0.2 mm and three boundary layer prism layers with a total height of 0.05-0.15 mm. Careful mesh-dependency tests are necessary to achieve mesh-independent solutions [67]. The presence of vascular devices with very fine struts that are placed in vessels several order of magnitude larger in diameter pose a challenge to meshing algorithms. Computational meshes need to be computationally cost effective to solve for the flow in the aneurysm and parent arteries while, at the same time, be accurate enough to resolve the flow around the very thin wires of stents or coils and the near-wire grid elements must be fine enough to resolve the wires and accurately reconstruct flow through the implanted device. Stuhne and Steinman [68] suggested that the mesh resolution in the vicinity of the stent wires needs to be about one-third of the wires radius to achieve an accurate flow solution in the near-strut regions. Other studies (e.g., Refs [69, 70]) have also reported on the properties of convergence of haemodynamics solutions in stented aneurysms with near-strut element sizes similar to what was reported by Stuhne *et al.* [68]. The widely-used body-fitted [71] grid generation can be complex and time-consuming for meshing aneurysms with implanted endovascular devices. Cebral *et al.* [72] proposed a hybrid method which uses the body-fitted approach to discretise the interior of the vessel walls but the adaptive embedded [71] approach for meshing the endovascular devices. Appanaboyina *et al.* [73] compared solutions produced by the hybrid approach and the pure body-fitted grids and showed their agreement (1-3% difference in predicting the maximum post-treatment velocity reduction over three predefined lines passing through the sac) after three levels of adaptive refinement of the near-strut elements in the hybrid approach.

Solving equations of motion requires setting the constitutive parameters (i.e., density and viscosity) as well as prescribing boundary conditions to the fluid. Blood flow in medium-sized arteries can be assumed to be incompressible with constant density. The rheology of blood can either be described by using a Newtonian model with a constant viscosity, which simplifies the equations of motion to the Navier-Stokes equations, or by using non-Newtonian models that consider the shear-thinning behaviour of blood.

As common practice in CFD modelling of blood flow in vascular domains, a velocity-related (usually flow rate) boundary condition is assigned at the inlet boundaries. This can be a constant flow rate (steady simulation) or a time-varying flow waveform (unsteady simulation). Such inflow boundary conditions are often derived from literature, where blood flow measurements are acquired in a particular artery for a specific cohort of people and reported in terms of descriptive statistics (mean values from standard deviations, see e.g. the works [74, 75, 76]). In some cases, patient-specific flow measurements are available from phase-contrast magnetic resonance imaging (PC-MRI)

or transcranial Doppler ultrasound (TCD), and patient-specific inflow boundary conditions are used for CFD simulations.

To prescribe outlet boundary conditions, zero-pressure boundary conditions are adequate for vascular domains with only one outlet. In contrast, in vascular domains with more than one outlet, flow distribution among outlet branches depends on the resistance and compliance of the distal vascular bed, which requires more advanced techniques to estimate the flow distribution ratio. However, many studies neglect the distal resistances and use zero-pressure outlet boundary conditions for multiple outlet vascular domains, which allows the flow to distribute among daughter branches according to their diameter and pressure drop [77]. To consider the effect of distal resistance and compliance, the three-dimensional computational vascular domain of interest can be coupled to lower-dimensional reduced-order models [78, 79]. However, although such boundary conditions give a more accurate representation of distal resistances, they increase the amount of parameters to be set in the model. Zero-dimensional (lumped parameter) [79, 80] models usually require setting the values of the terminal resistance and capacitance at each outlet branch. In one-dimensional models [81, 82, 83, 84] the branching topology, length, diameter, and material properties of vessel segments need to be assigned. Although some studies (e.g. Refs [85, 86, 87]) used fluid-structure-interaction techniques to account for the arterial wall compliance in the models, wall distensibility is neglected in almost all CFD simulations of blood flow in aneurysms and a no-slip boundary condition is assigned on the walls.

Despite the use of various commercial or in-house solvers with different numerical solution strategies by CFD modellers for simulating aneurysmal flow, recent CFD challenges [88, 89] showed a global agreement between the haemodynamic quantifications produced by various CFD solvers in the participating groups. However, as noted, simulation of vascular blood flow requires proper setting of constitutive parameters and prescribing boundary conditions. Both constitutive parameters and boundary conditions are subject to intra-subject and inter-subject variabilities which introduce uncertainties into the computational models of blood flow. Intra-subject variabilities have roots in the state of the person (e.g., level of stress, physical activity, sleep pattern, etc.). For example, plasma volumes losses during maximal exercise will result in increases in haematocrit, haemoglobin concentration, and concentration of plasma proteins, which consequently increase the blood viscosity [90]. Inter-subject variabilities have roots in demographic characteristics (e.g., age, gender, weight, etc.) or the person's lifestyle (smoking, drinking, physical activity, etc.). For example, both ageing and smoking will affect the arterial wall properties and consequently alter the arterial flow waveforms [76, 91]. On the other hand, uncertainties in computational blood flow

simulations can also arise from assumptions associated to the underlying models (e.g., wall motion or blood rheological models). The influence of such uncertainties on the aneurysmal haemodynamics is discussed in the next section.

2.2.4 Uncertainty in blood flow modelling

Blood rheology is often assumed to be Newtonian, which while an acceptable approximation in medium-sized arteries, is strictly speaking not consistent with the shear-thinning nature of blood. An overestimation of aneurysmal WSS magnitude with almost no effect on the WSS distribution on the aneurysm sac has been reported in several studies comparing aneurysmal WSS values obtained from Newtonian and non-Newtonian simulations [31, 92, 93]. Xiang *et al.* [94] compared Newtonian CFD simulations with those performed with the Casson [95] and Herschel-Bulkley [95] models and observed almost similar WSS distributions and magnitude in two of the three examined aneurysms; in the other complex-shaped aneurysm, the Newtonian model overestimated WSS on the aneurysm bleb with a low WSS magnitude. Since low WSS regions are thought to be the regions where aneurysms may rupture, Xiang *et al.* [94] suggested that using a Newtonian model might underestimate the aneurysm rupture risk in aneurysms with pronounced low shear regions, e.g., complex aneurysm shapes with daughter aneurysms; they also noted the importance of blood rheology in simulating post-treatment flows where intra-aneurysmal stasis is induced in the presence of endovascular devices to trigger thrombosis and the aneurysm healing process. Castro *et al.* [96] compared CFD simulations performed with Newtonian and Casson models in ten multi-bleb aneurysms. They observed that the Casson model produced higher WSS values on some aneurysmal regions at some instances during the cardiac cycle. However, since the differences were not statistically significant, they concluded that there was no evidence that any of the models overestimate aneurysmal WSS values.

Gambaruto *et al.* [62] compared the effect of blood viscosity model and geometric uncertainties and showed that segmentation errors had greater effects on the model outcomes. The errors in mean aneurysmal WSS were of the order of 15% for geometric uncertainties and 5% for uncertainties in the rheological model. Fisher *et al.* [97] compared aneurysmal WSS numerically predicted using four different rheological models in idealised aneurysm geometries; they showed that, compared to the parent vessel, the non-Newtonian effects were measurable inside the aneurysm sac (especially during the diastole); they observed the Carreau [95] model to be the most conservative, producing lower WSS magnitudes with larger regions of low WSS. However, Fisher *et al.* [97] emphasised that although the choice of the blood rheology model seems to have an effect on the numerical predictions of WSS, the differences raised from uncertainties in

the aneurysm morphology were greater.

Other studies investigated the effect of the choice of blood rheological model in the presence of endovascular devices. Rayz *et al.* [43] investigated intra-aneurysmal haemodynamics in three fusiform aneurysms that were thrombus-free pre-treatment, but developed thrombus during follow-up studies. They showed better agreement, although not statistically significant, between the low-flow regions and regions of thrombus deposition when a non-Newtonian rheology model was used. Morales *et al.* [98] studied the effect of blood rheology on steady flow simulations in three aneurysms before and after coiling; in untreated aneurysms, the Newtonian model overestimated intra-saccular velocities up to 16% in space-averaged velocities with a maximum of 45% in pointwise comparisons; these increased up to 55% in space-averaged velocities with a maximum of 700% in pointwise comparisons in coiled aneurysms; space-averaged WSS differed up to 2% and 12% between the two rheological models in the untreated and coiled aneurysms, respectively, while the Newtonian model overestimated the WSS in some cases and underestimated the WSS in others. These results demonstrate again the magnification of non-Newtonian effects in slow flow regions. However, Morales *et al.* [98] reported similar global flow patterns and post-treatment aneurysmal flow reductions in both Newtonian and non-Newtonian models. Admitting the observed magnitude differences in coiled aneurysms with thrombogenic slow flows, Morales *et al.* [98] concluded that a Newtonian rheology model could be adequate for blood flow simulations in coiled aneurysms, if the global haemodynamic alterations are used for device performance assessment. Huang *et al.* [99] studied the effect of blood rheology modelling choices in idealised stented aneurysms and observed that Newtonian models overestimated the intra-aneurysmal mean velocity magnitude by 6-26% in large-neck stented aneurysms and by 51-57% in small-neck stented aneurysms. Cavazzuti *et al.* [100, 101] investigated the effect of using a non-Newtonian rheology model in stented aneurysms and observed that average aneurysmal WSS values produced by the Newtonian rheology were around 15% greater in some regions and smaller in other regions; they concluded that the Newtonian to non-Newtonian effects are generally important but position dependent.

Among the above mentioned studies, Castro *et al.* [96], Morales *et al.* [98], and Fisher *et al.* [97] performed quantitative comparisons between time and space-averaged aneurysmal WSS values obtained from CFD simulations based on Newtonian and non-Newtonian (Casson) rheology and reported values of time-and-space-averaged WSS on the aneurysm sac for different cases. According to a random-effects meta-analysis, the standardised mean difference (Hedges' g) was 0.02 with a 95% confidence interval of -0.04 to 0.07. This suggests limited effect of blood rheology model choice on WSS
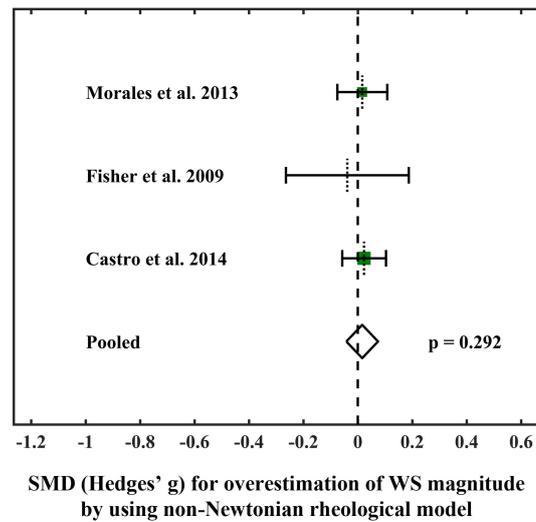
Figure 2.3: Forest plot showing the overestimation of space and time-averaged aneurysmal WSS produced by the non-Newtonian blood rheology. The plot illustrates effect sizes, Hedges' g, (represented by a square) and the confidence intervals (the horizontal lines) for each study and the pooled effect (the centre of the diamond) and its confidence interval (the width of the diamond) across all studies. Vertical dotted lines for each study show the study mean and the green squares are sized according to the study weight.

predictions by CFD. The meta-analysis based on these three studies failed to find a significant overall effect for the choice of rheological model (p-value = 0.292). None of the studies presented a pointwise comparison of aneurysmal WSS values provided by each rheology. Comparing time-and-space averaged WSS values, the study with the largest cohort performed by Castro *et al.* [96], showed that WSS values produced by the Newtonian model were twice as large as the values predicted by non-Newtonian models at some aneurysmal regions; however, at some other regions on the same aneurysm, the Newtonian model predicted WSS values half as large as those predicted by the non-Newtonian model. They found no significant correlation between low WSS regions and regions where any of the models produced higher or lower WSS than the other.

The forest plot presented in Figure 2.3 illustrates the results provided by the meta-analysis. Standardised mean differences (SMDs), defined as the difference between the mean values of the two groups (i.e., Newtonian and non-Newtonian cases) divided by a representation of the standard deviation [47], are used to present the effect size reported by each study and the pooled effect size. Cohen's d and Hedges' g are two different formulations for calculation of the SMDs, which differ in the type of the standard deviation used to standardise the mean differences [47]. Since the Cohen's d is known to overestimate the effect sized in small samples [47], in this study I used Hedge's g which

is the unbiased estimation of the effect size. As suggested by Cohen *et al.* [102], effects of size 0.2, 0.5, and 0.8 can be interpreted as small, medium, and large, respectively. Based on the reviewed works and the meta-analysis, it can be concluded that differences between the aneurysmal WSS values produced by any of the investigated rheological models have not been shown to be significant. Although all the reviewed studies reported differences in magnitude of the WSS values, it is still not clear whether any of the investigated rheological models produce systematically larger or smaller WSS values. Flow stasis and low recirculating flow are known to play an important role in aneurysmal inflammatory phenotype and thrombosis, and consequently in rupture or device-induced aneurysm healing. Thus, the observed discrepancies in WSS values suggest consideration of non-Newtonian behaviour of blood where the aneurysmal flow is very slow and disturbed due to the irregular aneurysm shape or is reduced by endovascular devices. Such consideration is more important when local haemodynamic evaluations, rather than global time- or space-averaged haemodynamic quantities, are of interest. Moreover, although all the reviewed studies reported almost no influence of blood rheological model choice on the WSS distribution and characterisation of regions where shear stress is relatively low or high, it is not still clear whether the reported discrepancies in magnitude and direction of CFD-predicted shear stresses result in false predictions about the aneurysm or the endovascular treatment effect.

Inlet boundary conditions to the vascular model of interest are another ingredient of the flow simulation that contains uncertainty. Inflow boundary conditions are often taken from the literature, where typical flow waveforms in a particular artery are reported for a specific cohort of people who usually have demographic differences with the specific patient whose aneurysm is being simulated. Some studies [103, 104, 105] used patient-specific inflow boundary conditions obtained from patient-specific measurements. Such patient-specific boundary conditions are superior to the typical literature-based boundary conditions, since they are acquired from the same patient. However, even the patient-specific boundary conditions cannot fully represent systemic blood flow, since systemic flow is highly dependent of the state of the person (e.g., level of stress, physical activity, sleep pattern, etc.) and measurements are only acquired at a particular point in time and under very specific scanning conditions. Nevertheless, although not representative of the effect of intra-subject variability, using one-shot measurements of patient-specific inflow boundary conditions has been shown to have limited effects on the distribution of WSS and oscillatory shear index (OSI) on the aneurysmal sac. However, comparing results obtained from simulations with typical literature-based and directly measured inflow boundary conditions has revealed remarkable differences in the magnitude of aneurysmal WSS and OSI [103, 104, 105, 106].

Consequently, exactly how intra-/inter-subject variations of systemic flow conditions may affect intra-aneurysmal haemodynamics and the rupture risk has become a relevant question within the research community.

Bowker *et al.* [107] investigated the effect of moderate aerobic exercise on three middle cerebral artery aneurysms and observed an average of 20% increase in time-averaged WSS on the aneurysm sac; this result has been obtained by keeping the inlet waveform fixed and increasing the time-averaged inflow and heart rate by 7.8% and 73.4%, respectively. Geers *et al.* [108] systematically investigated the effect of time-averaged inflow rate, heart rate, and inflow wave pulsatility index and showed that, under a fixed time-averaged flow rate, increasing heart rate and inflow pulsatility index had no effect on the aneurysmal time-averaged WSS magnitude. Xiang *et al.* [109] studied the effect of inflow waveforms on intra-aneurysmal haemodynamics of four aneurysms. They performed CFD simulations with four different waveforms that had the same time-averaged flow rate and showed that different waveforms produced the same spatial distributions on WSS and OSI on the aneurysm wall. They also observed the same values of time-averaged WSS magnitudes, but drastically different values of OSI in the four CFD simulations performed for each aneurysm. They finally concluded that inflow boundary conditions have only limited effects on the aneurysmal WSS and OSI for the purpose of aneurysm rupture stratification. Keeping the time-averaged flow rate fixed, Sarrami-Foroushani *et al.* [110], performed CFD simulations using inflow waveforms obtained from a data-driven model of internal carotid artery flow and observed that variations in internal carotid artery (ICA) flow waveform had no effect on the time-averaged WSS but altered the local directionality of WSS; they also showed that the inflow waveform variations changed the rupture outcome prediction in 4 out of 19 cases when a simple logistic regression model was used to predict the rupture outcome. For each aneurysm in a fifteen-aneurysm cohort, Morales *et al.* [111] performed eleven CFD simulations with different inflow rates (but using the same waveform) and showed that spatiotemporally averaged aneurysmal WSS varied as a quadratic function of time-averaged inlet flow rate. They showed that values of aneurysmal OSI did not change by changing the time-averaged flow rate while keeping the waveform constant.

Since patient-specific flow measurements are rarely available as a clinical routine for aneurysm patients, CFD modellers often scale the typical literature-based flow waveforms to approximately impose patient-specific boundary conditions to their models. For each aneurysm model, scaling is performed in order to maintain a fixed spatiotemporally averaged velocity or WSS at the inlet boundary. The literature-based flow rate is scaled according to the inlet diameter squared, if the scaling is based on time-
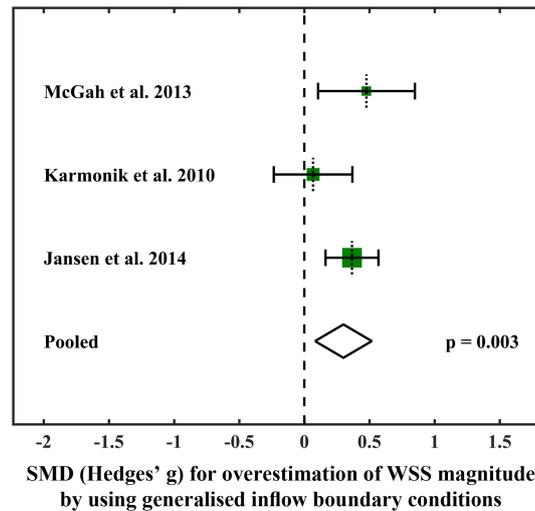
Figure 2.4: Forest plot showing the overestimation of space-and-time-averaged aneurysmal WSS produced by the generalised inflow boundary conditions. The plot illustrates effect sizes, Hedges' g, (represented by a square) and the confidence intervals (the horizontal lines) for each study and the pooled effect (the centre of the diamond) and its confidence interval (the width of the diamond) across all studies. Vertical dotted lines for each study show the study mean and the green squares are sized according to the study weight.

and-space-averaged velocity, and cubed, if the scaling is based on time-and-space averaged WSS [112, 113]. The choice of inlet location (and consequently inlet diameter) and scaling model (cubed or squared) is, however, a source of uncertainty in inlet boundary conditions. Valen-Sendstad *et al.* [112] investigated the effect of the choice of inlet location and the scaling model on the resulting inflow rates. They showed that scaling according to the squared diameter produced flow rates more consistent with the physiological flow rates. They also quantified the uncertainties arising from truncating the ICA at different locations and showed that all truncation locations below the cavernous segment produced the same uncertainties as physiological uncertainties of ICA flow rate and thus lead to reliable CFD simulations. Visually comparing CFD-predicted and digital subtraction angiography (DSA) -imaged intra-aneurysmal flow patterns, Pereira *et al.* [114] showed that reliable CFD outcomes were obtained using vascular models with inlet vessels truncated as far upstream as obtainable from the medical images, and coupled to Womersley inlet velocity profiles. Hodis *et al.* [115] also studied the effect of inlet artery length on 10 ICA ophthalmic aneurysm models and showed that removing two bends from the parent artery resulted in approximately 15% error in peak systolic space-averaged WSS over the aneurysm sac.

Jansen *et al.* [103], McGah *et al.* [105], and Karmonik *et al.* [106] performed quan-

titative comparisons between time-and-space-averaged aneurysmal WSS values obtained from CFD simulations based on measured patient-specific and generalised inflow boundary conditions and reported values of time-and-space-averaged WSS on the aneurysm sac for different cases. In these studies, the inlet boundaries of the vascular domains located on the ICA and generalised ICA flow waveforms were obtained from studies by Ford *et al.* [74] and Vanooij *et al.* [116], in which the ICA flow was measured over cohorts of 17 young and healthy volunteers and 8 patients with intracranial aneurysms, respectively. For each aneurysm case, McGah *et al.* [105] scaled the generalised waveform to maintain a physiological mean WSS of 1.5 Pa at the inlet boundary. However, Karmonik *et al.* [106] directly used the generalised flow waveforms obtained from the study by Ford *et al.* [74] without scaling; while Jansen *et al.* [103] have not reported the scaling process clearly. According to a random-effects meta-analysis, the standardised mean difference (Hedges' g) was 0.30 with a 95% confidence interval of 0.08 to 0.52 (p-value = 0.003). This suggests a moderate effect of inflow waveform on the prediction of WSS magnitude by CFD. Figure 2.4 illustrates the results provided by the meta-analysis of the effect of using generalised boundary conditions on the aneurysmal WSS magnitude. It is worth noting that in this meta-analysis study, I used aneurysmal WSS values provided by patient-specific boundary conditions as the baseline values. WSS values generated by the generalised boundary conditions can be arbitrarily higher or lower than the baseline values. However, I calculated the effect sizes in a consistent way keeping the WSS values generated by patient-specific boundary conditions as baseline for all studies. Thus, bearing in mind that the "sign" has no physical meaning in this meta-analysis, the term "overestimation" was used in consistency with other meta-analyses presented in this work.

A rigid-wall assumption is often made in cerebrovascular flow simulations [117]. Estimating regional aneurysmal wall motion from dynamic X-ray images, Dempre-Marco *et al.* [85] compared CFD simulations of blood flow in aneurysms with rigid and non-rigid wall assumptions and observed that, although the distribution of WSS on the sac and elevated WSS areas remained almost identical, rigid wall simulations tended to overestimate the pointwise aneurysmal WSS magnitude by around 50%. On the other hand, fluid structure interaction (fluid structure interaction (FSI)) techniques have been used to simulate aneurysmal flow in non-rigid aneurysmal models. Torii *et al.* [86, 87, 118] performed non-rigid fluid-structure-interaction simulations on aneurysms and reported up to 20% differences among WSS magnitudes obtained from rigid and non-rigid simulations. Takizawa *et al.* [118, 119, 120, 121], performed quantitative comparisons between maximum peak systolic aneurysmal WSS values obtained from rigid and flexible wall (fluid structure interaction) CFD simulations and reported
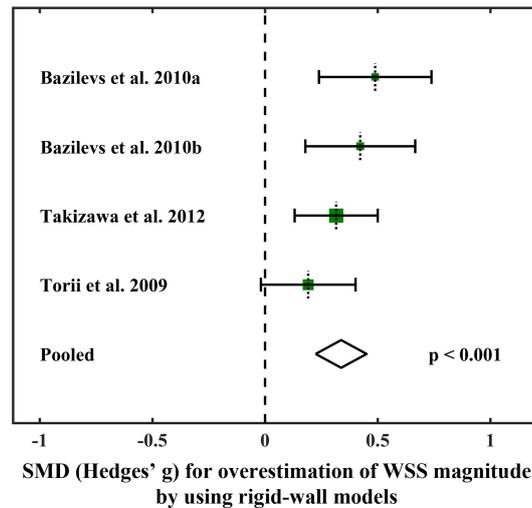
Figure 2.5: Forest plot showing the overestimation of maximum peak systolic aneurysmal WSS produced by the rigid arterial wall assumption. The plot illustrates effect sizes, Hedges' g, (represented by a square) and the confidence intervals (the horizontal lines) for each study and the pooled effect (the centre of the diamond) and its confidence interval (the width of the diamond) across all studies. Vertical dotted lines for each study show the study mean and the green squares are sized according to the study weight.

values of WSS on the aneurysm sac for different cases. According to a random-effects meta-analysis, the standardised mean difference (Hedges' g) was 0.34 with a 95% confidence interval of 0.22 to 0.45 (p-value < 0.001). Figure 2.5 illustrates the results provided by the meta-analysis.

The meta-analysis suggests an effect of wall distensibility on the prediction of WSS magnitude by CFD. However, visual inspections and quantitative comparisons based on global space-averaged measures showed an agreement between the rigid-wall and non-rigid-wall simulations as long as the distribution of WSS on the aneurysm wall, or the main characteristics of flow in the aneurysm (e.g., the complexity of flow pattern, or presence of an impinging flow jet, etc.) are of interest [31, 85, 122]. The main challenge to the current structural models of aneurysm wall is the present limitations in measurement techniques leading to uncertainties in identification of wall mechanical properties like thickness or modulus of elasticity. Aneurysms often have pathological walls with material properties varying spatially over sac. Despite some attempts to create ad hoc models of such variations, e.g. a thinner wall on the sac [123], the structural models are still far from the physiological reality. Thus, notwithstanding the important effects induced by rigid wall assumption, such issues with realistic quantification of aneurysm wall mechanics have resulted in rigid-wall CFD simulations remaining predominant in

the context of intracranial aneurysm modelling. To the best of my knowledge, the effect of using rigid-wall assumption on rupture risk stratifications and predictions of endovascular treatments' outcome has not been studied yet. However, the observed effects on WSS magnitudes, and presumably direction, magnifies the importance of future studies on non-rigid aneurysm wall models, especially when quantification of WSS and its mechanistic relation to the aneurysm wall biology and intra-aneurysmal thrombogenesis is of interest, e.g., in VETMs.

All in all, the meta-analyses found that wall distensibility and inlet flow waveform uncertainties have effects on the magnitude of aneurysmal wall shear stress predictions by CFD. Since only the maximum WSS values, representing a state of maximum stress [124] and wall deformation [121], were reported in some of the studies, thr meta-analysis on the effect of wall distensibility is based on maximum WSS. This limits the comparability of wall compliance meta-analysis with the other two meta-analyses that are based on the averaged WSS, i.e., the meta-analyses on the effect of inflow waveform and blood rheology. In future, in order to perform compliant wall simulations, improvements on the structural models of arteries and current techniques for measuring mechanical properties of the aneurysm wall are necessary. To the best of my knowledge, the effect of rigid wall assumption on the endovascular treatment predictions, and stratification and rupture risk assessment of intracranial aneurysms has not been explored yet. In addition, inter-subject variability of arterial flow rates as well as intra-subject variations of the systemic flow conditions in response to the regulatory systems lead to an uncertainty in the parent arteries' flow rate waveforms. Despite the recent studies [109, 110] on quantification of the uncertainties raised from inter-subject variability of inflow waveforms, the effect of intra-subject variability of systemic flow on aneurysmal WSS is still not attempted by the research community. Recent studies [125, 126] have revealed some new aspects of the effect of flow multi-directionality on the biological responses of the endothelium, which may play an important role in aneurysmal wall inflammation and degradation and aneurysm thrombosis by activating platelet activators [127, 128]. However, the sensitivity of WSS directionality to the above mentioned sources of uncertainty has not been well investigated in the literature. These, on the other hand, accentuate the importance of addressing geometric and flow uncertainties in the endovascular treatment models.

Uncertainties in aneurysmal blood flow modelling may also arise in outlet boundary conditions. Ramalho *et al.* [129] investigated the sensitivity of intra-aneurysmal haemodynamics to the outlet boundary conditions assigned using four different methods: traction-free, zero-pressure, coupling to a zero-dimensional model, and coupling to a one-dimensional model. They observed that coupling the outlet boundary to a zero-

dimensional or a one-dimensional model resulted in more appropriate flow distribution between the side branches. However, using the reduced-order models as boundary conditions requires proper choice of model parameters, like resistance and capacitance in zero-dimensional models, and vascular structural and mechanical properties in one-dimensional models. Uncertainty in such model parameters should be addressed to produce reliable patient-specific results, e.g. Refs [130, 131].

In addition to the uncertainties in quantifying physiological model parameters (i.e., blood density and viscosity) and boundary conditions, variabilities in discretisation strategies may influence the model outcomes. Providing a fixed set of boundary conditions and flow model parameters, the two recent CFD challenges on aneurysmal flow modelling invited CFD modellers to simulate blood flow in selected aneurysms and investigated how variations in solution strategies influence aneurysmal blood velocity and pressure quantifications. In the Aneurysm CFD Challenge 2013 [132], despite using different solution strategies and resolutions (mesh sizes of 86k-31200k using first or second order elements and time step sizes of 0.01-10 ms), approximately 80% of the 26 participating groups reported similar results with standard deviations of below 9% for cycle-averaged and peak systolic velocity, and pressure on the parent artery centreline in the two aneurysm cases studied; flow inside both studied aneurysms was stable and comparison among participating groups resulted in standard deviations below 20% for the velocity cut-planes through the aneurysm sacs. However, the aneurysmal flow inside the aneurysm involved in the Aneurysm CFD Challenge 2012 [89] was not stable and thus despite the overall agreement among the 27 submitted solutions, solutions with higher temporal resolutions (time step sizes below 0.2 ms) were able to capture flow instabilities; detection of flow instabilities by some groups resulted in greater inter-study variabilities particularly in peak systolic velocity patterns. According to the above challenges, CFD simulations with high temporal resolutions of at least 0.2 ms are required to capture aneurysmal flow instabilities. On the other hand, despite a strong correlation ($R^2 > 0.9$) between time-averaged WSS magnitudes, Valen-Sendstad *et al.* [133] observed a weak correlation ($R^2 = 0.23$) between OSI values predicted by normal (with spatial resolutions of 0.1-0.2 mm and temporal resolutions of about 1 ms) and high resolution (with spatial resolutions of about 0.06 mm and temporal resolutions of about 0.05 ms) simulations. Comparing normal and high resolution CFD simulations, they observed an average of 30% and 60% differences in pointwise values of time-averaged and maximum WSS on the aneurysm sac, respectively. They suggested that particularly for bifurcation unstable aneurysms, normal resolution CFD simulations cannot accurately capture oscillations both in magnitude and direction of WSS vectors. Due to the observed differences between OSI values and pointwise WSS magnitudes pre-

dicted by normal and high resolution schemes, Valen-Sendstad *et al.* [134] argued that although normal resolution CFD simulations may be adequate for aneurysm rupture risk assessment based on spatiotemporally averaged flow indices, they cannot be relied on to fully characterise WSS as a complex biomechanical stimuli on the aneurysm wall.

Mesh resolution near the wires also influences the flow quantification in the presence of endovascular devices. Comparing the solutions provided by 6 participating groups for three particular stented aneurysms, the Virtual Intracranial Stenting Challenge (VISC) in 2007 [88] showed that an accurate reconstruction of blood flow around the stent wires requires an adequately fine mesh resolution near the struts. Janiga *et al.* [66] observed more than 15% relative difference between intra-aneurysmal maximum flow velocities obtained based on first- and second-order numerical discretisation. They recommended second-order solvers for flow simulation in stented aneurysms.

To sum up, mesh-dependency tests are necessary when building VETMs, in particular, to ensure the convergence on the aneurysmal wall and near the device wires. Although assessments of device performance based on the highly reduced indices (e.g., flow reduction or increase in the aneurysm sac turnover time) can be done using coarser discretisations, higher resolution CFD simulations are required for an accurate resolution of velocity and WSS fields, especially when the interaction between localised haemodynamics and biology is of interest, e.g., platelet activation in the high shear flows between the struts [40], and inflammatory or thrombogenic biochemical surface reactions [126, 135]. In VETMs, CFD solutions require temporal resolutions higher than 0.2 ms to capture flow instabilities of interest, and spatial resolutions in the order of 0.1-0.2 mm within the vasculature and of about one-third of the wire radius near the wires. In addition, volumetric meshes require at least a few layers of prismatic boundary layer elements near the wall.

2.3   Modelling of endovascular devices and their deployment

Mathematical models developed for device deployment can be either mechanistic or phenomenological. Mechanistic models of device deployment dynamics account for the design and mechanical properties of the particular device and its mechanical interactions (contact) with the flow, the arterial wall, and the device itself. This makes mechanistic models potentially more accurate. However, such models have a large number of model parameters and, consequently, are more prone to uncertainty in the identification of model parameters. In contrast, while they may ignore some of the underlying biomechanical mechanisms, phenomenological models make certain geometrical or physical assumptions to describe the observable process of device deployment. These models

are computationally faster and their parameters are more easily obtainable from the device manufacturer. Therefore, phenomenological models are more commonly used for simulating virtual treatment procedures for the embolisation of aneurysms.

Mechanistic virtual coil models have been employed to describe the dynamics of coil deformation after insertion into the aneurysm sac [136, 137, 138, 139]. Such models have many ingredients to adjust in order to optimise the deployment strategy, such as the diameter, length, and mechanical properties of the coils as well as a proper set of boundary conditions describing interactions of the coil with the micro-catheter, aneurysm wall, and the coil itself. Equations of blood flow are then solved within the coiled aneurysm. Phenomenological models of endovascular coil deployment can be categorised into: (i) models that only modify the governing equations of blood flow to account for the impedance of fluid flow in the porous region of a thrombosed coil [140, 141, 142, 143, 144], and (ii) models that use mathematical descriptions to explicitly model the coil deployment inside a specific aneurysm and then solve blood flow equations in the aneurysm sac with a deployed coil inside [72, 145, 146, 147]. The dynamics of stent deployment have been mechanistically modelled using finite element models (FEMs) [29, 148, 149, 150, 151]. Such models, however, are computationally very expensive since they consider the structural properties of the stent as well as its interactions with the micro-catheter and the vascular wall. Phenomenological models describe the endovascular stent by representing it as a porous medium [152, 153], by mapping the stent design on a previously expanded cylinder inside the vessel [72, 73], by deforming a mesh until it reaches the vessel wall [28, 70, 154, 155], or by weaving stent wires around a circular cone deformed to fit against the vessel wall [27]. Flore *et al.* [150] and Bernardini *et al.* [148] compared aneurysmal flow after placement of an endovascular stent with a mechanistic FE model with that predicted after deploying the stent using a phenomenological fast virtual deployment model and observed a good quantitative agreement accompanied by a reduction in the computational time.

Virtual treatment models have been used to pre-operatively study the effect of coil shape, orientation, and packing density in patient-specific aneurysm models. Schirmer *et al.* [147] investigated the effect of orientation of helical coils on the aneurysmal flow and showed that the coil orientation with respect to the aneurysmal flow has a considerable influence of the effectiveness of helical coils. They showed that helical coils that are located parallel to the flow jet entering the aneurysm are more effective in preventing flow from entering the aneurysm and reducing the level of aneurysmal WSS. They observed the least flow reduction in aneurysms with coils placed orthogonal to the entering jet. Similarly, Jeong *et al.* [156] investigated the effect of coil shape and orientation on the aneurysmal haemodynamics and showed that cage-shaped coils deployed

orthogonally to the entering flow jet provided the least flow reduction in aneurysms. Agiilar *et al.* [157] studied the effect of coil surface area (diameter) and packing density on the intra-aneurysmal flow. They observed that coiled aneurysms with the same coil surface area but different packing densities produced similar intra-aneurysmal haemodynamics. They also observed that the coiled aneurysm with the largest coil surface area had the most effect on flow reduction and concluded that the coil surface area influenced on its performance. Morales *et al.* [158] studied the effect of coil packing density and configuration on the intra-aneurysmal flow and showed that at low packing densities ($< 12\%$), the aneurysmal flow was highly dependent on the coil configuration and this dependency decreased as packing density grew. They observed an insignificant influence of coil configuration at high packing densities.

Aneurysmal haemodynamics following the placement of a flow diverter stent are known to be dependent on the aneurysm size and shape [159, 160, 161, 162], location [159, 161], stent design and configuration [149, 155, 163, 164, 165, 166], and its orientation and position in the parent vessel [165, 167, 168, 169]. The stent porosity has also been shown to highly influence the effectiveness of the deployed stent [170, 171]. Virtual treatment models provide the opportunity to investigate the effect of the aforementioned variables using image-based patient specific models before the actual placement of flow diverters [33]. In clinical practice, flow diverters are usually selected to be oversized, i.e., to have slightly greater diameter than the vascular calibre. This results in an adequate appositioning against the vascular wall on the one hand and a stretch of stent cells along the vascular axis on the other. Mut *et al.* [172] studied the effect of stent oversizing on the post-treatment aneurysmal haemodynamics and showed that oversizing will result in larger stent cells and will decrease the haemodynamic effectiveness of the flow diverter stent. While deploying flow diverters, clinicians can maximise the strut local compaction, and consequently the flow diversion, across the aneurysm neck. The dynamic push-pull flow diverter deployment technique has been used to increase and decrease the local density of the flow diverter at the aneurysm neck and perforator-rich regions of the parent vessel, respectively, to allow maximum flow diversion at the neck while maintaining the perforators and branch vessels [173]. Janiga *et al.* [174] simulated flow through similar flow diverters that are differently deployed to have eight different local compactions at the neck; and, observed that different local compactions lead to different post-deployment intra-aneurysmal flow reductions ranging from 24.4% to 33.4%. They remarked that flow diverter local compaction across the aneurysm neck can be virtually and pre-operatively optimised to reach maximum flow reduction. However, Xiang *et al.* [40] simulated this deployment technique and showed that although resulting in an increased flow diversion, it pushes the flow di-

verter to bulge out inside the aneurysm, and produces a weaker inflow compared to the standard deployment technique that results in lower shear rates near the stent struts. Since high shear-induced activation of platelets plays a role generation of a stable white thrombus (versus instable stasis-induced red thrombus) inside the aneurysms, Xiang *et al.* [40] suggested that this deployment technique may result in lowering the platelet activation and, consequently, white thrombus formation potential.

Performance of endovascular devices in treatment of aneurysms is assessed by their ability to induce a flow stasis and consequently an occluding stable blood clot in the aneurysm sac [20]. Virtual endovascular treatment models can be used to pre-operatively predict the likelihood of recanalisation in candidate aneurysms for coil embolisation. Presence of high WSS (> 35 Pa as reported by Refs [175, 176]) at the neck of the coiled aneurysms was shown to have a correlation with post-treatment recanalisation and regions of high WSS coincided with regions where recanalisation happened [175, 176, 177, 178]. Delayed or incomplete occlusion and post-treatment rupture are the challenging complications associated with flow diverter treatments. Currently, there is no reliable measure to predict the performance of implanted flow diverters in terms of inducing a durable clot that occludes the sac completely and triggers the process of healing. Several attempts have been made to computationally quantify the stent-induced post-treatment haemodynamic alterations and use them to predict the treatment outcomes. Chung *et al.* [179] evaluated the treatment outcome in 36 rabbits with elastase-induced aneurysms treated with flow diverters; nine aneurysms were occluded completely or near completely within 4 weeks (categorised as fast group) and six aneurysms incompletely occluded at 8 weeks (categorised as slow group); differences were observed between the morphological indices of the two groups; e.g., neck area was 0.365 ± 0.082 cm^2 in the slow and 0.144 ± 0.078 cm^2 in the fast occlusion group, p-value = 0.015. However, from haemodynamic measures (measured immediately after stent deployment), the aneurysm inflow rate and mean intra-aneurysmal velocity were lower in the fast occlusion group (inflow rate was 0.155 ± 0.095 mL/s in the slow and 0.047 ± 0.053 mL/s in the fast occlusion group, p-value = 0.024 and intra-aneurysmal velocity was 0.506 ± 0.298 cm/s in the slow and 0.221 ± 0.224 cm/s in the fast occlusion group, p-value = 0.058); no differences were observed between WSS-based measures (e.g., space-averaged WSS, minimum WSS, or low WSS areas). Mut *et al.* [180] examined post-stent aneurysm flow in 23 aneurysms (15 aneurysms considered as fast with occlusion times less than 3 months, and the other 8 considered as slow with incomplete occlusion or patency at 6 months); they found differences in post-treatment inflow rate (1.89 ± 1.88 mL/s in the slow and 0.47 ± 0.52 mL/s in the fast group, p-value = 0.021), mean velocity (3.11 ± 2.04 cm/s in the slow and 1.13 ± 0.92 cm/s in the fast

group, p-value = 0.004), and shear rate (32.37±20.93 /s in the slow and 20.52±23.18 /s in the fast group, p-value = 0.021) values between the fast and slow groups; they suggested a threshold of 1.3 cm/s on post-stent mean velocity could predict occlusion time (slow or fast) with an accuracy of 84%. Kulcsar *et al.* [181] examined pre- and post-treatment haemodynamics in eight para-ophthalmic aneurysms treated with flow diverters; one was occluded but ruptured 5 day after treatment, one remained patent after one year, and others were occluded during the one year follow-up. In aneurysms with complete occlusion, they observed reductions of 10%-80% in the mean velocity, 12%-58% in the maximum velocity, 44%-81% in the mean WSS, and 32%-82% in the maximum WSS after flow diverter placement; however, mean and maximum velocities, and mean and maximum WSS were reduced by 60% and 47%, and 68% and 60% in the aneurysm that remained patent, respectively. In the aneurysm with post-treatment rupture, Kulcsar *et al.* [181] also observed 20% and 0% reductions in the mean and maximum velocities, respectively, while the mean WSS was reduced by 60% and a reduction of 20% was observed in the maximum WSS after stenting. They pointed out that lower reduction rate in the maximum velocity of the ruptured aneurysm suggests a persisting jet that prevents the successful occlusion of this aneurysm. However, based on the observations reported by Kulcsar *et al.* [181], the averaged haemodynamic measures in the case with persisting patency are not significantly different from those aneurysms with successful occlusion. Focusing on the relative changes (post- to pre-treatment ratio) induced by flow diverters, Ouared *et al.* [182] attempted to find patient-unspecific haemodynamic ratio thresholds that significantly determine the condition required for a durable aneurysm occlusion; they examined pre- and post-stent space-and-time-averaged velocity and WSS in 12 aneurysms (nine were occluded at 12 months' follow-up while the remaining three were still patent) but found no significant absolute occlusion threshold based on post-stent velocity and WSS absolute values; however, they found an area under curve (AUC) with a p-value of only 0.052 for pre- to post-stent mean velocity ratio with a minimum of one-third velocity reduction necessary to generate a long-term occlusion (with a sensitivity and specificity of about 99% and 67%, respectively), independent of the aneurysm geometry; despite post-treatment WSS reductions in all aneurysms, they could not find any significant occlusion threshold based on post- to pre-stent WSS ratios.

The above-mentioned studies identified reductions in aneurysmal flow and WSS following the treatment with endovascular devices; however, most of them found no significant haemodynamic differences between cases with successful occlusions or persisting patency. Although the observed post-treatment haemodynamic changes suggest the capability of pure haemodynamic models in predicting the treatment outcomes, the

limited sample sizes in each individual study prevents any general conclusion; for example, all aneurysms included in the study by Kulcsar *et al.* [181] have post-treatment mean velocities greater than that suggested by Mut *et al.* [180] as a fast occlusion threshold; or the so called patient-unspecific velocity reduction occlusion threshold proposed by Ouared *et al.* [182] results in a sensitivity and specificity of about 67% and 50% in the cohort studied by Kulcsar *et al.* [181]. Despite the hypothesised important role of WSS on aneurysm wall biology and initiation of thrombosis, none of the reviewed studies identified a significant difference between the fast and slow occlusion outcomes based on averaged WSS-based measures; this could be attributed to the highly localised patterns of aneurysmal WSS and the consequent biological aneurysm wall phenotypes that are not captured by the averaged quantities studied in the mentioned works. Moreover, inducing a selective aneurysmal clotting that triggers the healing process is crucial [183]. Unlike the stasis-induced red thrombus, which is less organised and contains a high content of leukocytes and proteolytic enzymes, white thrombus is more stable and contains a low content of leukocytes and proteolytic enzymes [40]. Unstable red thrombus forms under low shear flow; conversely, white thrombus forms through activation of platelets in high shear rate regions (e.g., near the stent struts) [40]. Recent findings on post-procedural ruptures of aneurysms treated with flow diverters suggest that the presence of fresh and non-organised red thrombus may result in a pathophysiological cascade leading to aneurysm wall degradation and rupture [39]. This revealed that device-induced intra-aneurysmal flow stasis may result in formation of unorganised red thrombus and lead to aneurysm rupture after treatment. Xiang *et al.* [40] hypothesised that white thrombus should desirably be induced in the aneurysm to promote stabilisation red thrombus and generate a stable clot that assist in the formation of a neointimal layer over the aneurysm neck. The hypothesis that the stable intra-aneurysmal clot is a combination of red (forms via stent-induced stasis) and white (forms via stent-induced platelet activation) thrombi needs further investigation and validation [40]. This hypothesis also magnifies the importance of appropriate anticoagulant/antiplatelet therapies in such complex problems [40, 183]. Summing up, the favourable treatment outcome, i.e., formation of a complete stable clot at a rate faster than thrombus-induced wall degradation, however, is highly affected by the mechanical and biochemical interactions between clot and intra-aneurysmal flow, in the presence of the anticoagulant/antiplatelet therapies. The above discussion implies that whether or not an implanted endovascular device leads to a complete aneurysm occlusion may not be assessed only based on post-treatment highly averaged haemodynamic quantities. Information from the intra-aneurysmal biochemistry and biology is required to reliably predict device performance. This could

be achieved by coupling mechanistic blood coagulation sub-models to the VETMs or devising more advanced phenomenological haemodynamic surrogates that capture the ongoing biological processes more effectively. Creating device performance indicators that compare the device-induced formation rates of unstable red versus stable white thrombi in the presence of anticoagulant/antiplatelet therapies may help predict the efficacy of an endovascular device for a specific patient.

2.3.1 Uncertainty in modelling of the endovascular devices

Uncertainty in modelling of the endovascular devices can arise either from uncertain model parameters or the way each model represents deployment of the device and its interaction with blood flow (model uncertainty). Phenomenological models of coil and stent deployment often rely on parameters such as device design, diameter, and length, which are often obtainable from the manufacturer. However, mechanistic models include mechanical properties of the devices and boundary conditions, which cannot be easily measured, and thus, introduce uncertainty into the model. The effect of device configuration, orientation, and position of the devices has been investigated in the literature, but to the best of my knowledge, the quantification of the uncertainty in the model parameters has not been attempted so far.

Modelling endovascular devices as porous media, although is not strictly a source of uncertainty, introduces errors in quantification of aneurysmal flow; especially local values of haemodynamic variables. Morales *et al.* [30] compared post-treatment aneurysmal flow fields obtained from modelling the deployed coil as a porous medium with that obtained from modelling the coils explicitly. They observed considerable differences in intra-aneurysmal velocity and local concentration of contrast agent predicted by each of the two techniques. However, due to the lack of quantitative comparisons between post-treatment aneurysmal flow fields obtained from models and in vivo measurements, it is not yet certain, which of the proposed models better represents the device performance under specific conditions. Levitt *et al.* [184] compared post-treatment haemodynamics in two coiled aneurysm phantoms numerically simulated using the porous medium technique and explicit model of coils obtained from high-resolution high-energy synchrotron X-ray micro-tomography; substantial differences up to 50% and 130% respectively in time-averaged WSS and OSI values averaged over the aneurysm sacs suggest inaccurate haemodynamic quantifications using homogeneous porous medium coil models. Although synchrotron tomography is not currently available in the routine clinical practice, this modality can be used to evaluate the accuracy of other more complex coil modelling techniques. In two of the three stented aneurysms, Raschi *et al.* [185] reported a qualitative and quantitative agreement (with up to 10%

difference in post-treatment reductions in aneurysm-averaged WSS) between aneurysmal post-treatment haemodynamics predicted by explicit and porous medium models of the deployed stents; in the third aneurysm, post-treatment reduction in aneurysm averaged WSS differed up to 25% between the porous medium and explicit models of the flow diverters. In a similar study with two stented aneurysms, identical WSS distributions with relative root mean square errors of 21%-24% in mean WSS magnitude averaged over the entire sac and 45%-81% in mean WSS magnitude averaged over the aneurysm dome are reported for simulations with flow diverters modelled either as porous medium or explicitly [152]. Capturing the local variations of porosity is a challenge in porous medium models of both coils and flow diverters. For example, complex geometry of the host artery, or particular deployment techniques (e.g., the push-pull technique) result in local variation of stent porosity at the aneurysm neck which cannot be easily mimicked by the porous medium models; especially if pre-operative evaluations of the devices are of interest so that the post-deployment porosities cannot be estimated by micro-tomography techniques. Thus, although refinements may improve on the predictions by encouragingly cost-effective porous medium models, the geometrical complexity of endovascular devices and the consequent effects on the flow seem to be a serious challenge to these models.

Intra-procedural changes in the host vessel geometry (shape and size) introduce further uncertainties in VETMs that has yet to be studied in more detail and quantified. The parent vessel can undergo dilation as a consequence of stent expansion during deployment, vasodilator drug administration, and the intentional post-release manipulations to correct stent apposition all leading to reported differences of about 5% and 10%, respectively, between virtual and real stent final radius and length [186]. Delayed geometrical and angular alterations of the host arteries within a year after deployment are also reported in stented aneurysms [187]. Straightening of the parent artery after deployment of stents was reported by King *et al.* [188]. In sidewall vertebral artery aneurysms, this resulted in alterations in the flow direction and rate (by 10%) of the aneurysm inflow jet [189]. However, none of the current deployment techniques accounted for such device-induced geometrical alterations [66]. Formation of a rapid and stable clot, which completely occludes the aneurysm sac, is the desired goal of a successful endovascular aneurysm treatment [190]; and, uncertain intra-procedural alterations in the physiological flow can affect the treatment outcome. Mut *et al.* [191] investigated intra-aneurysmal haemodynamics in aneurysms treated with three different stents under five different time-averaged flow rates in the parent vessel and observed that a change of 30-50% in the parent vessel flow rate during the stenting procedure resulted in a 30-80% change in the aneurysmal haemodynamic variables. This obser-

vation highlights the importance of inlet flow variability as a source of uncertainty (see the uncertainty in blood flow modelling section) in vascular treatment models.

2.4   Modelling of blood clotting

2.4.1   Clotting in aneurysms

In ruptured intracranial aneurysms, clot formation is the response of the haemostatic system and prevents blood loss at the site of injury, where the aneurysm has burst. Chronic spontaneous thrombosis can also occur in unruptured aneurysms, resulting in further wall damage and later aneurysm rupture or a natural healing process through complete occlusion of the aneurysm sac [192]. On the other hand, as mentioned before, intrasaccular thrombosis can also be induced by endovascular devices, like coils and stents, to occlude the aneurysm sac and isolate it from the vascular bed and reduce the rupture risk.

The desired process of healing in endovascular treatment is to generate a stable clot throughout the aneurysm sac. The aneurysm will then be excluded from the parent vessel by formation of a neointimal layer over the aneurysm neck [193, 194, 195]. Endovascular treatments are associated with complications such as incomplete occlusion, recanalisation or recurrence [196, 197], and thromboembolisation [198], which expose the patient to the risk of a later haemorrhage or an ischemic stroke. Anticoagulant drugs are usually prescribed after endovascular treatments [199], and prevent uncontrolled acute device-induced thrombus formation and reduce the risk of thromboembolisation on one hand and prolong the endosaccular clot formation on the other. Due to the prolonged treatment procedure, further wall inflammation and damage may occur due to the presence of an incomplete clot partially covering the aneurysm wall, increasing the risk of post-treatment rupture [39, 200]. Moreover, the increased time of clotting due to the prescription of antiplatelets and anticoagulants can further increase the risk of bleeding in patients with endovascular treatments [199].

2.4.2   Mechanisms of intra-aneurysmal thrombosis

It has been thought that adverse haemodynamic conditions at the aneurysm wall may result in wall inflammation and damage to the endothelium [38]. Aneurysm wall is often characterised by dysfunction/loss of endothelium [200]. The cell-based model of coagulation [201] provides an explanation for spontaneous thrombosis resulting from the endothelial damage and exposure of vascular tissue factor (TF) to the circulating blood in the aneurysm sac. WSS at regions where flow is low and multidirectional or

at regions where flow variations are dominated by frequencies higher than the systemic flow frequency (the heart rate) have been shown to correlate with the pro-inflammatory response of the endothelial cells [135, 202]. Inflamed endothelium expresses the NF-κB transcription factor (a nuclear transcription factor that can be activated by environmental signals, like WSS, and mediate wall inflammation and weakening), leading to upregulation of blood borne TF, which can subsequently trigger spontaneous thrombosis in such regions [203, 204]. Platelet activation and aggregation within the recirculation regions followed by deposition in regions of low flow has also been used to explain spontaneous coagulation in aneurysms [205, 206].

As far as device-induced coagulation in aneurysms is considered, pro-coagulant alterations in aneurysm haemodynamics, platelet activation as a result of blood contact with the deployed devices, and shear-induced platelet activation are key factors in initiating endosaccular thrombosis. Intra-aneurysmal flow reduction using endovascular devices is thought to create dead zones where the flow stasis favours platelet adhesion and activation, a key step in the thrombosis process [40, 41]. Such flow stasis can also be associated with damage to the endothelium and exposure of the sub-endothelial TF [207]. Blood contact with the artificial material (the deployed devices) is hypothesised to also be responsible for the initiation of blood coagulation inside the aneurysm sac [208, 209]. Xiang *et al.* [40] suggested that platelets can become activated in high-shear regions near the flow diverter stent struts and can be transferred to and deposited in low-flow regions in the sac. They further distinguished between white and red thrombi, where the former favours aneurysm healing and the latter leads to further wall weakening and the ultimate aneurysm rupture after flow diverter placement.

2.4.3   Computational models for spontaneous thrombosis in aneurysms

The most challenging part of a mechanistic model of thrombus formation in aneurysms is the mechanism used to describe thrombosis initiation. It has been observed that blood clots form or at least deposit in the regions where blood flow is extremely low and multidirectional [43, 210, 211, 212]. However, it is not yet well understood whether clotting starts extrinsically due to the endothelial damage and TF exposure in disturbed flow regions, i.e., aneurysmal wall regions where haemodynamic stresses are extremely low and multidirectional; or, intrinsically due to platelet activation and aggregation and exposure of blood borne TF under certain haemodynamic conditions [213]. Coagulation models in aneurysms can be classified into two main groups. The former only characterise blood flow in aneurysms and do not include any biochemical reactions. The latter, however, couple both flow and reaction to model coagulation in aneurysms. Some models include additional parts that consider the mechanical interactions be-

tween the clot and the blood flow field.

Rayz *et al.* [43, 214] and Ouared *et al.* [42, 215] correlated flow velocity, flow residence time residence time (RT) and WSS with clot formation and simulated clotting in aneurysms without considering the biochemical reactions. For three patients with magnetic resonance imaging scans before and after thrombus formation, Rayz *et al.* [214] showed that blood clots developed in regions with low WSS and high RT. They revealed a correlation between the location of intraluminal blood clots and regions of high RT and low WSS. Zimny *et al.* [216] classified thrombosis initiation mechanisms in aneurysms into intrinsic and extrinsic mechanisms. In their multiscale model, intrinsic mechanisms initiated clotting through platelet activation by the inflamed wall or by the contact of blood with external devices (e.g., coils and stents) and extrinsic mechanisms initiate clotting through exposure of TF due to damage to the aneurysm wall. Such damage was considered to be a result of post-treatment flow alterations in the sac or any damage that occurred during the deployment procedure. They finally extended the mesoscale model presented by Ouared *et al.* [42, 215] to a three-dimensional aneurysm model and simulated flow-mediated thrombus generation based on a threshold on aneurysmal WSS under which thrombosis initiates. deSousa *et al.* [41] simulated flow in ten patient-specific aneurysms and showed that spontaneous thrombosis was present in aneurysms with low shear rate and suppressed pulsatility. They also showed for three aneurysms treated with flow diverters that after flow diverter deployment, the aneurysmal shear rate fell below a certain threshold that has been correlated with the onset of thrombosis generation.

Although such models can provide some information about the possibility of presence of endosaccular thrombosis under certain aneurysmal morphology or haemodynamic environment, they will not provide enough information about the morphology of the aneurysmal blood clot and its interaction with the aneurysmal blood flow. Since these models do not include the underlying biochemical reactions, they cannot be used to predict effects of the chemical composition of blood or use of anticoagulants on spontaneous clotting or the final outcome of endovascular treatment. Coupling blood flow with a network of biochemical reactions, Bedekar *et al.* [44] and Biasetti *et al.* [217] simulated clot formation in intracranial and abdominal aortic aneurysms, respectively. They both used TF exposure on the aneurysm wall as the initiator of the clotting process and assigned a prescribed concentration of TF on the aneurysm wall as boundary condition. This approach benefited from a biochemical web of surface reactions to model clot formation on the aneurysm wall; however, it assumed that TF was uniformly exposed on the aneurysm wall and initiated the coagulation cascade. On the contrary, it has been observed that inflammatory lesions and endothelial damage, which

are thought to be responsible for TF exposure, are localised phenomena resulted from region-specific adverse haemodynamic conditions. Malaspinas *et al.* [211] set up a series of in vitro experiments and obtained WSS thresholds below which coagulation starts in idealised aneurysm geometries. Then, they used those thresholds to simulate clotting in two real aneurysms and successfully validated their results against patient-specific medical images. Although Malaspinas *et al.* [211] took a threshold-based approach to study spontaneous clotting in aneurysms, they simulated the underlying biochemical reactions; that is, the threshold has been used as the initiator of a web of chemical reactions. This makes their model capable of investigating the effect of patient-specific deficiencies in certain coagulation factors and/or the effect of anticoagulants on the clotting time and the final percentage of aneurysm occlusion.

2.4.4   Computational models for device-induced thrombosis in aneurysms

Xiang *et al.* [40] presented a model of blood flow in stented aneurysms, and demonstrated that blood flow near stent struts can provide shear rates high enough to activate platelets and trigger blood coagulation in the aneurysm sac where the flow is low enough for platelets to aggregate. Ngoepe *et al.* [45] coupled flow and biochemistry to simulate both spontaneous and stent-induced thrombosis in patient-specific aneurysm geometries. They used a level-set method to track the clot surface at each instance of the time and consider the effect of clot on the flow domain. They considered vascular TF as the sole initiator of the clotting process; however, instead of a uniform exposure of TF on the aneurysm wall, they used a shear rate threshold below which TF can be expressed on the wall and initiate the clotting process. This allowed coagulation to start only on the portions of the endothelium that are expected to be damaged, which is more physiologically relevant than exposing TF uniformly on the aneurysm lumen.

Recently, observing the fact blood clotting in aneurysms is not necessarily triggered by the exposure of TF due to the wall damage, Ou *et al.* [212] presented a model with more emphasis on the blood-borne TF as the initiator of stasis-induced thrombosis in aneurysms. To concentrate on the role played by the blood-borne TF, they ignored exposure of TF on the sub-endothelium and thrombogenicity of the flow-diverter. They hypothesised that accumulation of blood-borne TF in aneurysmal dead zones, where flow is low enough, is responsible for the initiation of thrombosis in those regions. The validity of their proposed model was supported by in vivo observations of surgically induced stasis in ligated right common carotid arteries of rats.
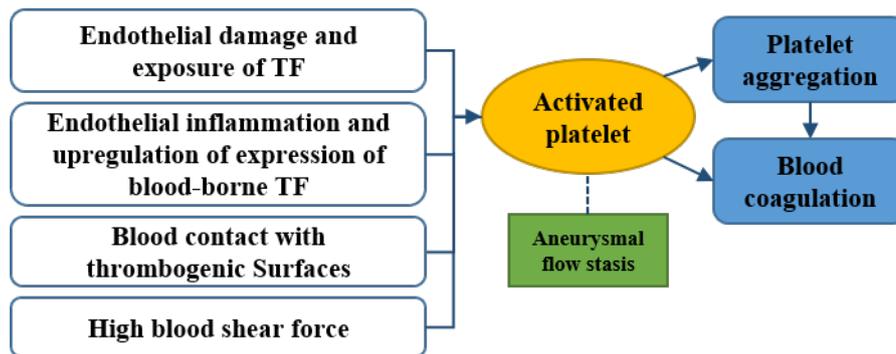
Figure 2.6: Possible mechanisms of intra-aneurysmal thrombosis.

2.4.5 Uncertainty in computational models of blood coagulation

Blood coagulation, either as part of haemostatic system or under pathological conditions, is a very complex system with several sources of uncertainty. One may consider the lack of in vivo experimental data and the limited knowledge on the underlying pro- and anticoagulant mechanisms as the main sources of uncertainty in such a complex process. It has been implied that neither cascade nor cell-based models of coagulation can satisfactorily explain in vivo coagulation in pathologies like intracranial aneurysms [209]. The role of the vessel wall in chemical initiation and hosting the coagulation process and interactive effects of the clot and blood flow field are still uncertain [44, 45, 218].

According to Virchow's triad, thrombosis can be initiated as a result of damage to the endothelium, damage to the blood itself, or under certain blood flow conditions. Particularly, as depicted in Figure 2.6, coagulation in aneurysms can be initiated due to 1) platelet activation as a result of endothelial damage and contact of blood with the vascular TF, 2) platelet activation as a response to upregulation of the blood-borne TF due to pro-inflammatory response of the endothelium, 3) platelet activation as a result of blood contact with thrombogenic surface of endovascular implants, and 4) platelet activation as a response to high blood shear force at high shear regions like near the flow-diverter struts. Blood stasis (dead zones) in complex aneurysmal geometries is always a favourable region for activated platelets to deposit and trigger blood coagulation. When considering blood coagulation in a given aneurysm, it is unclear beforehand if any or all of the above mentioned mechanisms are responsible for initiation or amplification of the thrombosis. Moreover, none of the current models developed to simulate blood coagulation in aneurysms include all of the above mechanisms or measure the relative importance of them for a particular aneurysm.

Insufficient experimental data and uncertain role of the coagulation factors can even

increase the level of uncertainty of the current models. For example, activation of the coagulation factor XII (a coagulation plasma protein that can be activated on artificial surfaces) in the presence of endovascular implants, which plays an important role in amplification of the coagulation, is not included in the cell-based model of coagulation [208].

Intra-subject variability in blood composition and pathologic deficiencies of certain coagulation factors can also increase the amount of uncertainty in coagulation modelling. It has been shown that uncertainty in the concentration of certain coagulation factors can result in completely different thrombin generation curves in a single patient. This can even be generalised to inter-subject, age-, sex-, and lifestyle-related variabilities in concentration of coagulation factors. These variabilities can also affect kinetics of the underlying reactions in terms of their rate constants. Danforth *et al.* [219] and Luan *et al.* [220, 220] investigated uncertainties in the reaction rate constants and showed that the predictive capability of the entire model is highly sensitive to variabilities in some of the numerous rate constants involved in a biochemical model of coagulation.

2.5 Conclusions

Endovascular treatment of intracranial aneurysms requires evaluating the best treatment options in terms of efficacy and safety. Whether a certain endovascular treatment leads to formation of a stable clot in a specific aneurysm is a question that challenges neurointerventionalists. Endovascular planning systems that would allow pre-interventional assessment of aneurysmal haemodynamics before and after virtual treatment are potentially valuable clinical tools. Underpinning such systems, CFD alongside other computational techniques for creating image-based vascular surface models and models of endovascular devices have already been extensively used to characterise intra-aneurysmal blood flow, and to understand the interplay between blood flow, aneurysm rupture risk, and endovascular treatment outcome. This paper overviewed the state-of-the-art in this area; and highlighted the importance of future efforts concentrating in device-induced thrombosis and uncertainty modelling in the context of VETMs.

We have presented a review of the current status of vascular anatomy and blood flow models, endovascular device deployment models, and blood coagulation models as the main ingredients that can be integrated into a VETM to help clinicians in the management of intracranial aneurysms. To provide a complete picture of treatment outcome, current systems for VETM need to be extended to incorporate post-

treatment aneurysmal response and account, for instance, for the mechanisms of clot formation in the presence of endovascular devices. Although efforts exist to model intra-aneurysmal blood coagulation [219, 221], none of the current models include all of the underlying mechanisms of intra-aneurysmal coagulation (see Figure 2.6) or measure the relative importance of them for a particular aneurysm. Most of the models have not been personalised or are difficult to personalise based on available patient-specific data. Stratification [222, 223] and success criteria for endovascular treatment need to be established that objectively define the ideal outcome in a way that could be used by the modelling community as part of a treatment optimisation framework. Therefore, future research will have to first bridge the gap between available empirical evidence from clinical studies as to what constitutes and leads to a successful treatment outcome and the technical ability to computationally model the complex interplay between factors due to the anatomy, haemodynamics, blood clot, and endovascular device. This underlying complexity, on the other hand, will have to be modelled in a judiciously simplified manner not only to make the problem computationally tractable while remaining faithful to key mechanisms but also to enable personalisation of model parameters to limited patient-specific data. At the same time, current attempts to create advanced haemodynamic surrogates for intra-aneurysmal biological phenotypes (e.g. thrombosis) [41, 43, 214, 224], should be further validated against in vivo observations and potentially used to develop more accurate predictors of intra-aneurysmal thrombosis that those attainable by simulating even simplified models the underlying complex biological mechanisms.

In an editorial, Kallmes *et al.* [46] expressed concerns regarding the status of computational studies on intracranial aneurysms and their clinical relevance. Two challenges were raised: 1) Can the VETM be used to predict flow quantities that are useful in clinical diagnosis and prognosis? 2) Do the numerous modelling assumptions and related uncertainties make the results questionable? In another editorial, Cebral *et al.* [225] emphasised that certain approximations and simplifications are needed in CFD studies to make them more cost effective and feasible. They suggested that what is important is measuring the effect of those assumptions on model outcomes and their relative importance, which could be evaluated using sensitivity analysis techniques. In this work, I have reviewed the three main ingredients of an image-based patient-specific virtual endovascular treatment model for intracranial aneurysms. Each of these sub-models is prone to uncertainties, which should be addressed in order to make the virtual endovascular treatment model reliable as well as patient-specific. For those uncertainties that I found enough quantitative analyses, meta-analyses were performed to identify their pooled effect. As presented in Table 1, uncertainties were categorised into: 1) those

for which a meta-analysis has been performed and thus their effects are supported by the highest level of evidence, 2) those which have been studied in the literature but for which I could not perform a meta analysis due to effects not being reported quantitatively or having only been considered in a limited number of studies, and 3) those which have not been studied yet in the context of IAs and thus their effect on the model outcomes is not still clear.

Virtual endovascular treatment models are influenced by several sources of uncertainty that need to be accounted for when interpreting the results of their predictions. Uncertainty handling is relevant to most computational biomechanics problems but can become particularly severe in complex multi-scale models. Meta-analyses have been performed on three well-known sources of uncertainty, and the uncertainties arising from vascular wall distensibility and inflow waveform variabilities showed effect sizes (Hedge's g) of 0.34, 95% CI [0.22, 0.45], p-value < 0.001, and 0.3, 95% CI [0.08, 0.52], p-value = 0.003, respectively. Significance of non-rigid FSI models in future understanding of complex biomechanical processes at the aneurysm wall has also been pointed out by Chung *et al.* [122]. Physiologically realistic FSI models of aneurysms require measuring local variations of wall mechanical properties over highly heterogeneous pathologic aneurysms' wall which is not easily achievable in routine clinical practice. In future, such uncertainties should be addressed by 1) using more accurate techniques for measuring model input parameters (uncertainty mitigation), 2) consideration to the propagation of uncertainties from input parameters into the model outputs by reporting confidence intervals and sensitivities instead of deterministic results (uncertainty exploration), or 3) replacing model outputs with other alternative variables, which carry the same information but are less sensitive to the unknown model parameters (sensitivity reduction). Specifically, more advanced imaging techniques can provide higher quality images of the vascular lumen along with fully automatic segmentation techniques that do not require a posteriori manual editing and can eliminate some of the geometric uncertainty. Conducting more experimental studies regarding the mechanisms underlying thrombosis, particularly in aneurysms, can reduce model uncertainties in aneurysmal clotting and thus produce more reliable virtual treatment outcome predictions. However, inherent uncertainties in the systemic flow (and several other model parameters) cannot be eliminated. In such cases, advanced uncertainty quantification techniques [130, 226, 227] can be used to systematically explore the effects of these uncertainties. The concept of personalisation should not be limited to deterministic identification of model parameters at a particular moment in time. Instead, model parameters should be treated as uncertain and/or fluctuating quantities; and uncertainty quantification techniques should be employed to propagate those uncertainties through the virtual

treatment models in order to produce confidence intervals and sensitivities associated with the model predictions.

Table 2.1: Major sources of uncertainty in different sub-models of a typical endovascular treatment model.

a) Uncertainties for which a meta-analysis has been performed		
Source of uncertainty	Reference(s)	Summary effect (Hedges' g) Mean (95% CI)
Wall distensibility	Torii *et al.* [118] Bazilevs *et al.* [120] Bazilevs *et al.* [121] Takizawa *et al.* [119]	0.34 (0.22 − 0.45)
Inlet flow rate waveform (inter-subject variability)	Karmonik *et al.* [106] McGah *et al.* [105] Jansen *et al.* [103]	0.02 (-0.04 − 0.07)
Blood rheology	Fisher *et al.* [97] Morales *et al.* [98] Castro *et al.* [96]	0.30 (0.08 − 0.52)

b) Uncertainties for which a meta-analysis has not been performed		
Source of uncertainty	Reference(s)	Main findings
Segmentation and reconstruction accuracy	Cebral *et al.* [31] Castro *et al.* [61] Gambaruto *et al.* [62] Geers *et al.* [57] Mikhal *et al.* [228] Schneiders *et al.* [229]	Overestimation of neck size by CTA compared to 3DRA lead to a 44.2% difference in time-and-space-averaged WSS over the aneurysm sac. Overestimation of neck size by 3DRA compared to 2D DSA lead to differences up to 98% in maximal WSS over the aneurysm sac. Reconstruction smoothing level can affect aneurysmal WSS by 15%. Reconstruction of aneurysm and parent vessel surface models significantly affect aneurysmal haemodynamics. Special care should be taken about removing kissing vessels, overestimation of aneurysm neck size by CTA and 3DRA, smoothing levels, and parent vessel reconstruction.
Length of parent vessel proximal to the aneurysm	Pereira *et al.* [114] Hodis *et al.* [115] Valen-Sendstad *et al.* [112]	Length of proximal parent vessel have a large effect on the aneurysmal haemodynamics (approximately 20% on the aneurysmal WSS). Parent vessels should at least be truncated as far upstream as images allow, preferably below the cavernous segment on ICA.

Continuation of Table 2.1.b) Uncertainties for which a meta-analysis has not been performed		
Source of uncertainty	Reference(s)	Main findings
Outlet boundary conditions	Ramalho *et al.* [129]	Outflow boundary conditions highly influence the aneurysmal haemodynamics (approximately 20% on the aneurysmal WSS) when multiple outlets are present. 0D and 1D outlet boundary conditions provide realistic flow split between branches when tuned carefully.
Moving parent arteries	Sforza *et al.* [230]	Pulsating intracranial vasculature motion has small effects on the aneurysmal haemodynamics (less than 5% on the aneurysmal WSS).
Using different CFD solvers	Steinman *et al.* [89]	Standard deviations of below 9% for cycle-averaged and peak systolic velocity and pressure.
Discretisation schemes	Valen-Sendstad *et al.* [134]	Strong correlation ($R^2 > 0.9$) between time-averaged WSS magnitudes between values obtained from normal and high resolution simulations. Weak correlation ($R^2 = 0.23$) between OSI values predicted by normal and high resolution simulations.
Endovascular device deployment model structure (imprecise governing equations)	Morales *et al.* [30] Levitt *et al.* [184] Raschi *et al.* [185] Augsburger *et al.* [152]	Modelling aneurysmal coils explicitly or approximating them by a porous medium will highly affect the predictions of post-treatment haemodynamics (approximately 70% difference in the post-treatment intra-aneurysmal velocity). Differences up to 50% and 130%, respectively in post-treatment time-averaged WSS and OSI values averaged over the aneurysm sacs obtained from explicit and porous medium models of coiled aneurysms Aneurysm-averaged WSS Differences of 10-25% between aneurysmal post-treatment haemodynamics predicted by explicit and porous medium models of the deployed stents. Relative root mean square errors of 21-24% in mean WSS magnitude averaged over the entire sac and 45-81% in mean WSS magnitude averaged over the aneurysm dome between simulations with flow diverters modelled either as porous medium or explicitly.
Intra-procedural systemic flow alterations	Mut *et al.* [191]	Intra-procedural parent vessel flow rate alterations greater than 30% can result can result in a 30-80% change in the aneurysmal haemodynamic variables.

c) Uncertainties that have so far not been studied in intracranial aneurysm simulations
Source of uncertainty
Intra-procedural alterations in parent vessel geometry
Blood coagulation model structure (missing reactions etc.)
Parameters of mechanistic models of medical devices (coils and stents)
Variabilities in blood composition and coagulation kinetic reaction rates in normal or pathological conditions

Chapter 3

Uncertainty quantification of wall shear stress in intracranial aneurysms using a data-driven statistical model of systemic blood flow variability

Abstract — Adverse wall shear stress (WSS) patterns are known to play a key role in the localisation, formation, and progression of intracranial aneurysms (IAs). Complex region-specific and time-varying aneurysmal WSS patterns depend both on vascular morphology as well as on variable systemic flow conditions. Computational fluid dynamics (CFD) has been proposed for characterising WSS patterns in IAs; however, CFD simulations often rely on deterministic boundary conditions that are not representative of the actual variations in blood flow. I develop a data-driven statistical model of internal carotid artery (ICA) flow, which is used to generate a virtual population of waveforms used as inlet boundary conditions in CFD simulations. This allows the statistics of the resulting aneurysmal WSS distributions to be computed. It is observed that ICA waveform variations have limited influence on the TAWSS on the IA surface. In contrast, in regions where the flow is locally highly multidirectional, WSS directionality and harmonic content are strongly affected by the ICA flow waveform. As a consequence, I argue that the effect of blood flow variability should be explicitly considered in CFD-based IA rupture assessment to prevent confounding the conclusions.

3.1   Introduction

Pro-inflammatory responses in the vascular endothelium play a key role in intracranial aneurysm (IAs) growth and rupture [38]. The driving factor behind this response is hypothesised to be wall shear stress (WSS), defined as the frictional force of blood on the vessel wall. Localised adverse WSS patterns, i.e., spatiotemporal distribution of hemodynamic WSS on the aneurysm sac, have been shown by Feaver *et al.* [135] to correlate with the expression of transcription factors related to inflammation (such as NF-κB), and have been shown by Davies *et al.* [231], Chiu *et al.* [232] and, Mohamied *et al.* [125] to correlate with locations of atherosclerotic lesions on the vessel wall. Several attempts have been made to further characterise the atherogenic WSS patterns by looking into, e.g., WSS magnitude oscillations [233, 234], temporal and spatial gradients [235, 236], and the harmonic content of the WSS waveforms [135, 237].

Evaluation of WSS from phase contrast magnetic resonance imaging is not reliable enough to provide quantitative measures [238]. Therefore, computational fluid dynamics (CFD) has been proposed as a tool for characterising WSS patterns.

WSS multidirectionality has been recently used to characterise atherogenic flows in CFD simulation studies by Mohamied *et al.* [125], and Peiffer *et al.* [239]. However, CFD-based studies are controversial among interventional neuroradiologists and have not become widely accepted in clinical decision making. Such controversies can be found in e.g. Kallmes *et al.* [46], Cebral *et al.* [225], Valen-Sendstad *et al.* [134], and Xiang *et al.* [240], where the clinicians and CFD modellers discussed the confounding nature and unreliability of various CFD-based haemodynamic variables and the importance of assumptions and uncertainties associated to CFD models. Failure to address underlying variations in systemic blood flow due to the state of the patient (e.g., level of stress, physical activity, sleep, etc.) and its effect on WSS patterns may be one of the reasons behind this perceived unreliability.

Here, the primary aim is to quantify the effect of flow waveform variability on the hemodynamic WSS over the intracranial aneurysm surface. Boundary conditions in CFD models are typically either drawn from literature data or obtained by patient-specific flow imaging over a few heartbeats. Neither approach reproduces the *intra-subject variability* of systemic blood flow arising due to the presence of dynamic regulatory systems.

The sensitivity of the intra-aneurysmal haemodynamics to the systemic flow conditions has been explored in various studies. For example, Geers *et al.* [108] found a 20% increase in flow rate to correspond to a 27% increase in aneurysmal WSS; Xiang *et al.* [109] found different flow rate waveforms with the same time-averaged inflow rate to

produce almost identical WSS distributions and WSS magnitudes, similar oscillatory shear index (OSI) distributions, but drastically different OSI values; and Morales *et al.* [111] observed that the spatiotemporal-averaged aneurysmal WSS varies quadratically with the inflow rate. However, CFD models of vascular blood flow still mostly report deterministic flow results.

To address this problem, I construct a Gaussian process model (GPM) for generating internal carotid artery (ICA) waveforms. The GPM is calibrated against the data from Ford *et al.* [74] on ICA flow measurements across a cohort of 17 young adults. The variability due to flow uncertainty is measured in three quantities of interest: time-averaged WSS (TAWSS), OSI, and transverse wall shear stress (transverse wall shear stress (TransWSS)), and means and confidence intervals are computed for each.

In this way, we achieve a novel combination of CFD simulations and statistical models that: 1) incorporates physiological flow measurements, 2) is more systematic than previous approaches for quantifying flow uncertainty, and 3) can be fitted to the characteristics of particular cohorts.

Classifying IAs by their rupture likelihood is currently performed by looking at morphological features and patient-specific risk factors [22]. Machine learning has been proposed to aid in this task. Xiang *et al.* [241] used morphological and hemodynamic features assessed on a cohort of 119 patients to train a logistic regression model for IA classification. Bisbal *et al.* [242] performed an exhaustive evaluation of seven different classifiers trained on 60 different features identified as being significant. Using the bounds on WSS uncertainty computed in this study, it is explored what happens when flow uncertainties are incorporated into a classifier similar to that of Xiang *et al.* [241]. The results demonstrate that the effect of flow variability on IA classifiers should be explicitly considered to avoid biasing effects that may confound the conclusions of CFD studies used to predict IA rupture likelihood.

3.2   Materials and Methods

3.2.1   Image-based patient-specific intracranial aneurysm models

Patient-specific surface models for two saccular IAs from the @neurIST cohort were previously reconstructed from three-dimensional rotational angiography as described in by Villa-Uriol *et al.* [243] using the geodesic active regions approach of Bogunovic *et al.* [58]. Both IAs were located on the ophthalmic segment of the left internal carotid artery. During the follow-up period, the aneurysm in patient 1 ruptured, whereas the one in patient 2 did not rupture. Vascular models were discretised using unstructured volumetric meshes in ANSYS ICEM v16.2 (Ansys Inc., Canonsburg, PA, USA). Tetra-

hedral elements with maximum edge size of 0.2 mm were used and three layers of prismatic elements with an edge size of 0.1 mm were used to create boundary layers. The total number of elements were 2.2 and 6.6 million and mesh densities were 3025 and 3315 elements per mm^3 for patients I and II, respectively.

3.2.2   Computational fluid dynamics simulations

Blood flow in the IA was modelled using the incompressible unsteady Navier-Stokes equations. Blood was assumed to be a Newtonian fluid of density 1066 kg/m^3 and viscosity of 0.0035 Pa·s. Peak systolic Reynolds numbers at the inlet ranges from 338 to 532, and no turbulence modelling was performed. To ensure fully-developed flow, the computational domain was extended at the inlet boundary by an entrance length proportional to the inlet boundary maximum Reynolds number. The Navier-Stokes equations were solved in ANSYS CFX v16.2 (Ansys Inc., Canonsburg, PA, USA) using a finite-volume method. Second-order-accurate discrete approximations were used both in space and time, i.e., a second-order advection scheme and a second-order backward Euler transient scheme. The cardiac cycle was discretised in time into 200 equal steps. Element and time-step sizes were set according to the @neurIST processing toolchain where mesh and time-step size independency tests were performed on WSS, pressure, and flow velocity at several points in the computational domain as described by Villa-Uriol *et al.* [243]. Arterial distensibility was not considered in this study (rigid-wall assumption).

3.2.3   Inlet boundary conditions and generation of ICA waveforms

A GPM (see e.g. Ref. [244] for details) was used to generate multiple inflow waveforms that mimicked the inter-subject flow variability at the ICA. The GPM was trained on subject-specific data from the study of Ford *et al.* [74] describing ICA flow measurements in 17 young adults. In that work, descriptive statistics of the reference flow rate waveform were reported in terms of mean values and variances of both time and flow rate at 14 fiducial landmarks. Flow rate mean values and variances were used to generate the GPM in this study. Any GPM is defined by its mean waveform plus a covariance function. Since the ICA flow waveform was smooth, continuous, and differentiable, the covariance function was chosen to be a squared exponential, $\sigma^2(t_j, t_k) = \sigma_0^2 \exp\left(-||t_j - t_k||_T^2 / 2L^2\right)$, with parameters σ_0 and L [244]. The distance metric was chosen as $||t_j - t_k||_T := \min\{|t_j - t_k|, |t_j - t_k + T_{\text{period}}|, |t_j - t_k - T_{\text{period}}|\}$ to get periodic waveforms, where T_{period} was the normalised cardiac cycle length and $t_j, t_k \in [0, T]$. As a stationary Gaussian process could not fully fit the observed data

(variance at systolic peak was greater than during diastole), a symmetric bell-shaped function, f, was used to introduce non-stationarity in the process.

$$f(t_j, t_k) = s_d + \frac{1}{\frac{1}{s_{ps}} + |\frac{max(t_j, t_k) - x_{ps}}{2}|^4} \qquad (3.1)$$

In equation (3.1), $s_d \in [0, 1]$ and $s_{ps} \in [0, 1]$ are parameters controlling the variance during diastole and at peak systole, respectively; and, x_{ps} is the peak systolic landmark number. As reported by Ford *et al.* [74], the ICA waveform systolic variance is approximately four times greater than diastolic variance and the systolic peak is the third landmark on the ICA waveform. Thus, in equation (3.1) the parameter s_{ps} was replaced by $4s_d$ and x_{ps} was set to 3.

Finally, the GPM mean waveform was set to the mean ICA waveform taken from Ford *et al.* [74]; and the GPM covariance function $\sigma^2(t_j, t_k)$ was constructed as

$$\sigma^2(t_j, t_k) = f(t_j, t_k) \cdot \sigma_0^2 \cdot$$
$$\exp\left(-\min\{|t_j - t_k|, |t_j - t_k + T_{\text{period}}|, |t_j - t_k - T_{\text{period}}|\}/2L^2\right). \quad (3.2)$$

Random realisations of the GPM was then used GPM-generated ICA waveforms. To fit the process covariance σ_0^2 and correlation length L to that observed in the measurements, for each $s_d \in [0, 1]$, a two-dimensional numerical optimisation problem was solved based on the cost function, g, that penalised values exactly equal to the mean waveform or greater than twice the standard deviation for each landmark.

$$g(y_j) = \begin{cases} P_o(y_j - (\bar{y}_j + 2SD_j)) & \bar{y}_j + 2SD_j \leq y_j \\ \frac{-P_m}{2SD_j}|y_j - \bar{y}_j| + P_m & \bar{y}_j - 2SD_j \leq y_j \leq \bar{y}_j + 2SD_j \\ P_o(y_j - (\bar{y}_j - 2SD_j)) & y_j \leq \bar{y}_j - 2SD_j \end{cases} \qquad (3.3)$$

For each landmark j, y_j is the value of ICA flow generated by the GPM; and, $\bar{y}_j$ and SD_j are the mean and standard deviation reported by Ford *et al.* [74]. Penalty parameters P_m and P_o penalise y_i values that are exactly equal to the mean or are deviated more than twice the standard deviation from the mean.

A virtual population of 50 internal carotid flow waveforms was then generated and used as inlet boundary conditions to the CFD models. To maintain a physiological arterial WSS of 1.5 Pa and to enable population-wide comparisons, Poiseuille's law was used to scale the GPM-generated waveforms such that the time-averaged WSS was 1.5 Pa at the inlet. Figure 3.1(a) shows the 95% confidence bounds of flow at the

fiducial landmarks (black bars), and a virtual population of internal carotid artery flow
waveforms generated from the Gaussian process model (red curves).
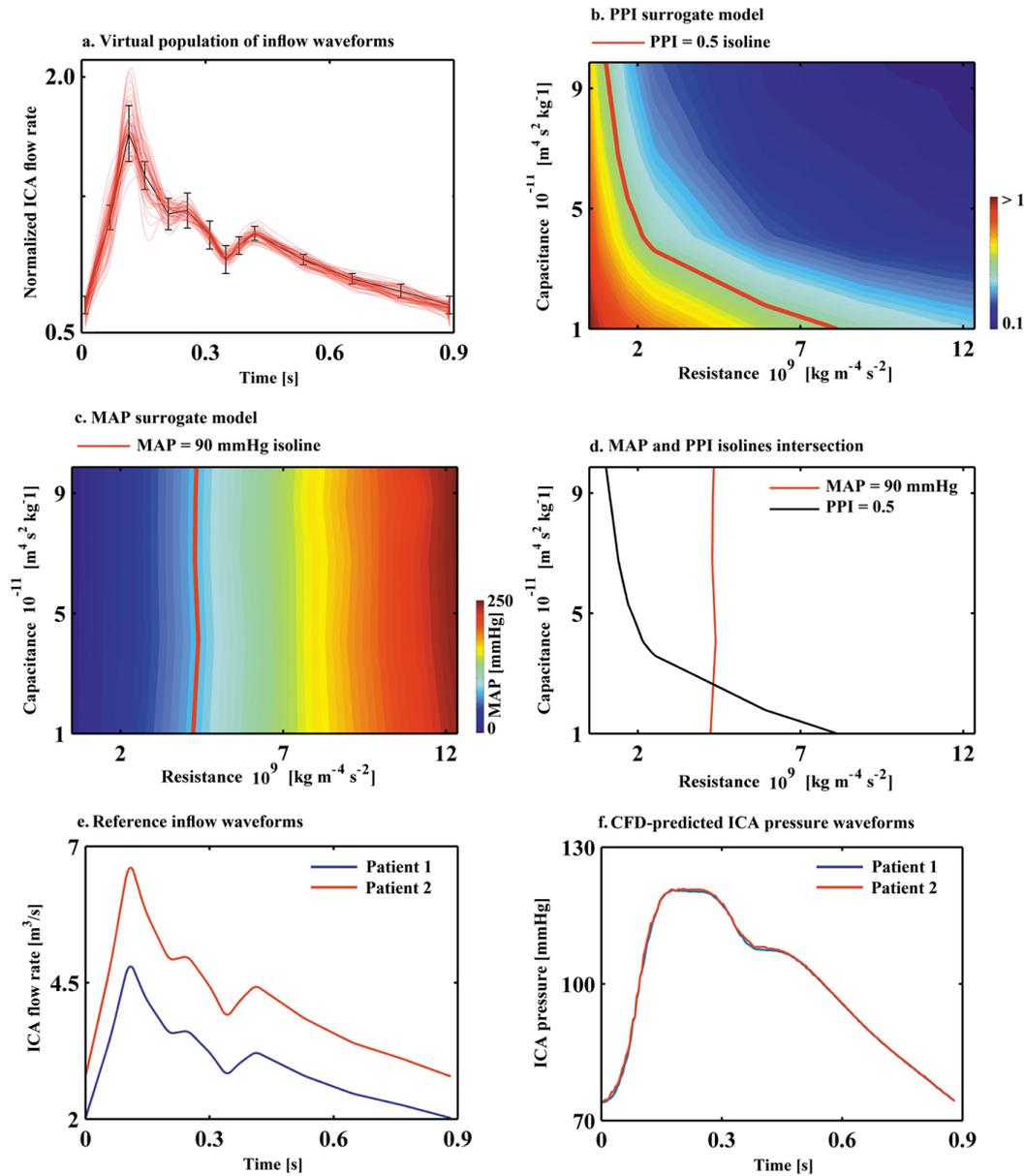
Figure 3.1: a) Response surface of the surrogate model of the ICA MAP. ICA MAP is
90 mmHg on the red solid line. b) Response surface surrogate model of the ICA PPI.
ICA PPI is 0.5 on the red solid line. c) Intersection of the MAP and the PPI isolines
gives the right terminal resistance (R) and capacitance (C) values for the desired MAP
and PPI at the ICA. d) Reference flow rate waveforms for patients 1 and 2 that are
scaled such that the TAWSS at the inlet was 1.5 Pa for each patient. e) CFD-predicted
pressure waveforms at the ICA after choosing the right R and C values.

3.2.4   Outlet boundary conditions

A two-element windkessel (RC) boundary condition model was assigned at the outlet boundaries. The RC windkessel model acts as a low-pass filter with a RC time constant $\tau = R \times C$. To guarantee that the terminal RC circuit converges to the ultimate pulsatile pressure and the solution is independent from the initial transient numerical effects, each simulation was run for certain number of cycles, defined as $nCycle = \left\lceil \frac{\tau}{T_{\text{period}}} \right\rceil + 1$, where $\lceil x \rceil$ symbolized the ceil function. Results from the last cardiac cycle were then used to calculate the hemodynamic parameters of interest. The resistance and capacitance values of the windkessel model were chosen to maintain a physiological range of ICA pressure and pulsatility for each particular patient. To enable rapid parameter tuning, a surrogate model was built using polynomial response surfaces to approximate the MAP and PPI of the flow for each (R,C) pair. A Chebyshev grid of 81 (9×9) points was created on a 2D physiological range of variability for R and C (reported in e.g. Brown *et al.* [82, 83, 245, 246, 247]) in such a way that each point on the grid was associated with a pair of R and C values. A total of 81 CFD simulations were performed while recording the observed values of steady-state MAP and PPI in the ICA for each simulation after *nCycle* heartbeat cycles. To develop a surrogate model of ICA MAP and PPI vs terminal resistance and capacitance, MAP and PPI surfaces were linearly interpolated over a uniform grid of 100×100. The surrogate model was used to select values R and C values in such a way that when the reference inflow waveform were applied at the inlet boundary, the model provides ICA pressures with MAP and PPI matching clinically measured values of 90 mmHg and 0.5 from the normal individual, respectively. Figure 3.1(b) and Figure 3.1(c). show the response surfaces of MAP and PPI against terminal resistance and capacitance for patient 1. Figure 3.1(d), values of R and C at the point, where MAP = 90 mmHg and PPI = 0.5 intersects, were selected as optimized windkessel parameters for patient 1. As mentioned above, a derivation of the Poiseuille's law that relates the inflow rate to the WSS and vessel's inlet cross-sectional area was used to scale the time-averaged flow rate in the parent vessel for each patient. Since the time-averaged flow rates are different in patient 2, the resistance and capacitance values from the first patient's surrogate model need to be scaled using factor α defined as $\alpha = \text{inflow}_{tav,1}/\text{inflow}_{tav,2}$, where where $\text{inflow}_{tav,1}$ and $\text{inflow}_{tav,2}$ are time-averaged inflow rates for patients 1 and 2. The terminal resistance and capacitance were then scaled as $R_2 = (1/\alpha) \times R_1$ and $C_2 = \alpha \times C_1$, respectively.

Figure 3.1(e) shows reference inflow waves for patients 1 and 2. Figure 3.1(f) shows that, applying the windkessel outlet boundary condition with tuned R and C values,

the same desired ICA pressure has been obtained for patients 1 and 2 with different inflow waveforms. Since the time-averaged inflow rate was kept constant and only waveform shapes varied across the virtual population, the same R and C values as those tuned with the reference inflow waveforms were used for all 50 CFD simulations on each patient.

3.2.5 Data analysis

WSS, $\boldsymbol{\tau}_w(x,t)$, is a time-varying vector field that represents the tangential component of the traction vector on the wall. The magnitude, pulsatility, directionality and the harmonic content of the WSS waveforms on the aneurysm wall were assessed using several derived quantities of interest.

WSS magnitude

TAWSS was calculated by averaging the magnitude of WSS vector at each surface node over the cardiac cycle.

$$\text{TAWSS}(x) = \frac{1}{T_{\text{period}}} \int_{T_0}^{T_0 + T_{\text{period}}} |\boldsymbol{\tau}_w(x,t)| \, dt \tag{3.4}$$

The variables T_0 and $T_0 + T_{\text{period}}$ are the starting point (3rd heartbeat) and the length of the cardiac cycle over which the WSS was integrated, respectively.

WSS directionality

As suggested by Mohamied *et al.* [125] and Peiffer *et al.* [239, 248], to assess the directionality of WSS I used both OSI and transverse WSS. The oscillatory shear index was calculated as

$$\text{OSI} = \frac{1}{2} \left(1 - \frac{|\int_{T_0}^{T_0 + T_{\text{period}}} \boldsymbol{\tau}_w(x,t) \, dt|}{\int_0^{T_{\text{period}}} |\boldsymbol{\tau}_w(x,t)| \, dt} \right) \tag{3.5}$$

and transverse WSS was calculated as defined by Peiffer *et al.* [239]

$$\text{transWSS} = \frac{1}{T_{\text{period}}} \int_{T_0}^{T_0 + T_{\text{period}}} |\boldsymbol{\tau}_w(x,t) \cdot \hat{q}| \, dt, \tag{3.6}$$

where $\hat{q} = \hat{p} \times \hat{n}$ and the unit vector $\hat{p}$ is the direction of the time-averaged WSS vector, $\hat{n}$ is the surface normal, and consequently the unit vector $\hat{q}$ is located in the same plane as $\hat{p}$ an its direction is perpendicular to the time-averaged WSS vector.

The unit vector $\hat{p}$ was calculated as

$$\hat{p} = \frac{\int_{T_0}^{T_0+T_{\mathrm{period}}} \boldsymbol{\tau}_w(x,t)\,dt}{|\int_{T_0}^{T_0+T_{\mathrm{period}}} \boldsymbol{\tau}_w(x,t)\,dt|} \tag{3.7}$$

As long as a preferred time-averaged direction of flow exists, TransWSS ranges from 0 to TAWSS. As the TAWSS takes substantially different values at aneurysmal regions with disturbed or regular flow, I defined the rTransWSS as the TransWSS normalised by the TAWSS at each surface point.

WSS harmonics

As indicated by Lee *et al.* [233], despite the multidirectional nature of blood flow in patient-specific vascular models, most experimental studies are performed under uniaxial flow due to constraints in experimental flow setups. Recently, WSS projections onto a reference axial direction were performed to rectify multidirectional flows and make them comparable to the flows used for *in vitro* experiments of Arzani *et al.* [249] and Morbiducci *et al.* [250]. However, since rectifying the WSS signal combines the magnitude and directionality aspects of the WSS vector and influences its harmonic content, I chose to perform a harmonic analysis on both the original and the rectified WSS signals. It has been observed that most physiological waveforms can be accurately reconstructed by the first ten or fewer harmonics [77]. Studying the first eight harmonics of the WSS signals at the ICA, Feaver *et al.* [135] showed that the endothelial inflammatory responses are mainly regulated by the first harmonic of the WSS signal. Thus, in this study, I based the harmonic analyses on the first eight harmonics of the WSS signals. I calculated the axial WSS as the component of time-varying WSS vector projected onto the unit vector $\hat{p}$. The fast Fourier transform was used to describe the time-varying aneurysmal WSS and axial WSS waveforms in the frequency domain and extract the amplitudes of the harmonics zeroth to eighth. It has been hypothesised that dominance of frequencies higher than the heart rate in the WSS magnitude signal triggers inflammatory responses in the vascular endothelium [135, 202]. The DH is another quantity of interest defined as the harmonic with the greatest amplitude by Himburg *et al.* [237]. As shown by Lee *et al.* [233], DH is independent from other WSS-related variables. In this study I also used DH to investigate how waveform variability in the parent vessel affect the dominant frequency of the time-varying WSS magnitude over the aneurysm sac.

Intracranial aneurysm rupture prediction

To evelute the effect of WSS uncertainty in IA rupture prediction, a different subset of 38 IAs all located at the sylvian bifurcation of the middle cerebral artery (MbifA-type) were selected from the @neurIST cohort and processed through the CFD pipeline as described in the Methods section. For this cohort, outlet branches were automatically clipped 20 mm after their proximal bifurcation. Branches shorter than 20 mm were extruded before truncation. Zero-pressure boundary conditions were then imposed at all outlets. As a full CFD simulation of all 50×38 cases would have been prohibitively costly, three representative waveforms were instead used for each of the 38 cases: mean flow, minimum flow and maximum flow predicted by the GPM model. TAWSS, OSI, and TransWSS were post-processed for each of these simulations and spatially averaged over the aneurysm sac to arrive at the feature values used for classification. These three different flow waveforms were then used to train a logistic regression model classifier similar to that of Xiang $et\ al.$ [241]:

$$\mathrm{logit}(P_r) = \beta_0 + \beta_1 \mathrm{OSI} + \beta_2 \mathrm{TAWSS},$$

where P_r is the model-predicted probability of the ruptured type, and the logit function is defined as $\mathrm{logit}(p) = \log\left(\frac{p}{1-p}\right)$. The regression coefficients $\beta_0, \beta_1, \beta_2$ were obtained through standard generalised regression techniques, and were used to define the corresponding odds ratios ($\mathrm{OR_{OSI}} = \exp(\beta_1)$ etc.), signifying how the odds of rupture increase by each unit increase in OSI.

3.3   Results

Figure 3.2 shows the mean values and the coefficient of variance (CoV) for haemodynamic variables TAWSS, OSI, and rTransWSS on the aneurysm sac simulated by CFD over the population of 50 difference ICA waveforms. In both cases, the ICA waveform variability had limited effects (CoV < 0.05) on the TAWSS. However, the effects were remarkable on WSS directional variability. CoVs for aneurysmal OSI and rTransWSS were both greater than 0.4 at regions where the WSS vectors had low magnitude but were directionally varying in time (disturbed flow regions). Waveform variability in the parent vessel had less significant effects on the WSS directionality at regions where shear stresses are higher and remain mostly unidirectional throughout the cardiac cycle (stable flow regions).
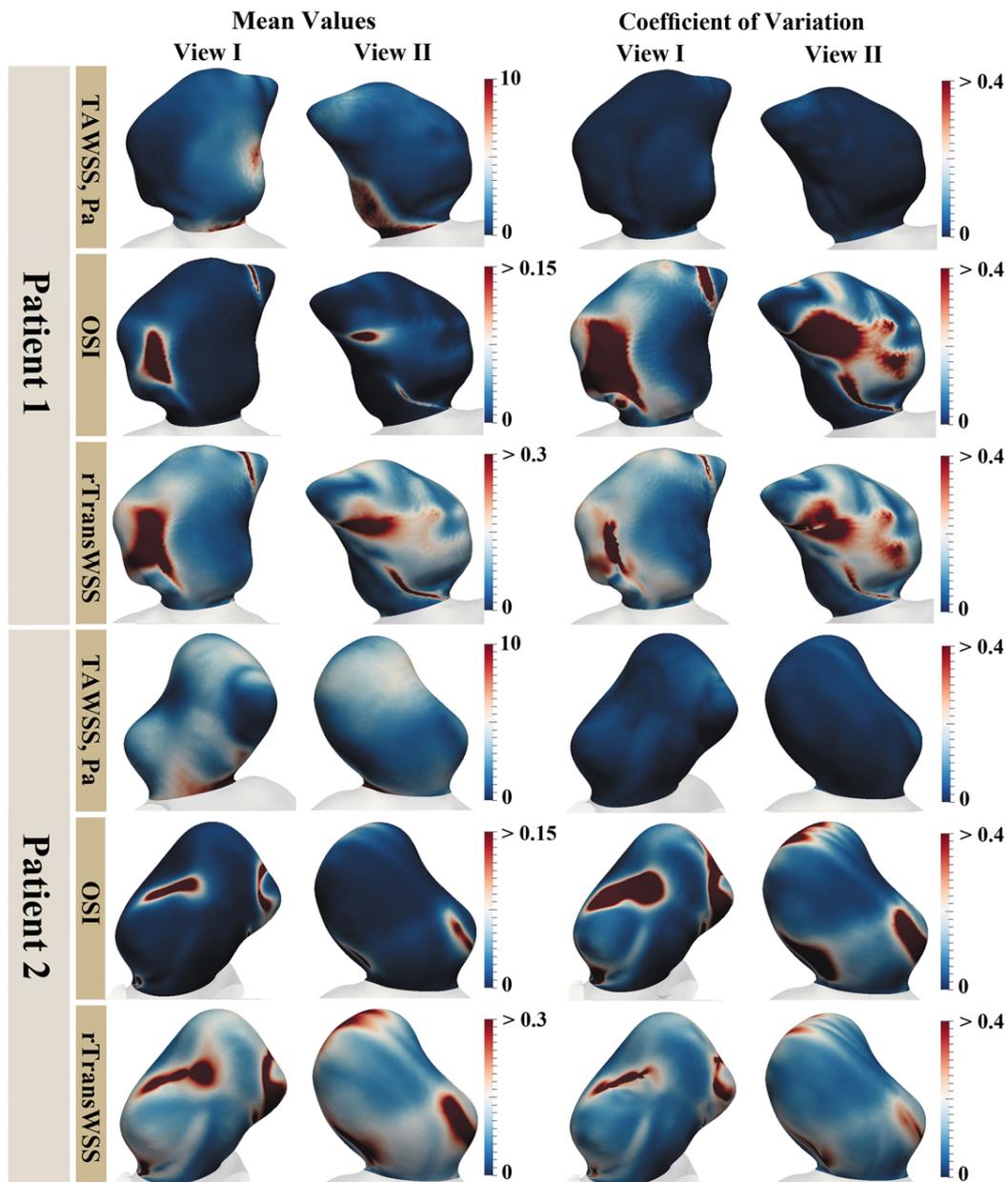
Figure 3.2: The mean values and the coefficients of variation (CoV) of the TAWSS, the OSI, and the rTransWSS across the virtual population over the aneurysm walls for patients 1 and 2.

Figure 3.3 shows mean values and CoVs for the dominant harmonic (DH) over the aneurysm sac. On both aneurysms, there are regions where the dominant frequencies are up to 5 times greater than the fundamental frequency (the heart rate). Results show that ICA waveform variability highly influences the time-varying WSS signal at regions where the higher harmonics dominate (CoV > 2). Similar to the directionality, less significant effects were observed at regions with regular pulsatile flow dominated

by the heart rate frequency (regions where DH is unity).

However, DH was originally defined for a unidirectional axial flow and may not lead to clinically interpretable results in multidirectional nonaxial flow [233, 250]. To alleviate this issue in the complex aneurysmal flows, I followed the method presented by Lee *et al.* [233] and rectified WSS vectors by projecting them on the time-averaged WSS direction as a reference axial direction. Figure 3.3 also shows the effect of parent vessel waveform variability on the harmonic content of the axial WSS magnitude signal. Results show that rectification of the WSS signal increased the DH at regions where flow is multidirectional. This can be attributed to the previously mentioned effects of ICA waveform variations on the WSS directionality, which implicitly affected the WSS magnitude signal during the rectification process. It can be seen that ICA waveform variability significantly influences the harmonic content of the axial WSS at disturbed flow regions (CoV > 2). To provide more intuition into the effects of parent vessel flow waveform variability, I illustrated the results for five manually selected representative points on the aneurysm sacs.

3.3.1 Effect of flow uncertainty on rupture pattern

The three WSS-derived quantities were evaluated through CFD simulations in $N = 38$ cases taken from the @neurIST database. Summary statistics of the WSS values evaluated are shown in Table 3.1 for the case of mean flow. An unpaired two-sided two-sample t-test was used to select the WSS-related features that were significantly different in the ruptured vs. unruptured populations. Spatially averaged OSI was significant or almost significant for all three flow cases ($p \in [0.032, 0.058]$), whereas TAWSS and TransWSS were not significant for any of the three flow cases considered ($p = 0.7$ for TAWSS and $p \in [0.12, 0.15]$ for TransWSS). This was in agreement with the analysis of Bisbal *et al.* [242] (who used a superset of the data used in this study), but contradicted the observations of Xiang *et al.* [109] who obtained significance also for TAWSS. It was therefore opted to train the classifier only on one feature, the OSI, leading to the regression model $\text{logit}(P_r) = \beta_0 + \beta_1 \text{OSI}$ for the rupture classification variable P_r. Before training the classifier, the OSI values were scaled so that the maximum value across the 38 cases was equal to 10. The data were divided into 19 training cases, which were used to estimate the regression coefficients, and 19 test cases, which were used for cross-validation.

	Ruptured ($N = 14$)	Unruptured ($N = 24$)	p-value
TAWSS [Pa]	3.32 (3.36)	3.76 (3.25)	0.7
OSI	12.4×10^{-3} (7.25×10^{-3})	7.79×10^{-3} (6.05×10^{-3})	0.032*
rTransWSS	0.104 (0.037)	0.088 (0.029)	0.12

Table 3.1: WSS quantities derived from CFD-simulations in the ruptured vs. unruptured groups of the @neurIST cohort. Values are group-wise means and standard deviations of the mean flow case. Statistical significance in univariate analysis computed using a two-sided t-test.
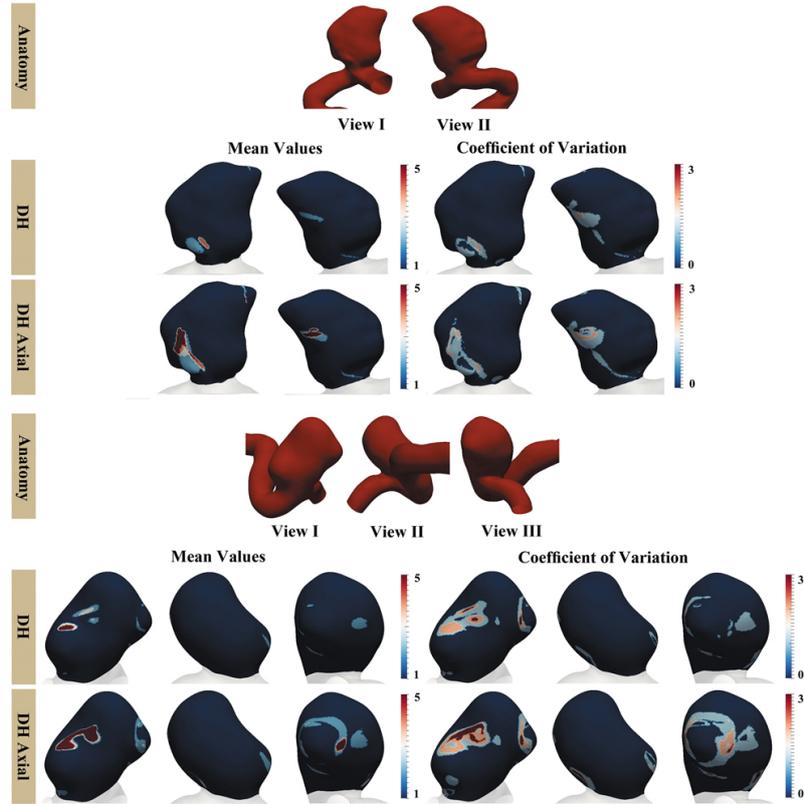
Figure 3.3: The mean values and the coefficients of variation (CoV) of the DH and axial DH across the virtual population over the aneurysm walls for patients 1 and 2.

The logistic regression based classifier achieved an area under the ROC curve that ranged in AUC $\in [0.8947, 0.9044]$. For the cutoff value $P_r = 0.9$, the resulting classifier achieved a sensitivity ranging in SENS $\in [79.0\%, 84.2\%]$, and a specificity ranging in SPEC $\in [79.0\%, 89.5\%]$ in the cross-validation exercise. The regression coefficients identified in each three flow cases were in the range $\beta_0 \in [-3.59, -2.93]$ and $\beta_1 \in [0.804, 0.883]$. The corresponding odds ratio for OSI was in the range OR$_{\mathrm{OSI}} \in [2.23, 2.42]$, reproducing the known correlation between elevated OSI and rupture status. While the accuracy of the classifier was only moderately affected by

the flow case considered, the final rupture/no-rupture prediction changed as a function of flow for 4 cases out of 19.

3.4 Discussion

Recent evidence links the region-specific inflammatory phenotype of the endothelial cells to both directionality and harmonic content of the time-varying WSS vector field [125, 126, 135, 202, 239]. Spatiotemporal variations of vascular WSS are driven by variabilities in the blood flow waveform and the vascular morphology. Although attempts at measuring the effect of parent vessel flow waveforms on WSS-related quantities of interest measuring directionality and harmonic content have been made by Peiffer *et al.* [135, 202, 233, 239] and others, there are few studies that have systematically evaluated the sensitivity of WSS to flow variability.

Time-averaged inflow rates have been shown to affect the magnitude of aneurysmal WSS[108]. Using one-shot measurements of patient-specific inflow boundary conditions has been shown to highly influence the magnitude of aneurysmal WSS when compared to results obtained from simulations with typical inflow boundary conditions derived from literature [104, 105, 106]. However, *in vivo* flow measurements typically record systemic flow only for a few cardiac cycles, and therefore do not represent the full range of flow variability. In the recent study of Xiang *et al.* [109], the effect of four different inlet waveforms on the space-averaged OSI was tested using CFD. Different waveforms produced drastically different absolute values of OSI, but similar OSI distributions over the aneurysm sac. A linear relationship was also observed between the spatially averaged OSI values calculated using different inflow waveforms, which suggests that changing the waveform did not consistently change the rupture risk ranking of aneurysms. Absolute values of OSI might, however, not be a robust criteria for clinical decision making unless the flow-related uncertainty is explicitly taken into account.

I evaluated the flow-induced WSS variability by performing simulations using boundary conditions sampled from a statistical description of inter-subject flow variability. When keeping the time-averaged flow rate fixed, variations in ICA flow waveforms had limited effects on the TAWSS over the aneurysm sac. However, it was found that WSS directionality measures (OSI and rTransWSS) in the disturbed flow regions (atheroprone regions) were very sensitive to flow waveform variability, although the effects were limited in regular flow regions where a preferred direction of flow exists (atheroprotective regions). To shed more light on regional effects of flow waveforms on the aneurysmal WSS, I defined atheroprone regions as regions where WSS is low (TAWSS < 1 Pa) and multidirectional (rTransWSS > 0.3) and atheroprotective re-

gions as regions where TAWSS > 3 Pa and almost unidirectional (rTransWSS < 0.1). These thresholds were conservatively chosen according to studies where WSS magnitude and directionality were correlated with pro-inflammatory endothelial phenotypes [125, 126, 135, 239]. As shown in Figure 3.4 for the two IAs considered, varying inflow waveform had limited effects on the TAWSS in both disturbed flow and regular flow regions (CoV < 0.1). However, WSS directionality in disturbed flow regions is strongly affected by the inflow waveform (CoV up to 2 with a median at 0.25), when compared to the protective regions. This implies the importance of flow waveform uncertainty in aneurysmal regions which are prone to inflammatory phenotypes and potential rupture. Mohamied *et al.* [125] observed that despite OSI, TransWSS correlated significantly with atherosclerotic lesions in rabits' aorta. Comparing OSI and rTransWSS as measures of WSS directionality, I observed that these two variables are in stronger correlation at regular flow (atheroprotective) regions (Pearson $r = 0.94$ and 0.96 for aneurysms 1 and 2, respectively; $p < 10^{-5}$) when compared to disturbed flow (atheroprone) regions where flow is highly multidirectional (Pearson $r = 0.75$ and 0.66 for aneurysms 1 and 2, respectively; $p < 10^{-5}$).

I have studied variability of the DH of the local WSS signal and observed that, due to nonlinear effects due of the vascular morphology, there are regions where the dominant harmonic of the time-varying WSS signal is not the systemic fundamental frequency (heart rate). I observed that, when considering the DH of the axial WSS signals, regions with higher DH than the heart rate co-localise with the regions where flow is multidirectional. This co-localisation could be explained by the fact that axial WSS is the projection of the instantaneous WSS vector in the time-averaged WSS vector direction. Xiang *et al.* [109] observed a strong correlation between the space-averaged aneurysmal OSI and the inflow waveform pulsatility index (PI), and suggested that OSI might be mainly determined by the PI of the inlet waveform. As a subsidiary study, I investigated any possible correlation between the inflow PI and the local OSI at five points on the aneurysm sacs. At each point on the aneurysm sac, PI was calculated as the difference between maximum and minimum flow rate divided by the time-averaged flow rate during each cardiac cycle. No clear correlation was observed between inflow PI and OSI at points where the dominant frequency was higher than the heart rate.This implies that parent vessel PI (easy to measure) is not a good surrogate for evaluating aneurysmal OSI (difficult to measure).
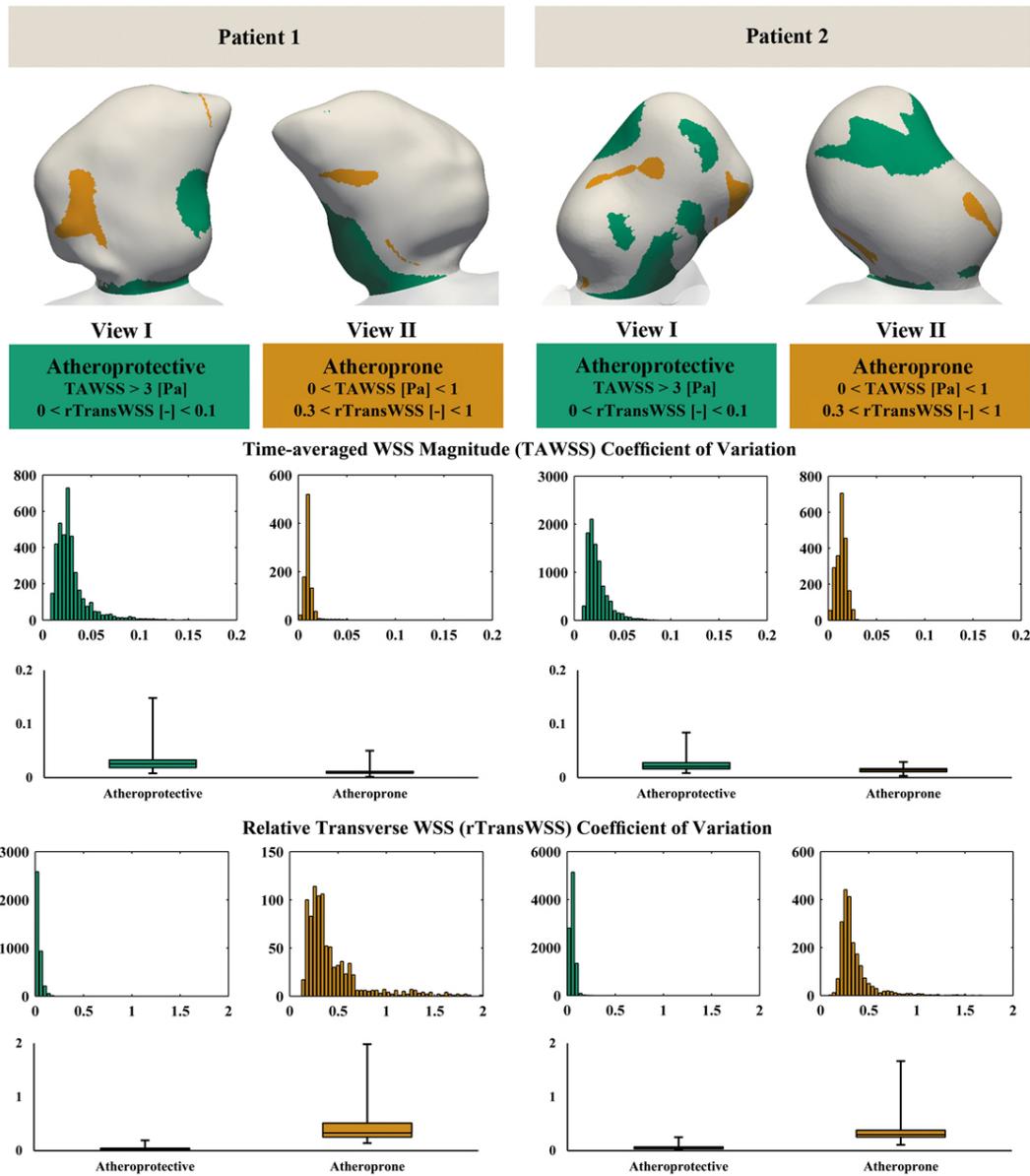
Figure 3.4: Regional variations of the time-averaged WSS magnitude and the relative transverse WSS. Histograms shows the distribution of the coefficient of variations on each of the atheroprone and atheroprotective regions. A boxplot complementary illustration is also presented under each histogram.

The effects that WSS uncertainty may have on IA rupture likelihood have been explored by using a logistic regression. In the dataset I used, the TAWSS did not reach statistical significance in separating ruptured cases from non-ruptured cases, so that a classifier was built solely based on OSI values. The classifier reached similar accuracy to that previously reported (sensitivity ranging in SENS $\in [79.0\%, 84.2\%]$ and specificity ranging in SPEC $\in [79.0\%, 89.5\%]$), but provided a range of values depending on the

choice of input flow waveform used. While the accuracy of the classifier was similar across waveforms, the classification between likely to rupture/likely to not rupture changed in 4 out of the 19 cases when the flow solution was varied. It is my view that, due to such effects, flow-related uncertainty should be explicitly accounted for in WSS-based rupture predictions to improve their credibility.

The limitations of this study were that the blood flow was assumed to be Newtonian and arterial distensibility was not taken into account, which overestimates WSS by up to 15% Section [251]. Transition from laminar to turbulent occurs at Re = 300-500 in intracranial aneurysms [252], and using laminar flow models may not capture all aneurysmal flow characteristics accurately. Parabolic velocity profiles imposed at the inlet boundaries may lead to different flow characteristics compared to the Womersley profiles. Intra-aneurysmal hemodynamics has been shown to be sensitive to the choice of inlet location for truncating the ICA from the surrounding vascular bed [114]. To reduce such errors and allow realistic flow inside the aneurysms, all the inlets were truncated at consistent locations below the cavernous segment to include the largest possible arterial segment upstream the aneurysm [112]. Vascular models were extruded at inlet boundaries by an entry length proportional to the specific Re to allow for fully developed flow. The flow variability model considered also modelled inter-subject variability only (rather than intra-subject), and was based on data from young adults only.

Chapter 4

A computational model for prediction of clot platelet content in flow-diverted intracranial aneurysms

Abstract — Treatment of intracranial aneurysms with flow-diverting stents is a safe and minimally invasive technique. The goal is a stable embolisation that facilitates stent endothelialisation, and elimination of the aneurysm. However, it is not fully understood why some aneurysms fail to develop a stable clot even with sufficient levels of flow reduction. Computational prediction of thrombus formation dynamics can help predict the post-operative response in such challenging cases. In this work, I propose a new model of thrombus formation and platelet dynamics inside intracranial aneurysms. The novel contribution of this work is the combination of platelet activation and transport with fibrin generation, that is key to characterising stable and unstable thrombus. The model is based on two types of thrombus inside aneurysms: red thrombus (fibrin- and erythrocyte-rich) can be found in unstable clots, while white thrombus (fibrin- and platelet-rich) can be found in stable clots. The thrombus generation model is coupled to a computational fluid dynamics (CFD) model and the FiPi is defined as a quantitative measure of clot stability. The model is validated against an in-vitro phantom study of two flow-diverting stents with different sizing. I demonstrate that the model accurately predicts the lower thrombus stability in the oversized stent scenario. This opens possibilities for using computational simulations to improve endovascular treatment planning and reduce adverse events, such as delayed haemorrhage of flow-diverted aneurysms.

4.1 Introduction

Treatment of large and wide-necked intracranial aneurysms of the anterior circulation with flow-diverting stents has proven to be safe and effective [10, 19, 253]. However, post-treatment rupture after seemingly successful treatment, reported in almost 2% of cases [10, 254], is associated with high risks of mortality and morbidity. Two types of thrombi have been identified from autopsy studies of aneurysms. White thrombus, rich in fibrin and platelets [19, 255], and red thrombus. Red thrombus is characterised by: (i) less enmeshed platelets [19, 255], (ii) not being able to facilitate the formation of a neointimal layer [256, 257], (iii) being prone to continuous fibrinolysis and renewal [255, 258, 259], and (iv) inducing autolytic activities in the wall resulting in weakening of the wall and ultimately rupture [19, 255, 260]. The presence of non-organised red thrombi after flow diversion has been suggested as a potential predictor for post-treatment rupture [19, 254, 255, 260, 261, 262]. There is a growing consensus that assessment of thrombus composition is required to successfully predict flow diverter performance [19, 254, 255, 260, 261, 262, 263].

Mechanisms of flow diverter (FD) -induced initiation and propagation of thrombosis are not well understood. In flow stasis, secretion of tissue factor by endothelium [264], white blood cells [264], and hypoxic platelets [264, 265]; as well as, secretion of platelet activating factors by the endothelium [266] and hypoxic red blood cells [264, 267, 268] are associated with fibrin generation and platelet activation, the two major components of clot formation. Regions with low shear flow and high residence time promote platelet activation and adhesion [42, 266], and stabilisation of platelet aggregates [269]. They also enhance platelet-fibrin and platelet-endothelium interactions [42]. However, despite a diverse set of initiation mechanisms, flow stasis can be considered as the nexus between all of them. It was, therefore, chosen to focus on flow stasis as the pathway to thrombus formation.

While extensive computational investigations focusing on thrombosis in flow systems, few studies have simulated coupled haemodynamics and biochemistry in flow-diverted aneurysms [270, 271]. Taking thrombin concentration as a surrogate for thrombosis, Ngoepe *et al.* [270] simulated clot growth in aneurysms after flow diversion, and an assumption was made that thrombin generation originated on the endothelial wall due to tissue damage. In contrast, Ou *et al.* [271] focused on stasis-induced expression on blood-borne tissue factor as the initiator and simulated fibrin generation inside the flow-diverted aneurysm. Although these studies presented promising results on simulation-based prediction of FD-induced thrombosis, they did not attempt to predict the platelet composition of the clot or its stability.

The objective of this study is to create a coupled flow and thrombosis model that is capable of predicting the stability of the clot that forms after flow diversion. To this end, a computational thrombosis model must consider estimation of the clot extent and stability in terms of composition of its structural components, i.e. fibrin and platelets. I consider FD-induced stasis as a surrogate for all the above mentioned thrombosis initiation mechanisms and simultaneously model thrombin and fibrin generation, and platelet activation and aggregation in stagnation regions. I validate the model against an in-vitro experiment performed in [1], in which thrombus formation was examined in an aneurysm phantom treated with FDs of different sizes.

4.2   Materials and Methods

4.2.1   Mechanisms of thrombosis after flow diversion

Increased flow residence time, decreased flow velocity, decreased shear rate, and decreased vorticity have been used to characterise flow stasis in aneurysms [272, 273, 274]. When compared with thrombosed regions, velocity, vorticity, and shear rate were reported to be 2.8 times larger in non-thrombosed regions of elastase-induced aneurysms in animal models [272]. Based on a harmonic analysis of shear rate waves in ten aneurysms, de Sousa *et al.* [266] determined 25 s^{-1} as the time-averaged shear rate below which thrombosis happened. Rayz *et al.* [274] showed that thrombus deposits in aneurysmal regions with a residence time greater than 18.22 ± 11 s. I therefore assumed thrombosis to initiate and progress in *prothrombotic* regions of the aneurysm after flow diversion, i.e., regions with time-averaged shear rate smaller than $SR_t = 25$ s^{-1} [266] and residence time greater than $RT_t = 5$ s [274].

In the present work, I considered four biochemically-coupled events that result in a clot of fibrin mesh and aggregated platelets: (i) *Thrombin generation* occurs by conversion of prothrombin to thrombin on the surface of both resting and activated platelets, but the kinetics of the reaction are faster for activated platelets. Also considered in the model is thrombin inhibition by its primary plasma inhibitor (anti-thrombin), in the absence of heparin catalysis. (ii) *Fibrin generation* occurs in the presence of thrombin, which converts fibrinogen to fibrin monomers. Further polymerisation of the fibrin monomers was not considered. (iii) *Platelet activation* occurs when resting platelets became activated by exposure to thrombin or other activated platelets. The latter mechanism was used as a surrogate for activation by agonists released from other activated platelets [275]. (iv) *Platelet aggregation* in the presence of fibrin takes place when platelets attached to the fibrin network and aggregated to form bound platelets. Bound platelets were assumed to be able to activate prothrombin and other resting platelets.
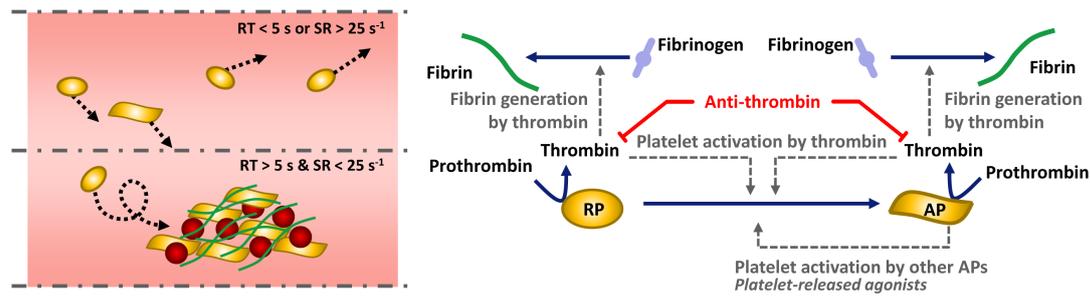
Figure 4.1: Left panel: schematic representation of platelet transport to the clotting site. Right panel: schematic representation of the clotting reaction network modelled in this study.

All in all, the model in this work included five biochemical species: prothrombin (PT), thrombin (TH), anti-thrombin (AT), fibrinogen (FG), fibrin (FI). Three categories of platelets; resting platelets (RP), activated platelets (AP), and fibrin bound aggregated platelets (BP) were considered. A schematic representation of the biochemical species and reactions is given in Figure 4.1. Details of the chemical reactions are described in the next sections.

4.2.2   Governing equations

To assess the likelihood of formation of a fibrin and platelet rich clot, a macroscopic model for post- FD thrombosis in aneurysm was made based on the previous models of haemostatic thrombosis [275, 276] and platelet deposition [277, 278]. In previous models, presence of an injury activated a set of procoagulant factors and finally resulted in thrombin generation and platelet activation. However, the mechanisms of stasis-induced thrombosis after aneurysm flow diversion are far from crystal clear. Yet, different models for thrombus formation and depostion have been proposed in the literature (e.g., in [266, 274]). The model is based on bulk initiation and propagation of thrombosis in regions of flow stasis as a surrogate to several intermediate mechanisms that are not still clear. I based the mathematical description of thrombin generation and platelet activation on the model presented by Sorensen *et al.* [278]. Since this model does not include fibrin generation, I used the mathematical model of fibrin generation presented by Anand *et al.* [276]. To model the bulk aggregation of platelets, I modified a representation of platelet aggregation at the site of injury that was originally proposed by Leiderman and Fogelson [277], called the LF model. Finally, to couple the growing clot to the velocity field, similar to the LF model, a Darcy term was added to the equations of blood motion.

Following the common practice in biochemical reaction modelling, where the rate

of occurrence of event, x, requires an appropriate concentration of a particular species, C_i, i.e., the concept of cooperativity, the Hill function, a sigmoidal activation function of form $\phi_x^i = C_i^n/(C_i^n + C_{i,50}^n)$, was used [279]. In this equation, C_i is the concentration of species i, $C_{i,50}$ is the concentration of species i where the half-maximal activation (half saturation) occurs, and the exponent n, called the Hill coefficient, reflects the steepness and switch-like character of the sigmoid. In this study, I set $n = 4$ where a narrow switch-like response to availability of a specie was needed, and set $n = 2$ when a wider and smoother response was required.

Fluid flow

Three dimensional momentum equations for incompressible and Newtonian fluid, the Navier-Stokes equations, were used to describe blood flow.

$$\rho\frac{\partial \boldsymbol{u}}{\partial t} + \rho(\boldsymbol{u} \cdot \nabla)\boldsymbol{u} = -\nabla p + \mu\nabla^2\boldsymbol{u} - \mu\Phi(k_f, k_p)\boldsymbol{u}. \tag{4.1}$$

In (4.1), $\boldsymbol{u}$ and p represent the velocity vector and pressure, respectively. Blood was assumed to be a Newtonian fluid with constant density, $\rho = 1060$ kg/m^3 and viscosity, $\mu = 0.004$ Pa.s. To account for the effect of clot on the fluid velocity field, without modelling the fluid-structure interaction, the blood clot was treated as a porous medium with both fibrous (fibrin strands) and granular (bound platelets) components. A Darcy term, $\mu\Phi(C_f, C_p)\boldsymbol{u}$, was added to the momentum equations. The function $\Phi(C_f, C_p)$ was defined as

$$\Phi(C_f, C_p) = \frac{1}{k_{fi}}\phi_p^{fi} + \frac{1}{k_{bp}}\phi_p^{bp}, \tag{4.2}$$

where k_{fi} and k_{bp} are permeabilities of the clot due to fibrin fibres and bound platelets, respectively. The Hill functions ϕ_p^{fi} and ϕ_p^{bp} were used ensure that there is no flow restriction in regions with no fibrin or platelet aggregates, while flow restriction increases to half of its maximal value as fibrin and platelet concentrations approaches $C_{fi,50}$ and $C_{bp,50}$, respectively. According to Anand *et al.* [276], the concentration of a fibrin gel at plasma level fibrinogen concentration was assumed to be greater than 600 nM, i.e., a fibrin gel was assumed to be formed when concentration of fibrin reached 600 nM. Based on this and the measurments done by Wufsus *et al.* [280], I set $C_{fi,50} = 600$ nM, $C_{bp,50} = 7 \times 10^5$ platelets/μm^3, $k_{fi} = 1.2 \times 10^{-1}\mu$m^2, and $k_{bp} = 3.1 \times 10^{-1}\mu$m^2. I also set $n = 4$ to ensure a sharp boundary between the clot and blood while maintaining the numerical stability.

Fluid-phase chemical species

I denote by C_{pt}, C_{th}, C_{at}, C_{fg}, C_{fi}, the bulk concentrations of prothrombin, thrombin, anti-thrombin, fibrinogen, and fibrin, respectively. Transport of each species was modelled using the advection-diffusion-reaction equation:

$$\frac{\partial C_i}{\partial t} + (\boldsymbol{u} \cdot \nabla)C_i = D_i \nabla^2 C_i + S_i, \tag{4.3}$$

where C_i is the species concentration, D_i is the diffusion coefficient, and S_i is the reaction term.

Thrombin generation was assumed to occur on the surface of resting and activated platelets and the platelets bound to the clot. The kinetics of the reactions was assumed as second order chemical reactions with kinetic constants k_{th}^{rp}, k_{th}^{ap}, and k_{th}^{bp}, respectively. Thrombin inhibition by anti-thrombin was also modelled as a second order reaction with kinetic constant, k_{th}^{at}. Thrombin-mediated fibrin generation was assumed to occur according to Michaelis-Menten kinetics with k_{fi}^{th} and $k_{m,fi}^{th}$ as kinetic constants. The reaction source terms in (4.3) were formulated for each species as:

$$S_{pt} = -k_{th}^{rp}C_{rp}C_{pt} - k_{th}^{ap}C_{ap}C_{pt} - k_{th}^{bp}C_{bp}C_{pt} \tag{4.4}$$

$$S_{th} = k_{th}^{rp}C_{rp}C_{pt} + k_{th}^{ap}C_{ap}C_{pt} + k_{th}^{bp}C_{bp}C_{pt} - k_{th}^{at}C_{at}C_{th} \tag{4.5}$$

$$S_{at} = -k_{th}^{at}C_{at}C_{th} \tag{4.6}$$

$$S_{fg} = -S_{fi} = -k_{fi}^{th}C_{th}C_{fg}/(k_{m,fi}^{th} + C_{fg}). \tag{4.7}$$

Platelet activation and binding

Transport of resting, C_{rp}, and activated, C_{ap}, platelets were modelled using (4.3). The same equation was solved for bound platelets, C_{bp}, but advection and diffusion terms were removed to prevent platelets from being transported once recruited by the clot.

Platelet activation by thrombin and already activated platelets were modelled as first order reactions with k_{pa}^{th} and k_{pa}^{ap} as kinetic constants of activation by thrombin and activated platelets, respectively. Platelet activation by thrombin was assumed to occur when thrombin concentration was greater than 9.11×10^{-1} nM [278]. This was modelled by multiplying the associated reaction source by a Hill activation function, ϕ_{pa}^{th} with $C_{th,50} = 9.11 \times 10^{-1}$ nM and $n = 4$ to ensure a steep and switch-like response around the threshold concentration.

Leiderman and Fogelson [277] assumed platelet aggregation and deposition at the site of injury to be proportional to the free platelet concentration and value of a binding affinity function, a Hill function, representing proximity of free platelets to already

Table 4.1: Model parameter values

Biochemical reactions kinetic constants

k_{th}^{rp}	6.50×10^{-10} U PLT^{-1}s^{-1}μM^{-1}	[278]	k_{th}^{ap}	3.69×10^{-9} U PLT^{-1}s^{-1}μM^{-1}	[278]
k_{th}^{bp}	6.50×10^{-10} U PLT^{-1}s^{-1}μM^{-1}	[278]	k_{th}^{at}	7.083×10^{-3} μM^{-1}s^{-1}	[278]
k_{fi}^{th}	59.00 s^{-1}	[276]	$k_{m,fi}^{th}$	3160 nM	[276]
k_{pa}^{th}	0.50 s^{-1}	[275]	k_{pa}^{ap}	0.30 nM^{-1}s^{-1}	[275]
k_{pa}^{bp}	0.30 nM^{-1}s^{-1}	[275]	k_{pb}	1.00×10^{4} s^{-1}	[277]

Diffusion coefficients

D_{pt}	5.21×10^{-7} cm²s^{-1}	[276]	D_{th}	6.47×10^{-7} cm²s^{-1}	[276]
D_{at}	5.57×10^{-7} cm²s^{-1}	[276]	D_{fg}	3.10×10^{-7} cm²s^{-1}	[276]
D_{fi}	2.47×10^{-7} cm²s^{-1}	[276]	D_{rp}	2.50×10^{-7} cm²s^{-1}	[277]
D_{ap}	2.50×10^{-7} cm²s^{-1}	[277]			

bound platelets. Fibrin generation was not considered by Leiderman and Fogelson [277]. In the present model, I considered thrombin-induced fibrin generation and its effect on platelet trapping and aggregation. I assumed platelet recruitment and deposition to depend on the concentration of free platelets and value of a function representing fibrin-platelet. I used a second order Hill function ϕ_{pb}^{fi} with $C_{fi,50} = 60$ nM, i.e., 10% of the threshold concentration at which fibrin clot is said to be formed, i.e., 600 nM. According to the above, the reaction source terms for resting and activated platelets were formulated as:

$$S_{rp} = -k_{pa}^{th}\phi_{pa}^{th}C_{rp} - k_{pa}^{ap}C_{rp} \tag{4.8}$$

$$S_{ap} = k_{pa}^{th}\phi_{pa}^{th}C_{rp} + k_{pa}^{ap}C_{rp} - k_{pb}\phi_{pb}^{fi}C_{ap} \tag{4.9}$$

$$S_{bp} = k_{pb}\phi_{pb}^{fi}C_{ap}. \tag{4.10}$$

4.2.3 Model parameters and initial concentrations

The model includes eight biochemical species and nine biochemical reactions. Values of reaction rate constants were taken from the experimental literature and are reported in Table 4.1. The parameter k_{pb} represents the rate of aggregation and deposition in the presence of fibrin. To my knowledge, this parameter has not been measured experimentally. Leiderman and Fogelson [277] estimated a fixed value for this parameter and reported only some change on the platelet density distribution in response to up to 100-fold increases of this value. I used the same value as Fogelson and Leiderman [277] and remark that as long as the value maintained though all the experiments, despite

the limited effect on platelet aggregation densities, it will not influence the case-to-case comparisons made based on the platelet aggregation density.

Values of diffusion coefficients for all species were taken from the experimental literature. The shear dependent diffusion augmentation effect of red blood cells on the diffusion of platelets was considered by two orders of magnitude increase in the expected value in normal Brownian motion [277, 281]. Platelets were assumed to be static once bound to the clot, therefore, in Table 4.1, no diffusion coefficient is reported for the bound platelets.

4.2.4 Flow-induced Platelet index (FiPi)

I defined the *flow-induced platelet index* (FiPi) as the relative difference of the platelet concentration between a closed and an open system:

$$\mathcal{P} = \frac{C_{bp}^{open} - C_{bp}^{closed}}{C_{bp}^{closed}} = \frac{C_{bp}^{open}}{C_{rp,0} + C_{ap,0}} - 1. \tag{4.11}$$

In (4.11), $C_{rp,0}$ and $C_{ap,0}$ are initial concentrations of resting and activated platelets in the clot-free blood, respectively. FiPi quantifies the effect of blood flow on transport of platelets to and from the site of clot formation and consequently on the final platelet content of the formed clot. In a closed system without any inflow or outflow, I assumed the concentration of bound platelets in a formed clot to be equal to the summation of the concentrations of resting and activated platelets at the initial state before any clot formed. However, in an open system, where blood can flow over and through the forming clot, the final concentration of bound platelets in the formed clot would be different from that in closed systems. Particularly, in flow-diverted aneurysms, it has been hypothesised that the flow entering the sac can bring resting and activated platelets into contact with the forming clot and lead to a higher concentration of platelets in the formed clot, when compared to the clot that is formed in almost absolute stasis.

4.2.5 Computational model validation

Phantom experiment for the effect of two different sized stents

Gester *et al.* [1] performed an in-vitro evaluation of intra-aneurysmal FD-induced thrombus formation. Two FDs of same type with two different diameters were deployed in a silicone phantom of a simplified lateral aneurysm; one of the FD's had a diameter of 4.00 mm (FD-4.0) the other was oversized with a diameter of 4.50 mm (FD-4.5). Blood from the cervical artery of slaughter house pigs were circulated in the
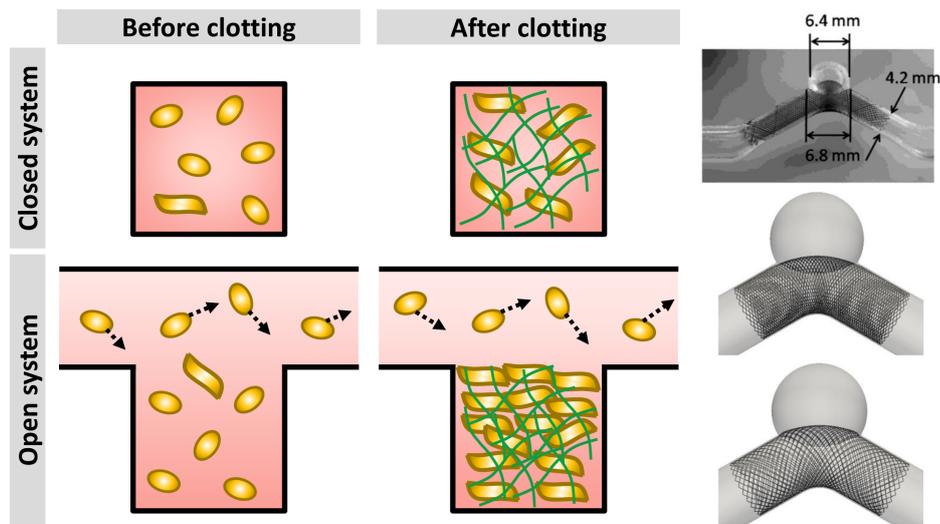
Figure 4.2: The first two columns represent the concept of the flow-induced platelet index (FiPi). In a closed system, the platelet content of the clot is equal to the initial concentration of platelets in the container before clotting occurred. In an open system, more platelets are advected with the blood flow to the clotting site, where they can attach to the clot and increase the clot platelet content. The third column shows the phantom from [1] (first row) and the computer models of the phantom (before and after FD placement) used in this study.

phantom model. PIV and Doppler sonography were performed to monitor the flow inside aneurysm. The FD-induced intra-aneurysmal clots were qualitatively evaluated once the sonography signal no longer existed (i.e., 10-12 hours after the experiments started). In the aneurysm treated with FD-4.0, a red cap-shaped clot was observed, mostly consisting of organised and platelet-rich clot formed with a growth direction opposite to the entering flow jet. In the aneurysm treated with the oversized stent, FD-4.5, a less platelet-rich clot filling almost the entire sac without any clear growth direction was observed with only a rigid (platelet-rich) region near the center of the aneurysm.

Computer model of the phantom experiment and the flow diverters

A computer model of the phantom was built using ANSYS Design Modeler v16.2 (Ansys Inc., Canonsburg, PA, USA). Geometric models of the deployed FD's were created using the fast virtual stenting (FVS) method [282]. According to the study [1], each FD consisted 24 wires of 40 μm thickness and mean porosities of the FD's in their deployed configuration were 72% and 65% for FD-4.5 and FD-4.0, respectively. Virtual stenting model parameters were chosen so that the digital FD models had the same geometrical characteristics. Since I were only interested in the effect of FDs on the
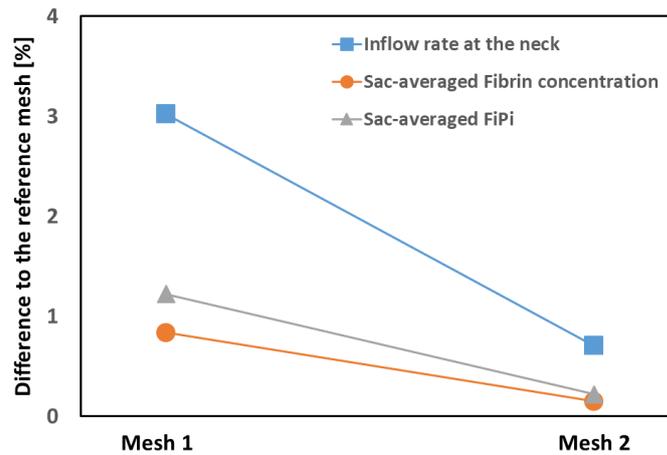
Figure 4.3: Mesh test outcomes for the non-oversized stent (FD-4.0). Mesh independence tests performed using volumetric meshes at coarse (Mesh 1), medium (Mesh 2), and fine (i.e., the reference mesh) refinement levels near the struts. For each of the examined variables, percentage differences were calculated with respect to the values obtained using the reference mesh.

intra-aneurysmal flow, to reduce the computational costs, the FD models were clipped and portions of the FDs laying entirely on the vessel wall were removed. The effect of partial stent modelling on intra-aneurysmal haemodynamics was proven negligible in previous studies [283].

Numerical simulations

Volumetric meshes were generated using ANSYS ICEM CFD v16.2 (Ansys Inc., Canonsburg, PA, USA). Element sizes in the core region of the domain were set according to the @neurIST processing toolchain where mesh independence tests on non-stented aneurysms were performed as described in [243]. Stuhne and Steinman [68] suggested that the mesh resolution in the vicinity of the stent wires needs to be about one-third of the wire's radius to achieve an accurate flow solution around the struts. In this study, mesh independence test was performed with three levels of refinement around the struts maintaining the mesh size in the core region. A coarse mesh (maximum edge size of 0.02 mm on the wires), a medium size mesh (maximum edge size of 0.01 mm on the wires), and a fine mesh (maximum edge size of 0.005 mm on the wires) were considered while the fine mesh used as the reference in the test. Mesh independence was performed based on the inflow rate at the aneurysm neck and the sac-averaged concentrations of the fibrin and platelets, and mesh independence was assumed to be reached when the solutions differed less than 1% from the reference-mesh solutions (see Figure 4.3). Mesh independence was obtained for the medium size mesh where

tetrahedral elements with maximum edge size of 0.2 mm and five layers of prismatic elements with a maximum edge size of 0.1 mm were used to discretise the core region of the computational domain. Around the stent struts, five layers of prismatic elements with a maximum edge size of 0.01 mm were used. This resulted in volumetric meshes with 13 and 12 million total number of elements for the FD-4.0 and FD-4.5 cases, respectively.

Three sets of simulations were performed for each of the FD-4.0 and FD-4.5 cases: (i) steady-state simulation of intra-aneurysmal haemodynamics before and after stent placement; (ii) transient pulsatile-flow simulation of intra-aneurysmal haemodynamics before and after stent placement (to enable comparisons with PIV reported by Gester *et al.* [1]; and (iii) transient steady-flow simulation of intra-aneurysmal haemodynamics and biochemistry before and after stent placement. The system of momentum transport (4.1) and transport equations for biochemical species (4.3) were solved in ANSYS CFX v16.2 (Ansys Inc., Canonsburg, PA, USA) using a finite volume method. CFX's Finite Rate Chemistry combustion built-in model was used to simulate blood flow in which thrombosis biochemical reactions occur. Second-order-accurate discrete approximations were used both in space and time, i.e., a second-order advection scheme and a second-order backward Euler transient scheme. CFX's Automatic time-scale control was used in the steady-state simulations. Solutions of the steady-state simulations and those of unsteady simulations at each time step converged when maximum residual of the computational domain was less than 5×10^{-4}. Concentration of each species at inlet was set at their normal value in human blood. The inlet concentrations of thrombin and fibrin were set to zero [276]. Prothrombin, anti-thrombin, and fibrinogen were assumed to have inlet concentrations of 1400, 2410, and 7000 nM, respectively [276]. Concentration of resting platelets at inlet was set to 2×10^8 platelets per millilitre and 5% of this concentration was assumed as the level of background platelet activation [278]. All model variables were initialised at steady state using a steady-state simulation with all the reaction terms off. Once the variables were initialised, unsteady-state simulations of the reactive flow were performed to cover a 30 seconds time interval. The time-step size was set to 0.01 second according to a time-step size independence test with a 2% agreement criterion on velocity and concentrations obtained from different solutions.

4.3 Results

4.3.1 Aneurysmal haemodynamics before/after flow diversion

In steady-state simulations of flow before FD placement, sac-averaged velocity, residence time, and shear rate were 0.04 m/s, 0.65 s, and 89.66 s^{-1}. After flow diversion with the FD-4.5, sac-averaged velocity and shear rate were reduced by 81% and 79%, respectively, and the sac-averaged residence time increased by 200%. Relative reductions in the aneurysm treated with FD-4.0 were 94% for both sac-averaged velocity and shear rate, and the sac-averaged residence time increased by almost 1000% in this case. Inflow rate at the aneurysm neck reduced by 74% and 89% in the aneurysms treated with FD-4.5 and FD-4.0, respectively. Figure 4.4 shows intra-aneurysmal haemodynamics on the aneurysm sagittal mid-plane before and immediately after FD deployment before any clot formed. To enable a qualitative comparison with the PIV measurements made in [1], I ran pulsatile flow simulations, with no chemical reaction, and presented velocity contour plots at peak systole. In Figure 4.4, shear rate and residence time contour plots are taken from steady-state simulations and represent the time-averaged values.

4.3.2 Thrombus formation and comparison to in-vitro observations

Unsteady simulations of FD-induced thrombosis covered a 30 s interval after FD deployment. According to previous studies [276, 284], The clot was assumed to be formed in regions where the fibrin concentration is greater than 600 nM. Figure 4.5 (first row) shows the contour plots of the fibrin concentration inside the aneurysm along the sagittal mid-plane at the end of the simulation. The white solid iso-lines, drawn at fibrin concentrations of 600 nM, show the thrombus front. In fibrin contour plots, the dark red is associated with fibrin concentrations greater than 3500 nM, showing an almost complete conversion of plasma fibrinogen into fibrin. In agreement with the observations in [1], the simulations showed that both FDs resulted in formation of a clot that filled nearly the entire sac. In the FD-4.0 case, more pronounced formation and anchorage of fibrin strands to the proximal region of the FD were reported in the phantom experiments once the clot began to form. A proximal-to-distal direction of clot growth was reported in the FD-4.0 case, as opposed to no clear growth direction in the case treated with FD-4.5. Based on the transient results (see fibrin concentration contour plots at $t = 10$ s in Figure 4.5), I observed that in the aneurysm treated with FD-4.0, the clot started to form from the aneurysm proximal region and grew in a direction opposite to the entering flow jet direction to fill the aneurysm. In the aneurysm treated
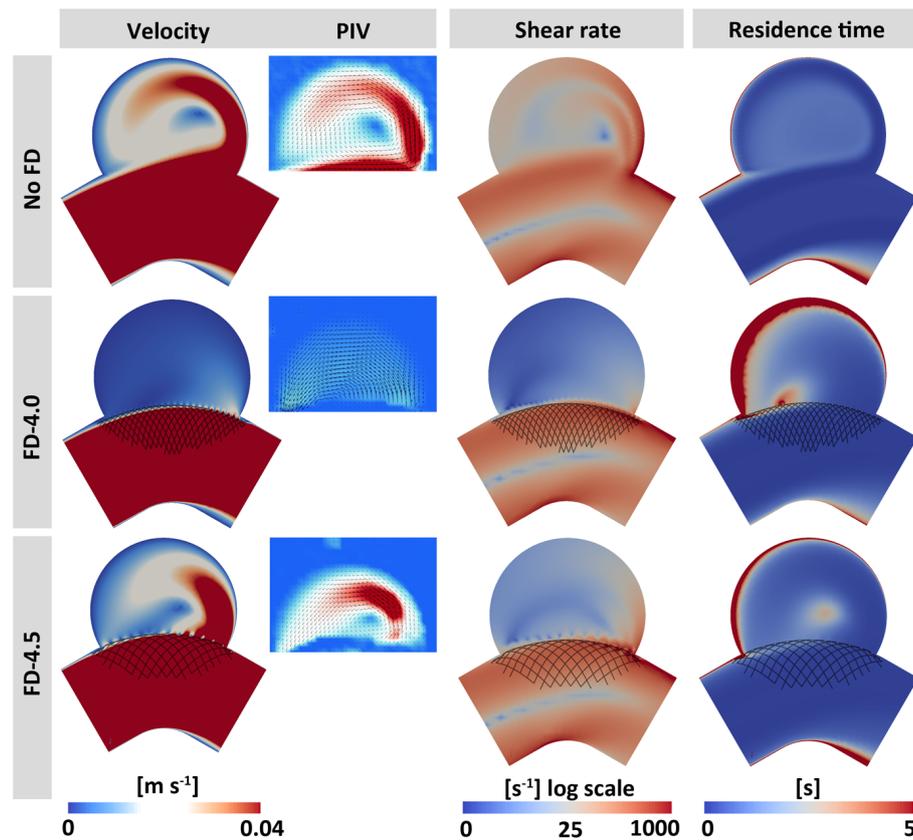
Figure 4.4: Intra-aneurysmal haemodynamic quantification before and immediately after FD deployment. Velocity quantifications were made at the peak systole to enable comparisons with PIV measurements made in [1].

with FD-4.5, there was also a clot forming in the central part of the aneurysm (the central recirculation zone), growing without any preferred direction. I also observed a thicker band of high fibrin concentration started from the proximal region of FD and extended across the sac to the upper distal wall.

Figure 4.5 (second row) shows sagittal mid-plane contour plots of FiPi, platelet content of the formed clot normalised by initial concentration platelets in thrombus-free blood. I remark that FiPi can be used to measure the effect of blood flow on the platelet content of the clot. In the FD-4.0 case, the results showed a platelet-rich clot (FiPi > 0.15) covering the entire aneurysm neck region and extended towards the upper wall. However, in the FD-4.5 case, formation of the platelet-rich clot was almost limited to the central region of the sac. I observed a less platelet-rich clot at the proximal region of the aneurysm (in both cases) and in a small region at the centre of the platelet-rich clot formed in the centre of the aneurysm treated with the oversized FD. This observation is in agreement with the hypothesis that rapid formation of clot in regions of extensive stasis results in a less platelet-rich clot, however, as the clot grows
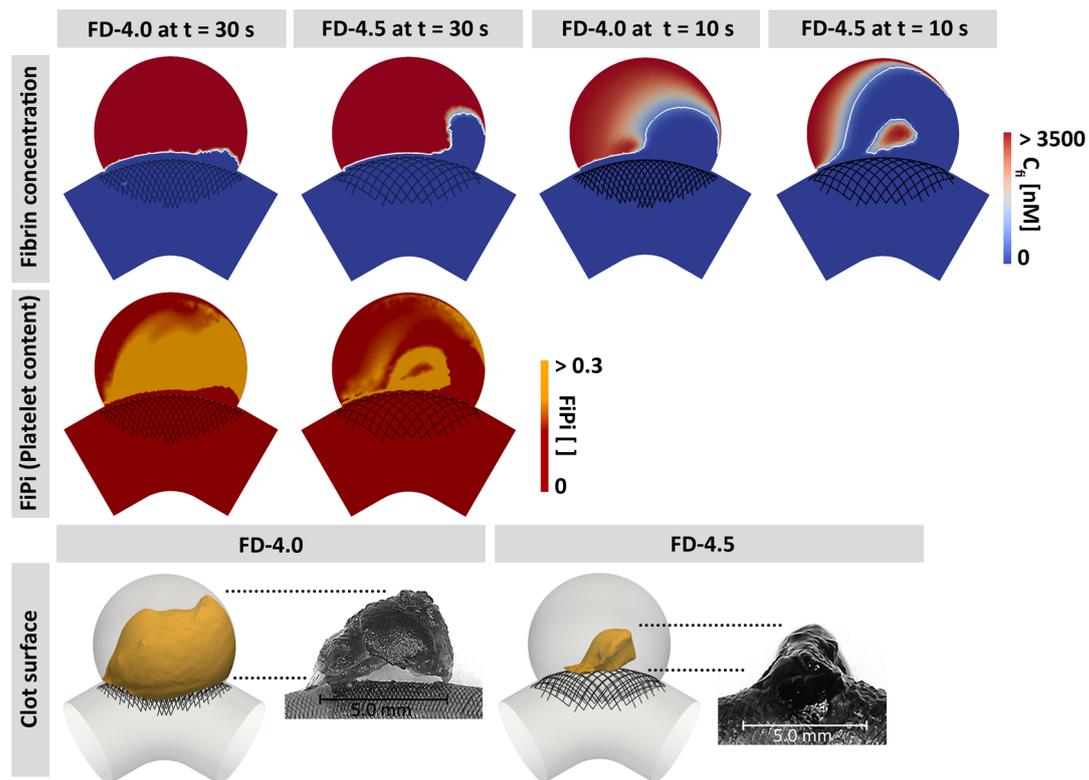
Figure 4.5: Thrombosis modelling in flow diverted aneurysms. In the first two rows, contour plots are presented on the aneurysm sagittal mid-plane. In the first row, the white solid line represents a concentration of 600 nM.

and interacts with the blood flow, more platelets take the opportunity to contact with the forming clot, which results in formation of a more platelet-rich clot [260, 263]. The above observations are in agreement with the study by Gester *et al.* [1], where a clot with a generally higher platelet content was reportedly induced by the FD-4.0, and the presence of regions with high platelet content around the central vortex were reported in the FD-4.5 case.

4.4   Discussion

4.4.1   Thrombus formation and model validation

The in-vitro study [1] compared the effects of flow diversion by two different stents in the same silicone phantom. They reported that in both cases the phantom was filled with thrombus at the end of the experiment, at which point they removed the silicone model and provided snapshots of the clots induced by each of the two FDs. To enable comparisons with snapshots presented in [1], I set a threshold on FiPi, the

measure of platelet content, and extracted from this the platelet-rich clot morphology. The morphology of the clots obtained from the model showed the best qualitative agreement with snapshots of the phantom experiment, when I used FiPi > 0.15 as a threshold. Figure 4.5, the third row, show the model predictions of the morphology of the platelet-rich clot as well as snapshots of the phantoms taken from [1]. To enable comparison, snapshots and model predictions were presented in the same spatial scale and dotted lines were used to show the clot extent above the FDs.

Location of the clot and the growth direction. In both cases, in-vitro experiments [1] showed that the clot started to form on the proximal wall. In the case of FD-4.5, the course of thrombosis continued by formation of fibrin as a result of stagnation of blood at the centre sac, i.e., the central vortex. Fibrin then filled the aneurysm without a clear growth direction. In the case of FD-4.0, the clot grew layer-by-layer and filled the aneurysm towards the distal wall. The thrombosis model correctly predicted the locations of clot deposition and the growth directions reported in these in-vitro experiments. Cebral *et al.* [272] studied 14 aneurysms successfully treated with flow diverters. They reported a layer-wise growth of clot from regions with smaller velocity, shear rates, and vorticity, i.e., the dome, towards the aneurysm neck. These results show that the thresholds based on residence time and shear rate were valid and that the model predicted realistic thrombi deposition location and growth direction.

Location of the high platelet content clot. In the case treated with FD-4.0, the simulations indicated a transformation from inertia-driven to shear-driven flow (Fig. 4.4). Flow stasis along the proximal wall resulted in rapid formation of a less platelet-rich clot. However, during the course of thrombosis, the shear-driven, well-distributed blood flow promoted the attachment of platelets to the forming clot. This finally led to the formation of a homogeneous platelet-rich clot almost in the entire aneurysm. However in the aneurysm treated with the oversized stent FD-4.5, inertial effects persisted in the post-treatment flow and circulation in the aneurysm sac was observed (Fig. 4.4). Although less pronounced than in FD-4.0, extensive stasis along the proximal wall resulted in the rapid formation of a less platelet-rich clot. I also observed formation of a clot in the central vortex. In contrast to FD-4.0, the inertia-driven flow jet was not slow enough to promote a platelet attachment. Such flow pattern resulted in a heterogeneous clot with a higher platelet concentration limited to the outer layers of clot initially formed in the central vortex (Fig. 4.5). These findings agreed qualitatively with the histological observations in [1].

Coverage of the aneurysm neck. Formation of a platelet-rich organised clot over the aneurysm neck is essential to fully close up the aneurysm and facilitate endothelialisation and formation of a neointimal layer [256, 257]. In this study, surface reactions on the FD struts were not simulated. However, in FD-4.5, I observed formation of a thin platelet-rich layer covered the proximal section of the aneurysm neck and extended to a thicker layer in the central section of the neck. However, the distal section of the neck remained patent. In contrast, in FD-4.0, I observed a thick platelet-rich layer fully covered the aneurysm neck. Similar behaviour is reported in in vitro experiments [1] and also in [256, 257] where the flow-diverter failed to fully close the sac in real aneurysms.

4.4.2 Clinical utility

Treatment planning of flow diversion is usually based on the aneurysm morphology [19, 253]. Aside from symptomatic aneurysms, large and giant aneurysms and those with a high aspect ratio or complex morphology are thought to be prone to post-FD haemorrhage [260]. Immediately after deployment, the efficacy of the FD is evaluated by measuring the reduction of flow into the aneurysmal sac by angiographic examination. However, post-operative rupture was reported in several cases with excellent immediate angiographic results after FD deployment [255, 260, 262].

In the phantom studied in this work, post-treatment haemodynamics in both FD-4.0 and FD-4.5 cases met the success criteria suggested in [273, 285, 286]. However, the two cases develop a clot with completely different qualities. This shows that purely haemodynamic assessments are insufficient to predict the likelihood of formation of a stable and occlusive clot. In order to provide a more comprehensive assessment of post-FD occlusion, it is necessary to consider the potential quality of the FD-induced clot, i.e., whether flow diversion results in a stable white clot or a red unorganised clot. The model showed promise in predicting the biochemical composition of clot structural components, fibrin and platelets, and thus, the likelihood of formation of a fibrin and platelet-rich white thrombi after flow diversion.

There is also evidence that in aneurysm treatment with FD, formation of a stable white clot over the aneurysm neck and the consequent formation of neo-intimal layer and FD endothelialisation are of superior importance than FD-induction of the thrombi inside the aneurysm body [256, 257]. Cebral *et al.* [272] trained a statistical model to predict the local occlusion based on local haemodynamics and found poorer predictions near the aneurysm neck, when compared to other regions of the flow diverted aneurysm. This magnifies the utility of models similar to the one in the present work to further improve personalised assessment of aneurysm flow diversion.

4.4.3   Limitations

All of the thrombosis model parameters were taken from experimental literature or relevant computational studies that performed sensitivity analyses, except the fibrin concentration at which rate of platelet attachment to the fibrin mesh is half of its maximum value, $C_{fi,50}$. A fixed value of this concentration used in all The simulations. My limited sensitivity analyses showed that this parameter have very small effects of the location and extent of the thrombus deposition, and on the distribution of platelets in the final clot. More comprehensive analyses are required to determine the sensitivity of blood composition to the model parameters.

Due to the computational burden required, the time scale of the thrombosis model is not representative of the physiological time scale of FD-induced clot formation and aneurysm occlusion, i.e., weeks to months. I relate this to: (i) the extensive simplification of the thrombosis chemical network, neglecting several molecular and cellular level phenomena involved in initiation, progression, and inhibition of thrombosis course after flow diversion, (ii) neglecting phenomena like lysis, organisation, and contraction of the clot (iii) neglecting the effect of flow pulsation on the reactions, especially on the initiation reactions when the clot-related concentrations are very small, and (iv) the effect of anti-coagulants and anti-platelets that are both common in flow diversion patients. I did not consider such anticoagulation in the model.

Augsburger*et al.* [287] showed that flow pulsation is not a major determinant of flow diverter performance in terms of reducing aneurysmal velocity. Since I was mostly interested in the final state of the clot and not in phenomena like thrombus breakdown, I did not consider flow pulsatility and the simulations were performed using a steady-state inflow boundary condition, however, the thrombosis model can easily be run with pulsatile boundary conditions.

4.5   Conclusion

The thrombosis model in the present study was developed to predict the platelet content distribution in intra-aneurysmal clots formed after flow diversion. The predictions made by the model showed qualitative similarities in the clotting pattern and platelet composition when compared with an in-vitro phantom experiment performed by an independent research group in [1]. I also compared the model predictions against the literature on qualitative thrombotic behaviour in aneurysms treated with flow diverters.

Chapter 5

Towards a computational framework for *in-silico* clinical trials of flow diverting stents

5.1   *In-silico* clinical trials of flow diverting stents

As described in Chapter 1, by *in-silico* clinical trials of flow diverters (FDs), I refer to the trials performed to assess a flow diverting stent effectiveness in treatment of a population of *virtual patients*. What distinguishes the concept of *in-silico* clinical trials from the personalised medicine or patient-specific modelling paradigms is that the underlying models and simulations are not tailored for a specific patient, but rather should be able to represent and generate an entire population of virtual patients. Intrinsic to developing *virtual populations* needed for *in-silico* trials is collecting and analysing clinical data and developing generative statistical models to populate *envelopes* of patient morphology and physiology. The term envelope is used to refer to the entire range of possible variation of, for example, the aneurysm morphology or a physiological variable under a specific condition.

A *morphological envelope* is a population of aneurysm surface models that represents the variability of aneurysmal shapes in patients diagnosed with intracranial aneurysms. Aneurysm surface models in such virtual populations can be obtained by: (i) segmenting three-dimensional angiograms of a population of patients that is large enough to capture the morphological variability of aneurysms, or (ii) generating synthetic aneurysms using statistical models of aneurysmal shape variations, i.e., statistical shape models (see [288] for example). Creation of statistical shape models requires a population of aneurysm shapes as the training set and results in the mean shape models as well as a parameterisation of the shape variability. The model then enables generation of new shapes by non-rigid deformation of the mean shape along the modes of variation.

A *physiological envelope* is a statistical representation of intra- and inter-subject variability/uncertainty in a class of relevant physiological measures (e.g. systemic flow waveforms, heart rate, tissue and blood properties, etc.). Advanced statistical techniques have been used to quantify the model input uncertainties and propagate them to the model output spaces. For example, adaptive stochastic collocation technique has been used in [289] for uncertainty quantification and propagation in models of blood flow in the cardiovasular system. A Gaussian process approach has been used in [110] to build a data-driven model of internal carotid artery (ICA) flow rate waveforms which allows random generation of a virtual population of inflow boundary conditions for cerebrovascular computational fluid dynamics (CFD) models.

Figure 5.1 shows a schematic view of how the above models could be combined in a tensor-product way to generate a multi-dimensional space of virtual experiments on which endovascular devices can be tested using a virtual treatment workflow (Fig-
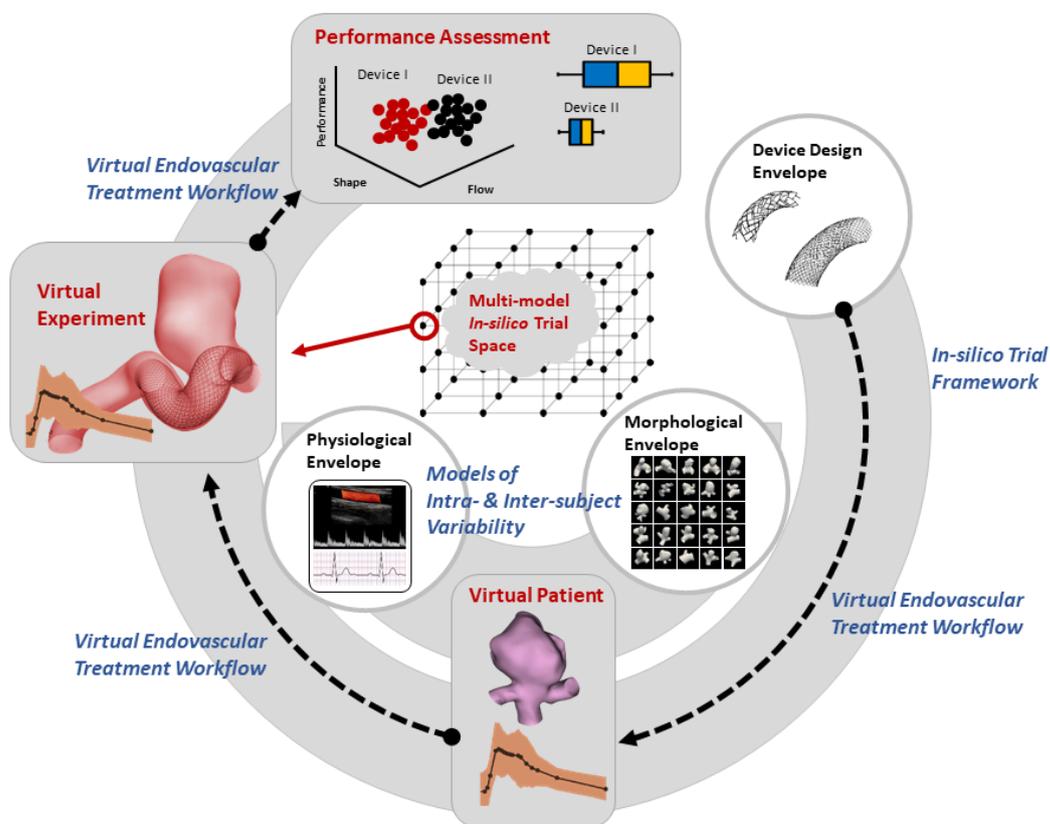
Figure 5.1: An *in-silico* trial framework for assessment treatment success in a population of virtual patients treated with flow diverting stents. Each virtual patient is treated a virtually implanted device that operates under a physiological envelope.

ure 5.1). Once an *in-silico* trial space is populated with virtual patients, a virtual endovascular treatment workflow computationally simulates the aneurysm treatment and assesses FD performance for each virtual patient. A detailed review of such a workflow and all its ingredient models is presented in Chapter 2. Semi-automated aneurysm management workflows used in @neurIST [243], and AView [290] are able to characterise pre-interventional aneurysm morphology and haemodynamics with the aim to help neuro-interventionalists in decision making and treatment planning. AngioLab [291] enables semi-automatic haemodynamic characterisation of the aneurysm after virtual treatment with coils and stents. Whether a virtual treatment workflow is designed with the aim to enable large-scale in-silico clinical trials or to aid in patient selection and treatment planning, it should be *fully-automatic* and include a device *performance indicator* that enables prediction of the flow diversion success in providing a stable aneurysm occlusion. Computational models used measures of the aneurysm morpholgy and pre-/post-deployment haemodynamics to predict the flow diversion sucess. In Chapters 2 and 4, I discussed that although such measures provide insight into the
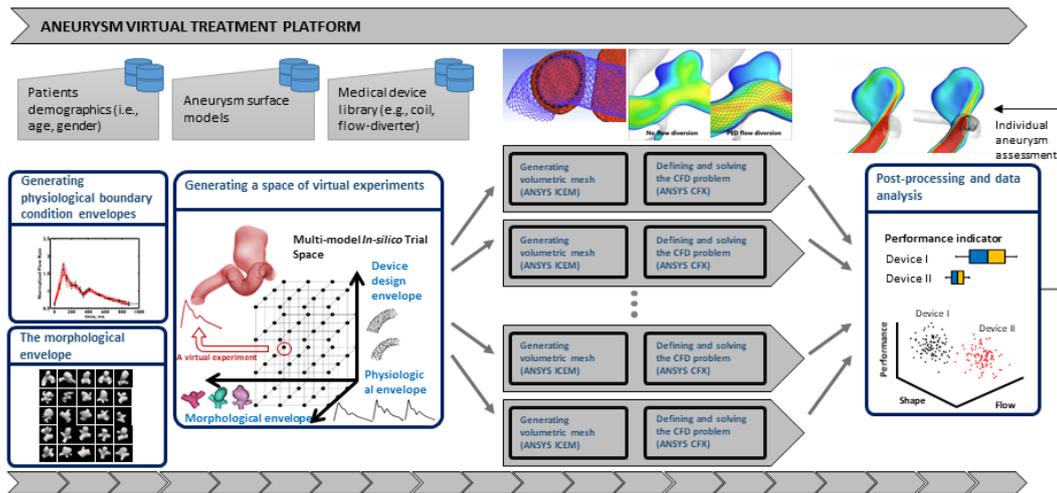
Figure 5.2: Streamlining and parallel execution of the *in-silico* trial framework processes on a computational framework. Once an *in-silico* trial space is populated with virtual experiments, a computational platform can be used for parallel execution of the costly simulations.

performance of flow diverters in aneurysms, they fail to provide accurate predictions about formation of an occlusive and stable clot after flow diversion. Ouared *et al.* [182] reported a successful flow diversion in aneurysms with at least 35% post-FD flow reduction (N = 12, balanced accuracy[1] = 83% for occlusion/no-occlusion threshold-based binary classification). Kulcsar *et al.* [39] suggested that aneurysms with an aspect ratio < 1.6 will occlude successfully after flow diversion. I applied this criterion on 8 cases reported in Kulcsar *et al.* [181] and Ouared *et al.* [182] and estimated a balanced accuracy of around 55%. Using the criterion suggested by Ouared *et al.* [182] to predict occlusion in the cohort reported in [181], I obtained a balanced accuracy of 58%. I argued that inclusion of stable clot formation likelihood as a decision variable in the computational pipeline would improve predictions made based on morphology and post-FD flow alterations.

I remark that apart from all the above mentioned ingredients, to enable large-scale *in-silico* trials, there is a need for (i) an automated workflow implemented on a computational platform that provides the capability of streamlining the virtual experiments and running them in parallel (ii) making simulations computationally as inexpensive as possible. Figure 5.2 shows how a parallel-processing platform can be utilised to run multiple virtual experiments and finally analyse the performance of each device on the virtual population.

While this thesis provided several ingredients required to build a framework for

---

[1]The balanced accuracy is defined as the arithmetic mean of specificity and sensitivity and is suggested as a measure of classification accuracy of an imbalanced test set, i.e., when the positives outnumber the negatives.

in-silico clinical trials of FDs, creation of fully-automatic framework and its implementation on a parallel-processing platform is out of the scope of this work. However, in this chapter, I present two proof of concept studies two as a preliminary step towards addressing the questions: How can an automatic framework be built for *in-silico* clinical trials of flow diverters? and, how can computationally inexpensive models be used to reduce computational costs of such trials? In the first study, I built a fully-automatic aneurysm flow modelling framework and utilised a parallel-processing platform (MULTIX, www.multi-x.org) to simulate flow in a cohort of aneurysms ($N = 54$) at rest and exercise conditions. In the second study, a computationally inexpensive, statistical framework was proposed to predict the aneurysmal wall shear stress patterns directly from the aneurysm shape.

5.2 A fully-automatic framework for aneurysmal flow simulation

[2]The main objective of this section is to showcase a fully-automatic computational framework that was developed to study the aneurysm haemodynamics under a range of physiological conditions. It has been shown that changes in wall shear stress (WSS) induced by flow variability can significantly change the CFD-based predictions of intracranial aneurysm rupture risk [109, 110]. In this study, I considered within-subject flow variability induced by changes in systolic blood pressure (BP) and heart rate (HR) during physical exercise, and studied the corresponding changes in WSS indicators, such as time-averaged WSS (TAWSS) or oscillatory shear index (OSI).

5.2.1 Materials and methods

Patient-specific vascular flow measurements

Patient-specific carotid flow data (*Lido cohort*) used in this study were part of an Alzheimer's disease study conducted at the Istituto di Ricovero e Cura a Carattere Scientifico San Camillo, Lido di Venezia, Italy, and previously reported in [292]. The cohort included 103 elderly people (age 73 ± 7 years), of whom 53 were diagnosed with mild cognitive impairment and the rest were healthy controls. Exclusion criteria included cerebrovascular disease as main aetiology, as well as the presence of any cardiovascular disease. The cohort could, therefore, be identified as elderly but healthy from the standpoint of vascular disease. The study was approved by the joint ethics

---
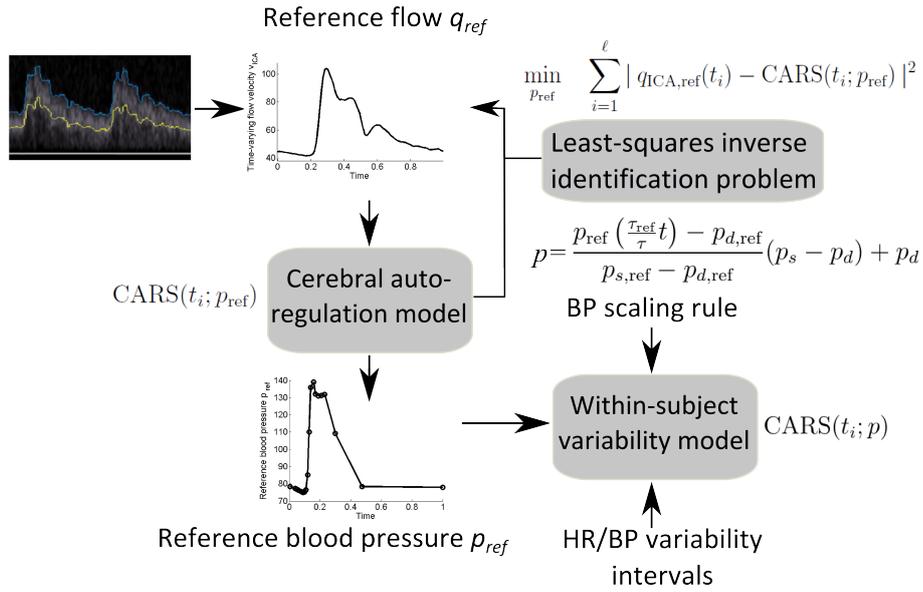
Figure 5.3: Training of the within-subject flow variability -model (5.1)–(5.4).

committee of the Health Authority Venice 12 and the IRCCS San Camillo (Protocol number 2014.08) and all participants gave informed consent prior to participation.

To measure carotid flow, ultrasound imaging (Siemens Acuson X300PE, Siemens Healthineers, Erlangen, Germany) was performed. Both left and right internal carotid waveforms were digitised from the DICOM images using `im2graph` (Shai Vaingast, `www.im2graph.co.il`). Flow velocity signals were converted to flow rates by assuming a circular cross-section and fully developed flow. The resulting flow rate signals were normalised to unit time and synchronised so that the maximum systolic upstroke point was matched between all the signals.

Statistical modelling of within-subject variability in ICA flow

Within-subject variability in ICA flow arises mainly due the changes in cardiac output, quantified here by HR and systolic blood pressure (SBP). These changes are modulated by thecerebral autoregulation system (CARS) that includes myogenic (pressure-driven), shear-induced (flow-driven), and metabolic (energy-driven) regulation mechanisms. To model within-subject variability of carotid flow, a range of arterial BP waveforms with different values of HR and SBP was considered and used a mathematical model of the CARS to generate the corresponding flow rate waveforms.

The HR model of Mader *et al.* [293] is a two-element feedback controller, for which orthostatic stress tests were previously used to identify model parameters in both

middle-aged and elderly volunteers:

$$
\begin{cases}
\dfrac{dv_1}{dt} = -(a+b+c)v_1(t) + (c-d(t))v_2(t) + (a+b)p(t) \\[2mm]
\dfrac{dv_2}{dt} = -bv_1(t) - dv_2(t) + bp(t) \\[2mm]
d(t) = \dfrac{bcf_{aut}(t)}{Mc\,p(t) - (a+c)f_{aut}(t)} \\[2mm]
f_{aut}(t) = 2.03 \cdot 10^{-6}p(t)^3 - 6.02 \cdot 10^{-4}p(t)^2 + 5.94 \cdot 10^{-2}p(t) - 1.95
\end{cases}
, \tag{5.1}
$$

where the model parameters

$$
\begin{aligned}
a &= a_m\lambda + (1-\lambda)a_e, & b &= b_m\lambda + (1-\lambda)b_e, \\
c &= c_m\lambda + (1-\lambda)c_e, & M &= M_m\lambda + (1-\lambda)M_e
\end{aligned}
\tag{5.2}
$$

depended piecewise linearly on age x_{age}:

$$
\lambda =
\begin{cases}
1, & \text{if } x_{\text{age}} < 35 \\[2mm]
\dfrac{75 - x_{\text{age}}}{40}, & \text{if } 35 \le x_{\text{age}} \le 75 \\[2mm]
0, & \text{if } x_{\text{age}} > 75
\end{cases}
\tag{5.3}
$$

Finally, the flow velocity in the middle cerebral artery (MCA) was obtained as:

$$
v_{\text{MCA}}(t) = M(p(t) - v_1(t)) + \overline{v}, \tag{5.4}
$$

where $\overline{v}$ corresponds to the time-averaged flow velocity. To translate MCA flow velocities to ICA flow rates, a linear relationship was assumed between ICA and MCA flows:

$$
q_{\text{ICA}} = \gamma A_{\text{ICA}} v_{\text{MCA}}, \tag{5.5}
$$

where A_{ICA} was the cross-sectional area of the ICA, and the VMCA/VICA index was $\gamma = 1.67 + 0.005 \times x_{\text{age}}$ for women and $\gamma = 2.00$ for men, as proposed in [294].

To drive the CARS model, the BP waveform $p(t)$ needed to be specified. For a given reference HR, it was assumed there exists a reference BP signal $p_{\text{ref}}(t)$ with SBP $p_{s,\text{ref}}$ and diastolic blood pressure (DBP) $p_{d,\text{ref}}$. The effect of HR and SBP variability on BP was then obtained by rescaling the reference BP waveform:

$$
p(t; \tau, p_s, p_d) = \frac{p_{\text{ref}}\left(\frac{\tau_{\text{ref}}}{\tau}t\right) - p_{d,\text{ref}}}{p_{s,\text{ref}} - p_{d,\text{ref}}}(p_s - p_d) + p_d. \tag{5.6}
$$

where $\tau = 60/\,\text{HR}$ is the cardiac interval. Since BP waveforms were not available

in this cohort, an inverse procedure was used to recover the reference BP from the ultrasound flow measurement by solving the least squares problem:

$$\min_{p_{\text{ref}}} \quad \sum_{i=1}^{\ell} \mid q_{\text{ICA,ref}}(t_i) - \text{CARS}(t_i; p) \mid^2, \tag{5.7}$$

where $\text{CARS}(t_i; p_{\text{ref}})$ is the output of the CARS model at time t_i when driving the model with the reference pressure $p_{\text{ref}}(t)$, and $q_{\text{ICA,ref}}$ is the reference ICA flow waveform. The within-subject variability model fitting process is graphically represented in Fig. 5.3.

Study on the effect of exercise on aneurysm flow

I studied the specific case of flow prediction in intracranial aneurysms (IAs). The mechanobiological growth and rupture process of IAs has been linked to changes in WSS patterns. A number of CFD studies [40, 110, 295] have looked at the effect of cerebral blood flow (CBF) fluctuations in WSS patterns, but none to my knowledge have considered the effect of the CARS. Quantities of interest include time-averaged WSS (TAWSS), oscillatory shear index (OSI), and transverse WSS (TransWSS):

$$\text{TAWSS}(x) = \frac{1}{T_{\text{period}}} \int_{T_0}^{T_0 + T_{\text{period}}} |\boldsymbol{\tau}_w(x, t)| \, dt;$$

$$\text{OSI}(x) = \frac{1}{2} \left(1 - \frac{\left| \int_{T_0}^{T_0 + T_{\text{period}}} \boldsymbol{\tau}_w(x, t) \, dt \right|}{\int_{T_0}^{T_0 + T_{\text{period}}} |\boldsymbol{\tau}_w(x, t)| \, dt} \right); \tag{5.8}$$

$$\text{TransWSS}(x) = \frac{1}{T_{\text{period}}} \int_{T_0}^{T_0 + T_{\text{period}}} |\boldsymbol{\tau}_w(x, t) \cdot (\hat{p} \times \hat{n})| \, dt,$$

where $\hat{n}$ is the surface normal, and the unit vector $\hat{p}$ in the direction of the time-averaged WSS vector can be calculated as:

$$\hat{p}(x) = \frac{\int_{T_0}^{T_0 + T_{\text{period}}} \boldsymbol{\tau}_w(x, t) \, dt}{\left| \int_{T_0}^{T_0 + T_{\text{period}}} \boldsymbol{\tau}_w(x, t) \, dt \right|}. \tag{5.9}$$

To enable comparison of TransWSS across cases, I calculated the relative TransWSS (rTransWSS) as the TransWSS normalised by the TAWSS at each surface point [110]. All point-wise quantities were averaged over the aneurysmal sac and used for population-specific analyses. Previous studies indicate that endothelial regions at-risk of rupture can be characterised as having low TAWSS but highly fluctuating WSS (both high OSI and high TransWSS) [38]. As a sudden rise in blood pressure may trigger the rupture of an aneurysm [296, 297], I investigated whether changes in CBF experienced in hy-

pertensive conditions play a role in altering the WSS patterns.

To generate a virtual cohort of IAs to test the differences in WSS between rest vs. exercise, patient-specific vascular surface models ($N = 54$) were segmented from previously acquired 3-D rotational angiography images in the @neurIST project [298]. Vascular models were discretised using unstructured volumetric meshes in ANSYS ICEM v16.2 (Ansys Inc., Canonsburg, PA, USA). Tetrahedral elements with maximum edge size of 0.2 mm were used and three layers of prismatic elements with an edge size of 0.1 mm were used to create boundary layers. Blood flow in the IA was modelled using the unsteady Navier–Stokes equations. Blood was assumed to be an incompressible Newtonian fluid with a density of 1066 kg/m^3 and viscosity of 0.0035 Pa·s. To ensure fully developed flow, the computational domain was extended at the inlet boundary by an entrance length proportional to the inlet boundary maximum Reynolds number. The Navier–Stokes equations were solved in ANSYS CFX v16.2 (Ansys Inc., Canonsburg, PA, USA). The unsteady Navier-Stokes equations were solved in ANSYS CFX v16.2 (Ansys Inc., Canonsburg, PA, USA) using a finite-volume method. Second-order-accurate discrete approximations were used both in space and time, i.e., a second-order advection scheme and a second-order backward Euler transient scheme. The cardiac cycle was discretised in time into 200 equal steps. Element and time-step sizes were set according to the neurIST processing toolchain where mesh and time-step size dependecy tests were performed on WSS, pressure, and flow velocity at several points in the computational domain as described by [298].

No patient-specific flow measurements were available in the @neurIST cohort. Instead, the mean waveform (different for men/women) from the Lido cohort was used as the baseline flow waveform. The baseline waveform was used as inlet boundary condition to the CFD models of aneurysm flow at rest. For each patient, obtain patient-specific physiologically-relevant flow waveforms and to enable population-wide comparisons, Poiseuille's law was used to scale the mean waveform such that the time-averaged WSS was 1.5 Pa at the inlet. We modeled differences between rest and exercise by increasing the HR from 66 bpm (at rest) to an elevated level of 145 bpm (during exercise), i.e., an increase by a factor of 2.2 [299]. These values were used as parameters in the within-subject flow variability model of Sect. 2.3. The baseline pressure waveform was determined for each case by solving problem (5.7). After solving the inverse problem, the systolic BP was correspondingly increased by a factor of 1.3 [299] in formula (5.6) to simulate effects of exercise and used to drive the CARS model and obtain the ICA waveform. The ICA waveforms where then used as inlet boundary condition to the CFD models of aneurysm flow during exercise. Zero-pressure boundary conditions were imposed at all outlets.
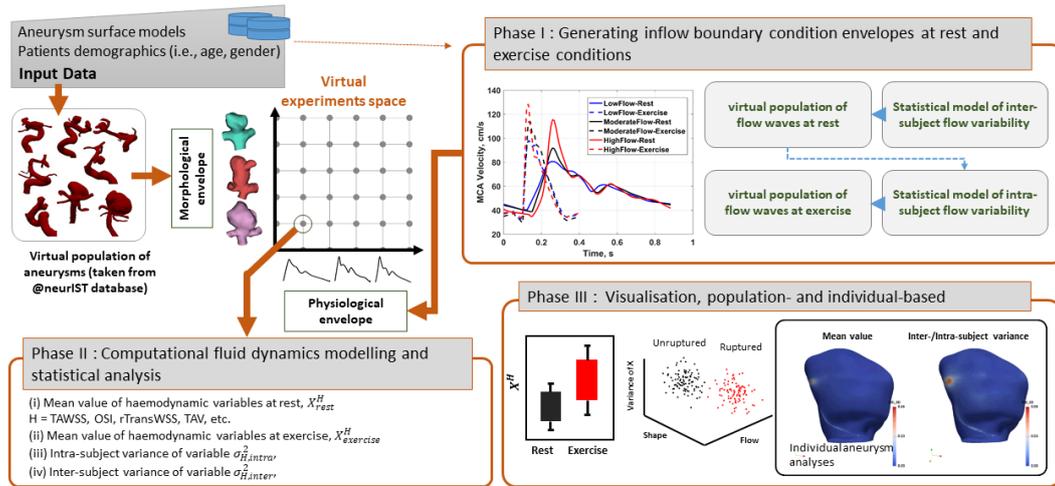
Figure 5.4: A framework for aneurysm flow modelling: investigation of the effect of exercise on aneurysm flow.

Aneurysm flow modelling framework

As mentioned above, we chose a cohort of 54 aneurysms taken from the @neurIST database as the morphological envelope. The aneurysms were already segmented using geodesic active region segmentation algorithm and the surface models were used in the study [58]. As depicted in Figure 5.4, this framework includes three main steps: (i) generating boundary condition envelopes for rest and exercise conditions, (ii) computational fluid dynamics modelling and statistical analysis of the results, and (iii) visualisation population- and patient-specific results. Since there was no endovascular device implantation, the trial space was built only by combining two components, i.e., the morphology and the physiology envelopes. In a preliminary step, aneurysm surface models were first used to generate volumetric meshes while the inlet areas were measured and used for scaling the inlet flow boundary condition. Figure 5.5 shows details of the workflows used in each step. In step one, reference waveforms taken from the Lido cohort were used to generate flow waveforms at rest and exercise and the trial space was populated with virtual patients, each had a morphology and flow boundary condition. Simulations were performed in the second step, and population- and patient-specific results were visualised at the third step. Workflows in this framework were built using Apache Taverna software [300] and ran on the `MULTIX` platform.

Results

Flow variability in the host artery (either the internal carotid, middle cerebral, or posterior communicating artery) during rest and exercise was measured with two different
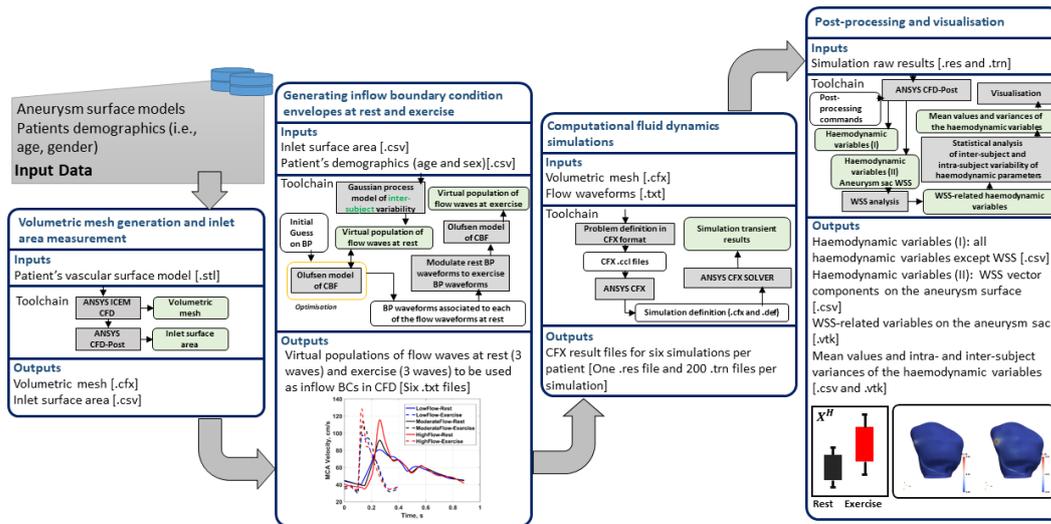
Figure 5.5: A framwork for aneurysm flow modelling: ingredient tools and workflows.

indicators: mean flow (FLOW) and PI. The variabilities of these indicators as well as the WSS-related quantities measured in the aneurysm are reported in in Table 5.1. Due to the effects of the CARS, CARS only fluctuated moderately ($< 10\%$) even when the HR was increased considerably. Meanwhile, the PI increased by over 100% in certain cases. In practice, all WSS-related indicators (TAWSS, OSI, rTransWSS) experienced on average an increase when moving from rest to exercise (Table 5.1). By far the largest increase was observed in OSI, which more than doubled on average during exercise. rTransWSS was considerablly less sensitive to flow fluctuations, being only somewhat more sensitive than TAWSS. In my previous study [110] TransWSS was similarly found to be a smoother measure of WSS fluctuations.

Changes in the absolute values of WSS and OSI might have relatively little physiological meaning unless critical thresholds are met for upregulating atheroprotective (for high TAWSS) or inflammatory pathways (low TAWSS and high OSI) in the endothelium. Therefore, I also studied areas of low TAWSS (defined as TAWSS < 0.4 Pa) and high OSI (defined as OSI > 0.4) relative to the total area of the aneurysmal sac. Their changes are also reported in Table 5.1. It was observed that relative area of low TAWSS decreased on average, while the relative area of high OSI increased. To understand better the interplay of TAWSS and OSI, in Fig. 5.6 I present the case of a 41-year-old woman with a posterior communicating artery aneurysm. In this case, a large increase in host vessel pulsatility (ΔPI $= 102\%$) lead to a corresponding large increase in TAWSS (ΔTAWSS $= 39\%$) and OSI (ΔOSI $= 129\%$). It should be noted that OSI tends to be a spatially concentrated measure of flow variability, so that even a large increase in OSI only effects a small part of the aneurysmal wall. At the same

Table 5.1: Within-subject variability of flow- and WSS-related quantities in $N = 54$ intracranial aneurysms. Values given are cohort means (std. dev. in parentheses).

Indicator	Rest	Exercise	Relative difference
FLOW [ml/min]	240 (99)	245 (109)	2.00% (2.22%)
PI	1.18 (0.00)	2.13 (0.16)	80.3% (13.5%)
TAWSS	4.78 (4.17)	5.78 (4.93)	27.2% (19.6%)
OSI	0.027 (0.023)	0.053 (0.035)	124.0% (84.1%)
rTransWSS	0.168 (0.069)	0.240 (0.084)	48.1% (29.3%)
rArea Low TAWSS [%]	12.87 (22.07)	7.42 (15.04)	-58.6% (27.8%)
rArea High OSI [%]	2.30 (2.60)	5.09 (5.37)	165% (143%)

Table 5.2: Correlation coefficients between flow variability in the host artery (ICA) and WSS variability in $N = 54$ intracranial aneurysm.

Comparison	Pearson's ρ	p-value
ΔFLOW vs. ΔTAWSS	0.277	0.043*
ΔFLOW vs. ΔOSI	-0.132	0.340
ΔFLOW vs. ΔrTransWSS	-0.100	0.473
ΔFLOW vs. ΔrAreaLowTAWSS	-0.276	0.069
ΔFLOW vs. ΔrAreaHighOSI	-0.064	0.649
ΔPI vs. ΔTAWSS	0.430	0.001*
ΔPI vs. ΔOSI	-0.200	0.148
ΔPI vs. ΔrTransWSS	-0.225	0.102
ΔPI vs. ΔrAreaLowTAWSS	-0.183	0.237
ΔPI vs. ΔrAreaHighOSI	-0.101	0.469

time, while TAWSS increased in most regions it remained low in the region where OSI was simultaneously elevated. Thus the actual change in rupture risk should be evaluated based on a combined informations about TAWSS and WSS pulsatility indicators, including analysis of the spatial patterns of WSS.

Linear correlations between changes in flow vs. changes in WSS are reported in Table 5.2. It was found that, on average, TAWSS increases were associated incresses in both FLOW and PI, while the correlations between flow and OSI/rTransWSS changes were not statistically significant.

Discussion

Computational fluid dynamics modelling is a promising tool for virtual treatment planning in cardio- and cerebrovascular disease, but requires patient-specific boundary conditions to achieve results that are relevant to the specific patient's physiology. If normative flow boundary conditions are used instead, derived quantities of flow, such as WSS, may incur large errors and uncertainties. In the context of intracranial aneurysm
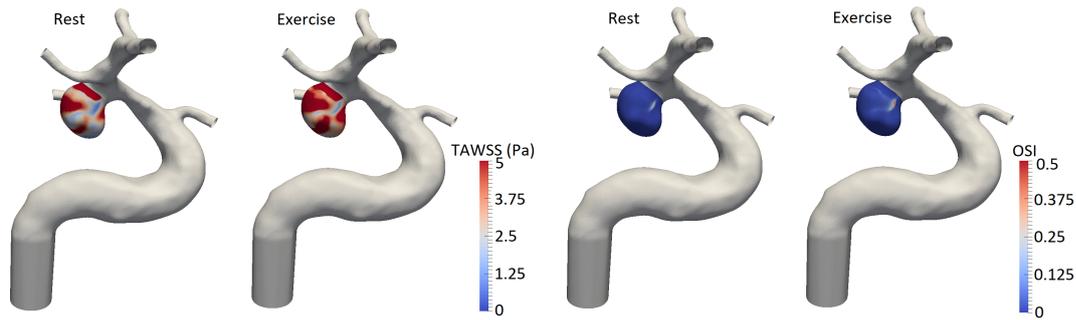
Figure 5.6: Example of flow in a posterior communicating artery aneurysm of a 41-year old female where a large increase in host vessel pulsatility (ΔPI = 102%) leads to corresponding large increases in TAWSS (ΔTAWSS = 39%) and OSI (ΔOSI = 129%).

flow modelling, previous meta-analysis [301] showed that the use of patient-unspecific boundary conditions leads to a moderate-sized effect (Hedges' $g = 0.30$) when evaluating WSS patterns on the aneurysmal endothelium. This uncertainty can be multiplied by the presence of within-subject flow variability. However, in clinical practice only a single flow measurement is usually performed and no estimate of systemic variability is available to guide the modeller as to the variability in the flow measurements.

A within-subject flow variability model was developed that mimics the response of the cerebral autoregulation system to cardiac output variability. This model can be used to extend a single baseline carotid flow measurement to a range of CBF experienced during the person's daily activities. As a concrete example, I performed CFD simulations in 54 intracranial aneurysms where the intra-subject flow variability model was used to generate waveforms at rest and during physical activity. The results showed that physiological changes in CBF during increased physical activity may induce fluctuations an order of magnitude higher in certain WSS-related quantities, such as OSI (a 2% mean increase in flow lead to a 124% mean increase in OSI in the virtual cohort). This indicates that OSI may be too sensitive to flow uncertainty to be reliably used for rupture-risk evaluation. A partial recipe to this problem is to use alternative WSS indicators that are robust to flow fluctuations. Specifically, I showed that TransWSS was less sensitive to flow fluctuations than OSI, so that if both indicators are equally informative for the rupture risk then TransWSS should be preferred over OSI. I remark that the study is limited in the sense that the within-subject CBF variability was controlled by a simple autoregulation model that only considers short-term effects. Long-term response to chronic disruptions in CBF, such as cardiac disease, should be modelled using a more advanced autoregulation model.

5.3   A computationally inexpensive model for haemodynamic quantification in aneurysms

[3]This study is presented as a proof of concept to show how computationally inexpensive models can be used to accelerate costly simulations in an *in-silico* trial framework. Here, I addressed the problem of estimating WSS on the surface of patient-specific image-based models of vascular aneurysms. Such estimates are clinically relevant as abnormal endothelial cell response to WSS variations is hypothesised to be one of the driving factors in the inflammatory process that leads to aneurysm growth and rupture. Boussel *et al.* [302], for example, reported a correlation between aneurysm growth and areas of low time-averaged WSS. WSS in small vessels is difficult to be estimated accurately from flow imaging, so that it is often evaluated indirectly through CFD simulations.

CFD simulations can be very time-consuming, especially in the context of rapid clinical decision making or in trials where haemodynamic analyses on a large-scale virtual population are of interest, e.g., *in-silico* clinical trials. Thus there is a need to develop methods that predict WSS directly from image-based models of aneurysms, preferably without relying on costly CFD simulations. One way to do this is by applying machine learning algorithms to build statistical models. This has been previously proposed e.g. by Schiavazzi *et al.* [130] to learn the relation between inlet/outlet flow and pressure in vascular flows. Statistical models for aneurysms are not found in the literature, possibly due to the heterogeneity of shapes and the consequent problems in establishing point correspondences.

To successfully predict WSS based only on the morphology of the aneurysm, I hypothesised that we deal with *geometry-driven flow*. This means that the time-averaged flow (and consequently the time-averaged WSS) is determined mainly by the morphology of the vasculature, and that other factors such as the mean input flow and the blood viscosity only contribute negligible fluctuation terms. Cebral *et al.* [31] performed a sensitivity analysis of various haemodynamic parameters in intracranial aneurysms (IAs), and showed that the greatest impact on the computed flow fields was indeed due to the morphology.

I proposed a framework to predict the time-averaged WSS (TAWSS) on the surface of patient-specific saccular IAs. A joint statistical model (JSM) was trained by a hybrid dataset of IA shapes and CFD-predicted aneurysmal TAWSS. I applied the method of Gooya *et al.* [288] for joint clustering and principal component analysis for building

---

statistical models. However, the published method does not provide a mechanism to predict missing values from partially observed data. The model was further extended by collapsing the JSM to a shape only model, obtaining initial TAWSS values, and further refining the result by projecting it to the JSM space.

The JSM was trained using a database of 38 patient-specific IA morphologies plus 114 TAWSS patterns (three different flow scenarios for each IA morphology). The optimal model was first selected by maximising the model evidence, and used to predict the TAWSS pattern given the IA morphology of the test aneurysm. To the best of my knowledge, this represents the first development of a statistical model for complex IA shapes that also provides predictions of WSS. While the focus here is on the TAWSS, the method is general and can also predict flow quantities in other cases where the geometry-driven flow assumption holds.

5.3.1 Materials and methods

Vascular modelling and pre-processing of shapes

A cohort of 38 IA cases were selected from the @neurIST database. Surface models of the parent vessels, the neck surface, and the aneurysm sac were previously reconstructed using the @neurIST processing toolchain as described by Villa-Uriol *et al.* in [243]. In all these cases, the IA was located at the sylvian bifurcation of the middle cerebral artery (MbifA-type), which is the most prevalent location for IAs. For each vascular model, the inlet branches were truncated at the beginning of the internal carotid artery (ICA) cavernous segment and extruded by an entry length of $5\times$ the inlet diameter to allow for fully developed flow. Outlet branches were automatically clipped 20 mm after their proximal bifurcation. Branches shorter than 20 mm were extruded before truncation. The processed vascular surface models were then used for CFD simulation of blood flow as described in the next section.

Flow simulation and post-processing of TAWSS

For each surface model, a volumetric mesh of unstructured tetrahedrons with a maximum side length of 0.2 mm was generated in ANSYS ICEM v16.2 (Ansys Inc., Canonsburg, PA, USA). Three boundary layers of prismatic elements with edge size of 0.1 mm were used to provide convergence of WSS-related quantities. Blood was considered incompressible and Newtonian with density of 1066 kg/m^3 and dynamic viscosity of 0.0035 Pa·s. Arterial distensibility was not considered.

Time-varying inlet boundary conditions were prescribed at the ICA. To account for intra-subject flow variability on the aneurysmal TAWSS, I performed multiple flow

simulations with different inflow boundary conditions for each case. A Gaussian process -model (GPM) was used to generate multiple inflow waveforms over the physiological range of variability at the ICA. This GPM was trained on subject-specific data from the study of Ford *et al.* [74], describing the statistical variance of 14 fiducial landmarks on the waveform. To simulate the high, moderate, and low flow conditions, I selected three representative waveforms from the GPM generated samples and used them as inlet boundary conditions for flow simulations. A Poiseuille profile was imposed at all times of the inlet, and zero pressure at the outlets.

The unsteady Navier-Stokes equations were solved in ANSYS CFX v16.2 (Ansys Inc., Canonsburg, PA, USA) using a finite-volume method. Second-order-accurate discrete approximations were used both in space and time, i.e., a second-order advection scheme and a second-order backward Euler transient scheme. Mesh convergence tests were performed on WSS, pressure, and flow velocity at several points in the computational domain. Unsteady simulations were run for 3 heartbeats until a periodic solution with stationary mean pressure was achieved. A total of $38 \times 3 = 114$ flow simulations were performed. Thereafter, the WSS vector field $\boldsymbol{\tau}_w(x, t)$ on the surface was reconstructed and WSS was computed as described in the previous section.

The area of interest for building the statistical model contained only the aneurysm sac. This choice was made to reduce the shape complexity due to variations of the branch vessels. For each of the 114 simulated cases, aneurysm sacs along with the TAWSS data were extracted from the complete vascular model and aligned semi-automatically by Procrustes registration according to their neck surfaces. Joint IA aneurysm sac and TAWSS field data sets were then decimated to point sets of around 600 points, so that the statistical model could be trained in a reasonable amount of time (< 30 mins).

Construction of hybrid point sets

The combined 4-D data vectors mixed both spatial (coordinates (x, y, z) of the points) and flow components (TAWSS in units of Pa). The relative magnitudes of the different components thus needed to be carefully selected to avoid biasing the joint model towards either pure shape or pure TAWSS approximations. As initial scaling, the Euclidean distance (d) of each point in the point sets from the global centroid of point sets was computed and the maximum, $d_{\max}$, was used to scale the spatial coordinates as $(\widetilde{x}, \widetilde{y}, \widetilde{z}) = (x, y, z)/d_{\max}$. TAWSS values were scaled to fall between [0,1] by dividing them with the peak TAWSS value computed across all the vectors in the training set. To open up a possibility to investigate the effect of relative weight of shape and TAWSS in the JSM, I introduced a weighting factor (α). Thus, for each case ($k = 1, \ldots, 114$)

the 4D point set was, $\mathcal{X}_k(\alpha) = [\tilde{\mathcal{Y}}_k, \alpha\tilde{\mathcal{F}}_k]$, where $\tilde{\mathcal{Y}}_k$ was the shape vector and $\tilde{\mathcal{F}}_k$ was the TAWSS vector. Note that there was no point-to-point correspondence between different shapes.

Joint statistical flow-and-shape model construction

[4]Let $\mathcal{X}_k = \{\mathbf{x}_{kn}\}_{n=1,k=1}^{N_k, K}$ denote the kth point set, where $\mathbf{x}_{kn}$ is a $D = 4$ dimensional vector containing spatial and TAWSS coordinates of the nth landmark. The statistical model can be explained by considering a hierarchy of two interacting mixture models. In D dimensions, points in $\mathcal{X}_k$ were assumed to be samples from a Gaussian mixture model (GMM) having M components. Furthermore, by consistently concatenating the coordinates of those components, $\mathcal{X}_k$ can be represented as an MD dimensional vector. These were assumed to be samples from a mixture of J probabilistic principle component analysers (PPCAs) [303]. Clustering and linear component analysis for $\mathcal{X}_k$ takes place in this high-dimensional space. The jth PPCA is an MD dimensional Gaussian specified by the mean vector $\bar{\boldsymbol{\mu}}_j$, and the covariance matrix given by $\mathbf{W}_j\mathbf{W}_j^T + \beta^{-1}\mathbf{I}$. Here, $\mathbf{W}_j$ is an $MD \times L$ dimensional matrix, whose columns encode the variation modes in the cluster j. Let $\mathbf{v}_k$ be an L dimensional vector and define $\boldsymbol{\mu}_{jk} = \mathbf{W}_j\mathbf{v}_k + \bar{\boldsymbol{\mu}}_j$, a *re-sampled* representation of $\mathcal{X}_k$ in the space spanned by principal components of the jth cluster. Meanwhile, if we partition $\boldsymbol{\mu}_{jk}$ into a series of M subsequent vectors and denote each as $\boldsymbol{\mu}_{jk}^{(m)}$, we obtain the means of the corresponding GMM.

To specify point correspondences, let $\mathcal{Z}_k = \{\mathbf{z}_{kn}\}_{n=1}^{N_k}$, and $\mathbf{z}_{kn} \in \{0,1\}^M$. The latter is a vector of zeros except for its arbitrary mth component, where $z_{knm} = 1$, indicating that $\mathbf{x}_{kn}$ is a sample from the D-dimensional Gaussian m. Moreover, let $\mathbf{t}_k \in \{0,1\}^J$, whose component j being one, $(t_{kj} = 1)$, indicates that $\mathcal{X}_k$ belongs to cluster j. It was defined

$$p(\mathbf{x}_{kn}|\mathbf{z}_{kn}, \mathbf{t}_k, \beta, \mathbb{W}, \mathbf{v}_k) = \prod_{j,m} \mathcal{N}(\mathbf{x}_{kn}|\boldsymbol{\mu}_{jk}^{(m)}, \beta^{-1}\mathbf{I}_D)^{z_{knm}t_{kj}}. \tag{5.10}$$

Finally, prior multinomial distributions were imposed on $\mathbb{Z} = \{\mathcal{Z}_k\}$ and $\mathbb{T} = \{\mathbf{t}_k\}$ variables, normal distributions on $\mathbb{W} = \{\mathbf{W}_j\}$ and $\mathbb{V} = \{\mathbf{v}_k\}$ variables, and assumed conditional independence (see [288] for further details).

To train the joint flow-shape model, I considered estimating the posterior probability of $p(\boldsymbol{\theta}|\mathbb{X}, M, L, J)$, where $\mathbb{X} = \{\mathcal{X}_k\}$ and $\boldsymbol{\theta} = \{\mathbb{Z}, \mathbb{T}, \mathbb{W}, \mathbb{V}\}$. Since this was not analytically tractable, an approximate posterior was sought by maximising a lower bound (LB) on the $p(\mathbb{X}|M, L, J)$ (also known as *model evidence*). This was achieved by assuming a factorised form of posteriors, following the variational Bayesian (VB)

---

[4]The details of statistical model has been given in [288]. A brief overview is provided here for the sake of completeness.
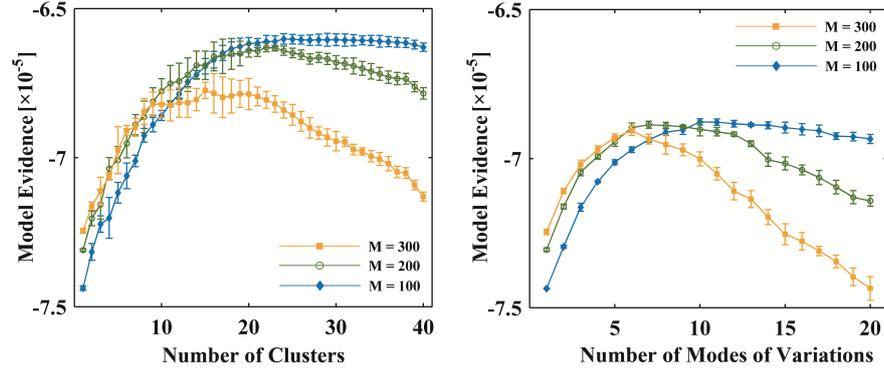
Figure 5.7: Lower bound of model evidence used for optimising the number of clusters J when $L = 1$ (left), and the number of modes of variation per cluster L when $J = 1$ (right). Results shown for different M, the number of sampling points in each cluster.

principal. On the convergence, the approximated posteriors were computed, hence expectations (denoted by $\langle \cdot \rangle$) of latent variables with regard to these variational posteriors became available. For a new test point set $\mathcal{X}_r$, the model projected point set the can be computed using the definition of the expectation: $\langle \hat{\mathbf{x}}_{rn} \rangle = \int \hat{\mathbf{x}}_{rn} p(\hat{\mathbf{x}}_{rn} | \mathcal{X}_r, \mathbb{X}) d\hat{\mathbf{x}}_{rn}$. The latter can be shown to lead into the following result.

$$\langle \hat{\mathbf{x}}_{rn} \rangle = \sum_{j,m} \langle t_{jr} \rangle \langle z_{rnm} \rangle \langle \boldsymbol{\mu}_{jr} \rangle^{(m)} \tag{5.11}$$

To predict TAWSS values from a shape, the trained joint model was first collapsed to a shape-only model, by discarding flow related rows from the $\mathbf{W}_j$ matrices and $\bar{\boldsymbol{\mu}}_j$ vectors. Using this collapsed model, then, VB iterations were performed and the initial posteriors for the corresponding $\mathbf{t}_r$, $\mathcal{Z}_r$ and $\mathbf{v}_r$ variables were obtained. Following this, the $\langle \mathbf{W}_j \rangle$ and $\bar{\boldsymbol{\mu}}_j$ were obtained from the joint model and it was set: $\langle \boldsymbol{\mu}_{jr} \rangle = \langle \mathbf{W}_j \rangle \langle \mathbf{v}_r \rangle + \bar{\boldsymbol{\mu}}_j$. Subsequently, the (5.11) was used to estimate initial TAWSS values. These estimates were then further refined by performing VB iterations (using the joint model), updating $\mathbf{t}_r$, $\mathcal{Z}_r$ and $\mathbf{v}_r$, and interlacing imputations from (5.11). I observed that a convergence was achieved within 10 iterations (< 5 mins).

5.3.2   Results

Model selection and validation

The lower bound of the model evidence, $p(\mathbb{X} \,|\, M, L, J)$, was used as a criterion to select optimal numbers of: 4-dimensional Gaussians (M), PPCA clusters (J), and modes of variations (L) in each cluster. A nine-fold cross validation was then performed using 36 IA shapes and flows to assess the generality and specificity of the model. The scaling
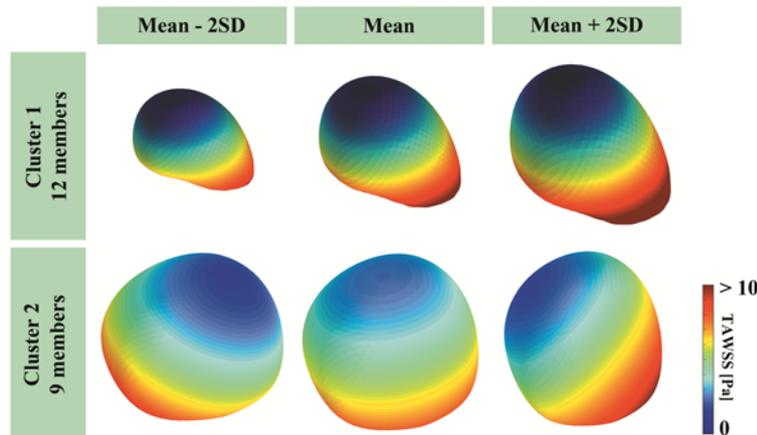
Figure 5.8: Mean and first mode of variation for the two most populated clusters. The mode of the first cluster (top row) represents mainly the IA size, while the mode of the second cluster (bottom row) represents mainly changes in TAWSS patterns.

parameter α, representing the relative weight of shape and TAWSS information in each point set, was then chosen to minimise the generalisation and specificity errors. It was observed that the specificity and generalisation errors was minimised for the default choice of scaling, i.e. $\alpha = 1$. These parameters were used for the flow prediction test.

Fig. 5.7 shows the variation of model evidence with respect to the model parameters (J, L, and M). For each $1 \leq J \leq 40$ and $1 \leq L \leq 20$, I repeated the training for 10 rounds of initialisations. The mean and standard deviation of the model evidences obtained are reported. As shown in Fig. 5.7, maximal model evidence was observed for $J = 23$, $L = 1$, and $M = 100$.

Fig. 5.8 shows the mean shape and the first (and only) mode of variation for the two most populated clusters (the largest cluster having 12 point sets, and the second largest cluster containing 9 point sets). It can be seen that the IA size was the leading mode of the first cluster. However, in the second cluster, the leading mode of variation acted mainly to reorient the TAWSS pattern while the aneurysm shape remained similar. This demonstrated that the modes identified in the model training capture both flow and shape variabilities.

TAWSS Prediction from Shape

To evaluate the ability of the JSM to predict TAWSS for a given test shape, I performed leave-one-out cross-validations. Since CFD model inputs were shown to only affect the TAWSS magnitude and not the distribution of TAWSS on the aneurysm sac [109], Pearson correlation test was used to perform a statistical point-by-point comparison between the model predicted TAWSS and that obtained from the full CFD simulation.

Among a total of 38, the following correlation coefficients were found: $\rho \geq 0.6$ for 18 cases, $0.4 \leq \rho \leq 0.6$ for 13 cases, and $\rho \leq 0.4$ for the rest. It was observed that IAs with worst correlation coefficients fell into clusters with only one aneurysm shape in them. This revealed that the unsuccessful WSS prediction cases were associated with what appeared to be outlier shapes from the training data set; mainly complex multi-bleb aneurysm shapes. Fig. 5.9 shows the model predicted TAWSS compared with the ground truth CFD solutions for the four best and worst cases. For each aneurysm, we report correlation coefficient ρ and the most probable cluster size (MPCS). The latter refers to the size of the cluster that appeared most similar to the test case. It can be seen that the IA with the worst ρ value (bottom row) fell into a cluster with size of three. While others with stronger predictions fell into more populated clusters containing at least 9 point sets in the training data.

5.3.3   Discussion

I presented the first statistical model for complex saccular aneurysms that also predicted TAWSS patterns. The JSM was trained using a database of 38 patient-specific IA geometries and corresponding TAWSS values obtained from CFD simulations. A mixture PPCA model with 23 clusters and one mode of variation in each provided the best fit in terms of model evidence. Only the morphology and TAWSS on the aneurysmal sac were used for training, yet the TAWSS included implicitly information about the configuration of the host vessels. This enabled estimations of TAWSS on the IA wall based on the IA shape alone. Observation of the modes of variation of the largest clusters confirmed that the modes contained information on the variability of both TAWSS and shape.

The large inter-subject variability of IA shapes and their parent vessel configurations means that a sufficiently representative set of training data needs to be acquired. Even when choosing the most populous type of IA (MbifA-type) from the most comprehensive imaging database available to us, I only had 38 patient cases for training. To further study the prediction power of the proposed method, a larger cohort of synthetic aneurysms could however be generated and analyzed as a future work. As a result, the leave-one-out flow prediction test revealed that some IA shapes in the dataset were outlier shapes in which the TAWSS could not be well approximated. These outlier shapes included IAs with multiple daughter aneurysms and/or unusual positioning of the IA with respect to the vasculature. They could be flagged for further CFD analysis based on the size of the cluster in the training data that they were most likely to be part of.

I used IAs as an example of heterogeneous datasets with large variability in both
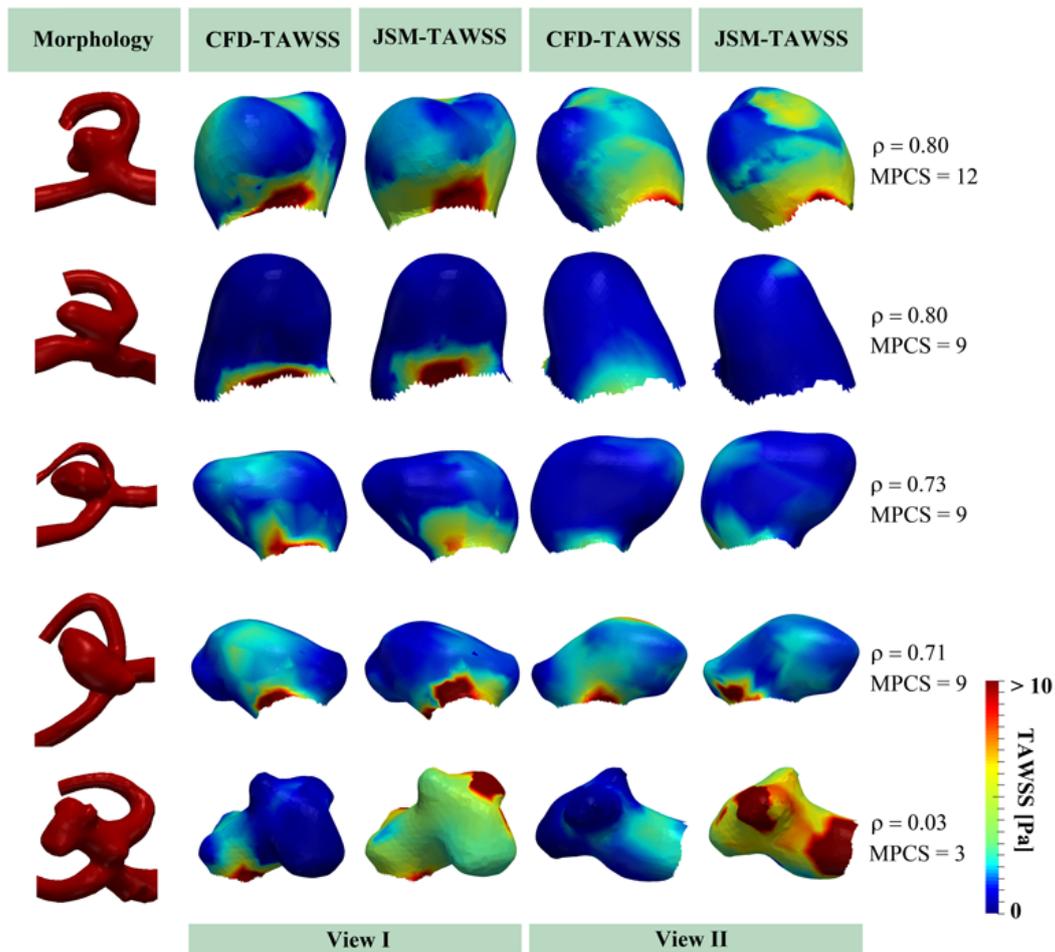
Figure 5.9: Leave-one-out cross validation test for TAWSS estimation. Shown are the four best cases and the worst case (in terms of Pearson's ρ). The JSM accurately predicts flow impingement regions (case 1) and absence of flow (case 2). Case 5 is a complex outlier shape that does not resemble any of the other IA shapes used for training. All correlations significant to $p < 0.001$ except case 5, $p = 0.05$.

flow patterns and shapes. Building the shape model is challenging since there is no straightforward method for establishing point correspondences between heterogeneous shapes. In the proposed method point correspondences are not required. Furthermore, the use of the PPCA mixture model allows outliers to be automatically separated into their own clusters. This is an improvement to single cluster PPCA models, which are known to be sensitive to outliers. The method presented here is therefore general and applicable to a number of other flow prediction scenarios in the presence of complex shape variations.

5.4 Conclusion

As discussed in section 5.1, in *in-silico* clinical trials, a combination of vascular surface models from a real cohort of patients and inter-/intra-subjects flow variability models provide a space of *virtual patients* that extend the cohort beyond what would be available with purely patient-specific data collection. In this chapter, I presented two preliminary studies towards addressing a fully-automatic and computationally inexpensive frameworks for aneurysm flow modelling. In section 5.2, I built an automatic framework to quantify aneurysmal haemodynamics in a range of physiological conditions, i.e., rest versus exercise. In section 5.3, I presented a model to estimate aneurysmal TAWSS directly from its morphology bypassing the computationally expensive process of solving Navier-Stokes equations. I believe that such developments could be further extended and utilised in large-scale *in-silico* clinical trials.

Chapter 6

Conclusions and outlook

6.1   Conclusions

- Measures of quantity and quality of the device-induced clot are important when assessing a FD performance in inducing a stable occlusive clot. Models of post-treatment clot formation should be linked to the purely haemodynamic virtual endovascular treatment workflows to improve them in predicting formation of a stable clot after flow diversion. My review of literature and meta analyses showed that uncertainties emerging from vascular wall distensibility and intra-/inter-subject systemic flow variability affect the aneurysmal haemodynamics. I argued there is a need to extend the current deterministic models of cardiovascular flow with strategies for uncertainty mitigation, uncertainty exploration, and sensitivity reduction.
  – *Chapter 2*

- I developed a data-driven statistical model of ICA flow, which was used to generate a virtual population of waveforms used as inlet boundary conditions in CFD simulations. The utility of such virtual populations lies in *in-silico* trials where the model provided one of the ingredients to successful virtual trials of cerebrovascular interventions, particularly aneurysm flow diversion. I used this virtual population to compute the statistics of the aneurysmal WSS distributions in presence of flow variability. Variations of internal carotid flow waveform had limited effect on the magnitude of time-averaged WSS on the aneurysm sac. In regions where the flow was locally highly multi-directional, WSS directionality and harmonic content were largely affected by the ICA flow waveform. Incorporating the flow variations in classification of the aneurysms based on rupture likelihood, changed the rupture prediction in 4 out of 19 cases, when compared to classifications based on haemodynamic variables predicted from deterministic models. I argued that the effect of systemic blood flow variability should be explicitly considered in CFD-based aneurysm rupture assessment to prevent confounding the conclusions.
  – *Chapter 3*

- I developed a thrombosis model to predict the platelet content distribution in intra-aneurysmal clots formed after flow diversion. The predictions made by the model showed qualitative similarities in the clotting pattern and platelet composition when compared with an in-vitro phantom experiment performed by an independent research group in [1]. I also compared the model predictions against the literature on qualitative thrombotic behaviour in aneurysms treated with FDs.
  – *Chapter 4*

- As a primilary step towards creation of an *in-silico* trial framework for FD assess-

ment, I demonstrated how a fully-automatic framework can be built for aneurysm flow modelling. I used this framework to simulate aneurysmal flow in 54 intracranial aneurysms at rest and during physical activity. The results showed that physiological changes in CBF during increased physical activity may induce fluctuations an order of magnitude higher in certain WSS-related quantities, such as OSI (a 2% mean increase in flow lead to a 124% mean increase in OSI in the virtual cohort). This indicates that OSI may be too sensitive to flow uncertainty to be reliably used for rupture-risk evaluation. A partial recipe to this problem is to use alternative WSS indicators that are robust to flow fluctuations. Specifically, I showed that TransWSS was less sensitive to flow fluctuations than OSI, so that if both indicators are equally informative for the rupture risk then TransWSS should be preferred over OSI.

I also presented the first statistical model for complex saccular aneurysms that also predicted time-averaged WSS patterns. This enabled direct estimation of WSS patterns based on the aneurysm morphology. Such computationally inexpensive statistical models can alleviate the problem of costly CFD simulations and are beneficial for acceleration of large-scale *in-silico* trials. I demonstrated that the predicted WSS patterns can achieve significant similarities to the CFD-based results.
– *Chapter 5*

6.2   Outlook

While each chapter of this thesis is self contained and specific prospects are discussed at the end of each chapter, I summarise of the main possible future directions:

- Previous studies demonstrated the need for prediction of the FD-induced clot bio-chemical composition that is key in characterising stable and unstable thrombus (e.g. [19, 254, 262]). I pointed out that predictions about the success of flow diversion made purely based on aneurysm morphology or post- FD flow alterations cannot capture formation of a stable clot inside aneurysm. Computational prediction of clot stability requires virtual treatment workflows to include models of intra-aneurysmal thrombosis that enable characterisation of the composition of the clot constituents, especially the structural components, i.e., fibrin and platelets. I remark that flow diversion success predictions should be made based on aneurysm morphology, post- FD flow alterations, and biochemical composition of the clot induced by FD. In future FD performance indicators should devised as a combination of these three components to better assess FD performance in terms of inducing a stable clot that closes the aneurysm sac.

- Virtual endovascular treatment workflows are influenced by several sources of uncertainty to be accounted for when interpreting the results of their predictions. In Chapter 2, meta-analyses were performed on three well-known sources of uncertainty, and the uncertainties arising from vascular wall distensibility and inflow waveform variabilities showed effect sizes (Hedge's g) of 0.34, 95% CI [0.22, 0.45], p-value < 0.001, and 0.3, 95% CI [0.08,0.52], p-value = 0.003, respectively. Significance of non-rigid FSI models in future understanding of complex biomechanical processes at the aneurysm wall has also been pointed out by Chung *et al.* [122]. Physiologically realistic FSI models of aneurysms require measuring local variations of wall mechanical properties over highly heterogeneous pathologic aneurysms' wall which is not easily achievable in routine clinical practice. In future, such uncertainties should be addressed by: 1) using more accurate techniques for measuring model input parameters (uncertainty mitigation); 2) considering the propagation of uncertainties from input parameters into the model outputs; and reporting confidence intervals and sensitivities instead of deterministic results (uncertainty exploration); or 3) replacing model outputs with other alternative variables, which carry the same information but are less sensitive to the unknown model parameters (sensitivity reduction). Specifically, more advanced imaging techniques can provide higher quality images of the vascular lumen along with automatic segmentation techniques that do not require a posteriori manual editing and can eliminate some of the geometric uncertainty. Conducting more experimental studies regarding the mechanisms underlying thrombosis, particularly in aneurysms, can reduce model uncertainties in aneurysmal clotting and produce more reliable virtual treatment outcome predictions. However, inherent uncertainties in the systemic flow (and several other model parameters) cannot be eliminated. In such cases, advanced uncertainty quantification techniques [130, 226, 227] can systematically explore the effects of these uncertainties. The concept of personalisation should not be limited to deterministic identification of model parameters at a particular moment in time. Instead, model parameters should be treated as uncertain and/or fluctuating quantities; and uncertainty quantification techniques should propagate those uncertainties through the virtual treatment models in order to produce confidence intervals and sensitivities associated with the model predictions.

- Generation of boundary condition envelopes that capture the entire range of variability of a boundary variable is needed both as part of an *in-silco* trials and to increase the credibility of personalised simulations usually made based on a single set of boundary conditions. In this thesis, I presented statistical models of inter-

nal carotid flow variability (see chapters 2 and 5). These data-driven models are made based on limited number of experimental measurements made on cohorts with homogeneous characteristics, e.g., young and healthy. Data from larger, cross-sectional population studies (e.g. the UK Biobank project [304]) is needed to retrain the models for increased coverage and to achieve actual population-specific, not just cohort-specific models. In future, instead of simple autoregulation models that only consider short-term effects, long-term response to chronic disruptions in cerebral blood flow, such as cardiac disease, should be modelled using a more advanced autoregulation model.

- Quantitative description of the clot composition and morphology is not available in the literaure reporting experimental results on the FD-induced clots (e.g., references [1, 305]). Well-designed *in-vitro* experiments are needed for validation of the thrombosis models based on more quantitative results.

- The time scale of thrombosis models is not representative of the physiological time scale of FD-induced clot formation and aneurysm occlusion, i.e., weeks to months. Anti-coagulants and anti-platelets, both common in the treatment of flow diversion patients, are absent from thrombosis models. More advanced and computationally efficient thromosis models are needed to overcome such limitations. Computer models should consider these chemicals to help clinicians in planning the treatment so they prevent the events like in-stent thrombosis and the possible embolic effects while promoting clot formation in the sac.

- This thesis contributed some of the key components needed for creating an *in-silico* trial framework, particularly for assessing flow diverting stents. Even when all the models and workflows are ready, further developments are needed to streamline them and enjoy a computational framework that enables the large-scale *in-silico* trials. Platforms like `MULTIX`[1] are needed to orchestrate the workflows and enable performing processes on heterogeneous large-scale data. To allow large-scale *in-silico* trials, it is important to consider the computational cost reduction, especially when costly processes like thrombosis simulations are involved. Replacing costly mechanistic models of a *in-silico* trial framework, with phenomenological models, e.g., data-driven models based on machine learning techniques, can be considered to alleviate such issues.

- Intracranial aneurysms phenotypes are highly complex and heterogeneous [38]. Despite the agreements on the mechanisms underlying the aneurysm initiation,

---

[1]See Section 1.1

mechanisms of growth, rupture/stabilisation, and spontaneous/post-treatment healing of the aneurysms are still controversial. Many researchers have investigated the role of haemodynamics in aneurysm progression and rupture. For example, it was shown that WSS differ in ruptured and unruptured aneurysms [241]; and both high and low WSS were correlated with the aneurysm rupture status [38]. Spontaneous aneurysm thrombosis was also shown to occur in regions where blood residence time is high [43, 214]. However, although there is a consensus that intra-aneurysmal haemodynamics do play a role in aneurysm pathophysiology, the mechanisms of the haemodynamic-biologic interactions are not clearly understood.

Whether an aneurysm ruptures or remains stable is thought to depend on the balance between the eutrophic and the destructive changes in the aneurysm wall [38]. Adverse WSS conditions are believed to disrupt the balance and drive aneurysm wall inflammation and degradation. Under healthy conditions, changes in WSS are sensed by the intact endothelium, however, the aneurysm wall is often characterised by dysfunction/loss of endothelium [200] and, thus, impaired mechanotransduction. Cebral *et al.* [306] examined 10 wall tissue samples obtained from different human intracranial aneurysms. Intact endothelium was observed in only 3/10 samples and they did not find any significant difference in the number of aneurysms with intact endothelium in the ruptured and unruptured groups. The study by Cebral *et al.* [306] is the first I know of to compare in-vivo haemodynamics with the histology of human intracranial aneurysms. Cebral *et al.* [306] used sac-averaged WSS to examine the correlations among flow conditions and cellular interactions in the wall, which prevents any general conclusion due to the highly heterogeneous wall structure and aneurysm flow condition. Tissue samples from different regions of the sac and registration of the histologic data with the local haemodynamics should be included in the future studies to better understand the interplay between hemodynamics and the cellular mechanisms of inflammation, and degradation.

In Chapters 3 and 5, I presented models of inter-/intra-subject variability of physiology and studied the uncertainty in the quantification of the aneurysmal WSS. The presented methods are general and not limited to uncertainty quantification of WSS, and thus can be used to investigate the effect of physiological variabilities on other simulation-based haemodynamic measures. In Chapter 4, the thrombosis initiation is not based on any particular biological mechanism at the wall, e.g., wall TF exposure, or blood-borne TF secretion. Instead, flow stasis was assumed as the nexus between all of the complex initiation mechanisms and volumetric

haemodynamic parameters (i.e., residence time and low shear rate) were used to identify regions of flow stasis where the clot can form through a diverse set of initiation mechanisms.

References

[1] K. Gester, I. Lüchtefeld, M. Büsen, S. Sonntag, T. Linde, U. Steinseifer, and G. Cattaneo, "In vitro evaluation of intra-aneurysmal, flow-diverter-induced thrombus formation: a feasibility study," *Am. J. Neuroradiol.*, vol. 37, no. 3, pp. 490–496, 2016.

[2] M. Viceconti, A. Henney, and E. Morley-Fletcher, "In silico clinical trials: how computer simulation will transform the biomedical industry," *Int. J. Clin. Trials*, vol. 3, no. 2, pp. 37–46, 2016.

[3] "The European Medical Technology industry," http://www.medtecheurope.org/sites/default/files/resource_items/files/MEDTECH_FactFigures_ONLINE3.pdf, accessed: 2018-07-29.

[4] "Premarket approval (PMA) database. US Food and Drug Administration." http://www.accessdata.fda.gov/scripts/cdrh/cfdocs/cfpma/pma.cfm, accessed: 2018-07-29.

[5] V. K. Rathi, H. M. Krumholz, F. A. Masoudi, and J. S. Ross, "Characteristics of clinical studies conducted over the total product life cycle of high-risk therapeutic medical devices receiving FDA premarket approval in 2010 and 2011," *J. Amer. Med. Assoc.*, vol. 314, no. 6, pp. 604–612, 2015.

[6] J. Makower, A. Meer, and L. Denend, "FDA impact on us medical technology innovation: a survey of over 200 medical technology companies," *Adv. Med. Technol. Assoc., Washington, DC*, 2010.

[7] Haddad, T., A. Himes, L. Thompson, T. Irony, R. Nair *et al.*, "Incorporation of stochastic engineering models as prior information in Bayesian medical device trials," *J. Biopharm. Stat.*, vol. 27, no. 6, pp. 1089–1103, 2017.

[8] G. J. Rinkel, M. Djibuti, A. Algra, and J. Van Gijn, "Prevalence and risk of rupture of intracranial aneurysms a systematic review," *Stroke*, vol. 29, no. 1, pp. 251–256, 1998.

[9] G. Rajah, S. Narayanan, and L. Rangel-Castilla, "Update on flow diverters for the endovascular management of cerebral aneurysms," *Neurosurg. Focus*, vol. 42, no. 6, p. E2, 2017.

[10] J. Byrne and I. Szikora, "Flow diverters in the management of intracranial aneurysms: a review," *EJMINT*, vol. 1225000057, p. 29, 2012.

[11] K. M. Fargen and B. L. Hoh, "Flow diversion technologies in evolution: a review of the first two generations of flow diversion devices," *World Neurosurg.*, vol. 84, no. 2, pp. 254–256, 2015.

[12] "FDA executive summary. general issues: Meeting to discuss the evaluation of safety and effectiveness of endovascular medical devices intended to treat intracranial aneurysms."

[13] M. Martínez-Galdámez, S. M. Lamin, K. G. Lagios, T. Liebig, E. F. Ciceri, R. Chapot, L. Stockx, S. Chavda, C. Kabbasch, G. Farago *et al.*, "Periprocedural outcomes and early safety with the use of the Pipeline Flex Embolization Device with Shield Technology for unruptured intracranial aneurysms: preliminary results from a prospective clinical study," *J. Neurointerv. Surg.*, pp. neurintsurg–2016, 2017.

[14] J. V. Byrne, R. Beltechi, J. A. Yarnold, J. Birks, and M. Kamran, "Early experience in the treatment of intra-cranial aneurysms by endovascular flow diversion: a multicentre prospective study," *PloS One*, vol. 5, no. 9, p. e12492, 2010.

[15] T. Becske, M. B. Potts, M. Shapiro, D. F. Kallmes, W. Brinjikji, I. Saatci, C. G. McDougall, I. Szikora, G. Lanzino, C. J. Moran *et al.*, "Pipeline for uncoilable or failed aneurysms: 3-year follow-up results," *J. Neurosurg.*, vol. 127, no. 1, pp. 81–88, 2016.

[16] J. Raymond, J.-C. Gentric, T. E. Darsaut, D. Iancu, M. Chagnon, A. Weill, and D. Roy, "Flow diversion in the treatment of aneurysms: a randomized care trial and registry," *J. Neurosurg.*, vol. 127, no. 3, pp. 454–462, 2016.

[17] W. Brinjikji, M. H. Murad, G. Lanzino, H. J. Cloft, and D. F. Kallmes, "Endovascular treatment of intracranial aneurysms with flow diverters: a meta-analysis," *Stroke*, vol. 44, no. 2, pp. 442–447, 2013.

[18] J.-m. Liu, Y. Zhou, Y. Li, T. Li, B. Leng, P. Zhang, G. Liang, Q. Huang, P.-f. Yang, H. Shi *et al.*, "Parent artery reconstruction for large or giant cerebral

aneurysms using the tubridge flow diverter: A multicenter, randomized, controlled clinical trial (PARAT)," *Am. J. Neuroradiol.*, vol. 39, no. 5, pp. 807–816, 2018.

[19] S. Fischer, Z. Vajda, M. Perez, E. Schmid, N. Hopf, H. Bäzner, and H. Henkes, "Pipeline embolization device (PED) for neurovascular reconstruction: initial experience in the treatment of 101 intracranial aneurysms and dissections," *Neuroradiology*, vol. 54, no. 4, pp. 369–382, 2012.

[20] T. Krings, D. M. Mandell, T.-R. Kiehl, S. Geibprasert, M. Tymianski, H. Alvarez, and F.-J. Hans, "Intracranial aneurysms: from vessel wall pathology to therapeutic approach," *Nat. Rev. Neurol.*, vol. 7, no. 10, pp. 547–559, 2011.

[21] R. A. Gabriel, H. Kim, S. Sidney, C. E. McCulloch, V. Singh, S. C. Johnston, N. U. Ko, A. S. Achrol, J. G. Zaroff, and W. L. Young, "Ten-year detection rate of brain arteriovenous malformations in a large, multiethnic, defined population," *Stroke*, vol. 41, no. 1, pp. 21–26, 2010.

[22] J. B. Bederson, I. A. Awad, D. O. Wiebers, D. Piepgras, E. C. Haley, T. Brott, G. Hademenos, D. Chyatte, R. Rosenwasser, and C. Caroselli, "Recommendations for the management of patients with unruptured intracranial aneurysms: a statement for healthcare professionals from the stroke council of the american heart association," *Circ. J.*, vol. 102, no. 18, pp. 2300–2308, 2000.

[23] T. Steiner, S. Juvela, A. Unterberg, C. Jung, M. Forsting, and G. Rinkel, "European stroke organization guidelines for the management of intracranial aneurysms and subarachnoid haemorrhage," *Cerebrovasc. Dis.*, vol. 35, no. 2, pp. 93–112, 2013.

[24] H.-H. Chang, G. R. Duckwiler, D. J. Valentino, and W. C. Chu, "Computer-assisted extraction of intracranial aneurysms on 3d rotational angiograms for computational fluid dynamics modeling," *Med. Phys.*, vol. 36, no. 12, pp. 5612–5621, 2009.

[25] A. Firouzian, R. Manniesing, Z. H. Flach, R. Risselada, F. van Kooten, M. C. Sturkenboom, A. van der Lugt, and W. J. Niessen, "Intracranial aneurysm segmentation in 3d ct angiography: Method and quantitative validation with and without prior noise filtering," *Eur. J. Radiol.*, vol. 79, no. 2, pp. 299–304, 2011.

[26] M. Hernandez and A. F. Frangi, "Non-parametric geodesic active regions: method and evaluation for cerebral aneurysms segmentation in 3dra and cta," *Med. Image Anal.*, vol. 11, no. 3, pp. 224–241, 2007.

[27] P. Bouillot, O. Brina, R. Ouared, H. Yilmaz, M. Farhat, G. Erceg, K.-O. Lovblad, M. I. Vargas, Z. Kulcsar, and V. M. Pereira, "Geometrical deployment for braided stent," *Med. Image Anal.*, vol. 30, pp. 85–94, 2016.

[28] I. Larrabide, M. Kim, L. Augsburger, M. C. Villa-Uriol, D. Rüfenacht, and A. F. Frangi, "Fast virtual deployment of self-expandable stents: method and in vitro evaluation for intracranial aneurysmal stenting," *Med. Image Anal.*, vol. 16, no. 3, pp. 721–730, 2012.

[29] D. Ma, G. F. Dargush, S. K. Natarajan, E. I. Levy, A. H. Siddiqui, and H. Meng, "Computer modeling of deployment and mechanical expansion of neurovascular flow diverter in patient-specific intracranial aneurysms," *J. Biomech.*, vol. 45, no. 13, pp. 2256–2263, 2012.

[30] H. G. Morales, I. Larrabide, M. L. Aguilar, A. J. Geers, J. M. Macho, L. San Roman, and A. F. Frangi, "Comparison of two techniques of endovascular coil modeling in cerebral aneurysms using CFD," in *IEEE Int. Sympos. Biomed. Imaging (ISBI)*. IEEE, 2012, Conference Proceedings, pp. 1216–1219.

[31] J. R. Cebral, M. A. Castro, S. Appanaboyina, C. M. Putman, D. Millan, and A. F. Frangi, "Efficient pipeline for image-based patient-specific analysis of cerebral aneurysm hemodynamics: technique and sensitivity," *IEEE T. Med. Imaging*, vol. 24, no. 4, pp. 457–467, 2005.

[32] M. Villa-Uriol, I. Larrabide, J. Pozo, M. Kim, M. De Craene, O. Camara, C. Zhang, A. Geers, H. Bogunović, and H. Morales, *Cerebral aneurysms: a patient-specific and image-based management pipeline*. Springer, 2011, pp. 327–349.

[33] M.-C. Villa-Uriol, I. Larrabide, J. Pozo, M. Kim, O. Camara, M. De Craene, C. Zhang, A. Geers, H. Morales, and H. Bogunović, "Toward integrated management of cerebral aneurysms," *Philos. T. Roy. Soc. A*, vol. 368, no. 1921, pp. 2961–2982, 2010.

[34] B. P. Walcott, C. Reinshagen, C. J. Stapleton, O. Choudhri, V. Rayz, D. Saloner, and M. T. Lawton, "Predictive modeling and in vivo assessment of cerebral blood flow in the management of complex cerebral aneurysms," *J. Cerebr. Blood F. Met.*, vol. 36, no. 6, pp. 998–1003, 2016.

[35] P. Bhogal, M. A. Pérez, O. Ganslandt, H. Bäzner, H. Henkes, and S. Fischer, "Treatment of posterior circulation non-saccular aneurysms with flow diverters: a single-center experience and review of 56 patients," *J. Neurointerv. Surg.*,

pp. Published Online First: 11 November 2016, doi: 10.1136/neurintsurg–2016–012 781, 2016.

[36] M. Shapiro, T. Becske, H. A. Riina, E. Raz, D. Zumofen, and P. K. Nelson, "Non-saccular vertebrobasilar aneurysms and dolichoectasia: a systematic literature review," *J. Neurointerv. Surg.*, vol. 6, no. 5, pp. 389–393, 2014.

[37] C. Iosif, S. Ponsonnard, A. Roussie, S. Saleme, P. Carles, S. Ponomarjova, E. Pedrolo-Silveira, G. Mendes, E. Waihrich, and C. Couquet, "Jailed artery ostia modifications after flow-diverting stent deployment at arterial bifurcations: A scanning electron microscopy translational study," *Neurosurgery*, vol. 79, no. 3, pp. 473–480, 2016.

[38] H. Meng, V. Tutino, J. Xiang, and A. Siddiqui, "High wss or low wss? complex interactions of hemodynamics with intracranial aneurysm initiation, growth, and rupture: toward a unifying hypothesis," *Am. J. Neuroradiol.*, vol. 35, no. 7, pp. 1254–1262, 2014.

[39] Z. Kulcsár, E. Houdart, A. Bonafe, G. Parker, J. Millar, A. Goddard, S. Renowden, G. Gal, B. Turowski, and K. Mitchell, "Intra-aneurysmal thrombosis as a possible cause of delayed aneurysm rupture after flow-diversion treatment," *Am. J. Neuroradiol.*, vol. 32, no. 1, pp. 20–25, 2011.

[40] J. Xiang, D. Ma, K. V. Snyder, E. I. Levy, A. H. Siddiqui, and H. Meng, "Increasing flow diversion for cerebral aneurysm treatment using a single flow diverter," *Neurosurgery*, vol. 75, no. 3, pp. 286–294, 2014.

[41] D. R. de Sousa, C. Vallecilla, K. Chodzynski, R. C. Jerez, O. Malaspinas, O. F. Eker, R. Ouared, L. Vanhamme, A. Legrand, and B. Chopard, "Determination of a shear rate threshold for thrombus formation in intracranial aneurysms," *J. Neurointerv. Surg.*, pp. 853–858, 2015.

[42] R. Ouared, B. Chopard, B. Stahl, D. A. Rüfenacht, H. Yilmaz, and G. Courbebaisse, "Thrombosis modeling in intracranial aneurysms: a lattice boltzmann numerical algorithm," *Comput. Phys. Commun.*, vol. 179, no. 1, pp. 128–131, 2008.

[43] V. Rayz, L. Boussel, M. Lawton, G. Acevedo-Bolton, L. Ge, W. Young, R. Higashida, and D. Saloner, "Numerical modeling of the flow in intracranial aneurysms: prediction of regions prone to thrombus formation," *Ann. Biomed. Eng.*, vol. 36, no. 11, pp. 1793–1804, 2008.

[44] A. Bedekar, K. Pant, Y. Ventikos, and S. Sundaram, "A computational model combining vascular biology and haemodynamics for thrombosis prediction in anatomically accurate cerebral aneurysms," *Food Bioprod. Process.*, vol. 83, no. 2, pp. 118–126, 2005.

[45] M. Ngoepe and Y. Ventikos, "Computational modelling of clot development in patient-specific cerebral aneurysm cases," *J. Thromb. Haemost.*, vol. 14, no. 2, pp. 262–272, 2016.

[46] D. F. Kallmes, "Point: CFD—computational fluid dynamics or confounding factor dissemination," *Am. J. Neuroradiol.*, vol. 33, no. 3, pp. 395–396, 2012.

[47] M. Borenstein, L. V. Hedges, J. Higgins, and H. R. Rothstein, *Introduction to meta-analysis.* Wiley Online Library, 2009.

[48] E. T. Chappell, F. C. Moure, and M. C. Good, "Comparison of computed tomographic angiography with digital subtraction angiography in the diagnosis of cerebral aneurysms: a meta-analysis," *Neurosurgery*, vol. 52, no. 3, pp. 624–631, 2003.

[49] A. M. Sailer, B. A. Wagemans, P. J. Nelemans, R. de Graaf, and W. H. van Zwam, "Diagnosing intracranial aneurysms with mr angiography systematic review and meta-analysis," *Stroke*, vol. 45, no. 1, pp. 119–126, 2014.

[50] W. J. van Rooij, M. Sprengers, A. N. de Gast, J. Peluso, and M. Sluzewski, "3d rotational angiography: the new gold standard in the detection of additional intracranial aneurysms," *Am. J. Neuroradiol.*, vol. 29, no. 5, pp. 976–979, 2008.

[51] M. Piotin, P. Gailloud, L. Bidaut, S. Mandai, M. Muster, J. Moret, and D. Rüfenacht, "Ct angiography, mr angiography and rotational digital subtraction angiography for volumetric assessment of intracranial aneurysms. an experimental study," *Neuroradiology*, vol. 45, no. 6, pp. 404–409, 2003.

[52] M. Ramachandran, R. Retarekar, R. E. Harbaugh, D. Hasan, B. Policeni, R. Rosenwasser, C. Ogilvy, and M. L. Raghavan, "Sensitivity of quantified intracranial aneurysm geometry to imaging modality," *Cardiovasc. Eng. Techn.*, vol. 4, no. 1, pp. 75–86, 2013.

[53] R. Anxionnat, S. Bracard, X. Ducrocq, Y. Trousset, L. Launay, E. Kerrien, M. Braun, R. Vaillant, F. Scomazzoni, and A. Lebedinsky, "Intracranial aneurysms: clinical value of 3d digital subtraction angiography in the therapeutic decision and endovascular treatment," *Radiology*, vol. 218, no. 3, pp. 799–808, 2001.

[54] U. Missler, C. Hundt, M. Wiesmann, T. Mayer, and H. Brückmann, "Three-dimensional reconstructed rotational digital subtraction angiography in planning treatment of intracranial aneurysms," *Eur. Radiol.*, vol. 10, no. 4, pp. 564–568, 2000.

[55] S. Tanoue, H. Kiyosue, H. Kenai, T. Nakamura, M. Yamashita, and H. Mori, "Three-dimensional reconstructed images after rotational angiography in the evaluation of intracranial aneurysms: surgical correlation," *Neurosurgery*, vol. 47, no. 4, pp. 866–871, 2000.

[56] M. A. Castro, C. M. Putman, and J. R. Cebral, "Patient-specific computational modeling of cerebral aneurysms with multiple avenues of flow from 3d rotational angiography images," *Acad. Radiol.*, vol. 13, no. 7, pp. 811–821, 2006.

[57] A. Geers, I. Larrabide, A. G. Radaelli, H. Bogunovic, M. Kim, H. G. van Andel, C. Majoie, E. VanBavel, and A. Frangi, "Patient-specific computational hemodynamics of intracranial aneurysms from 3d rotational angiography and ct angiography: an in vivo reproducibility study," *Am. J. Neuroradiol.*, vol. 32, no. 3, pp. 581–586, 2011.

[58] H. Bogunović, J. M. Pozo, M. C. Villa-Uriol, C. B. Majoie, R. van den Berg, H. A. G. van Andel, J. M. Macho, J. Blasco, L. San Román, and A. F. Frangi, "Automated segmentation of cerebral vasculature with aneurysms in 3dra and tof-mra using geodesic active regions: an evaluation study," *Med. Phys.*, vol. 38, no. 1, pp. 210–222, 2011.

[59] D. A. Steinman, J. S. Milner, C. J. Norley, S. P. Lownie, and D. W. Holdsworth, "Image-based computational simulation of flow dynamics in a giant intracranial aneurysm," *Am. J. Neuroradiol.*, vol. 24, no. 4, pp. 559–566, 2003.

[60] Y. Sen, Y. Qian, Y. Zhang, and M. Morgan, "A comparison of medical image segmentation methods for cerebral aneurysm computational hemodynamics," in *2011 Int. Conf. Biomed. Eng. Inform. (BMEI)*, vol. 2. IEEE, 2011, Conference Proceedings, pp. 901–904.

[61] M. Castro, C. Putman, and J. Cebral, "Computational fluid dynamics modeling of intracranial aneurysms: effects of parent artery segmentation on intra-aneurysmal hemodynamics," *Am. J. Neuroradiol.*, vol. 27, no. 8, pp. 1703–1709, 2006.

[62] A. M. Gambaruto, J. Janela, A. Moura, and A. Sequeira, "Sensitivity of hemo-dynamics in a patient specific cerebral aneurysm to vascular geometry and blood rheology," *Math. Biosci. Eng.*, vol. 8, no. 2, pp. 409–423, 2011.

[63] A. J. Geers, I. Larrabide, A. Radaelli, H. Bogunovic, H. Van Andel, C. Majoie, and A. F. Frangi, "Reproducibility of image-based computational hemodynamics in intracranial aneurysms: comparison of cta and 3dra," in *IEEE Int. Sympos. Biomed. Imaging (ISBI)*. IEEE, 2009, Conference Proceedings, pp. 610–613.

[64] M. Spiegel, T. Redel, Y. Zhang, T. Struffert, J. Hornegger, R. G. Grossman, A. Doerfler, and C. Karmonik, "Tetrahedral and polyhedral mesh evaluation for cerebral hemodynamic simulation–a comparison," in *2009 Annu. Int. Conf. IEEE Eng. Med. Biol. Soc. (EMBC)*. Citeseer, 2009, Conference Proceedings, pp. 2787–2790.

[65] C. A. Taylor and D. A. Steinman, "Image-based modeling of blood flow and vessel wall dynamics: applications, methods and future directions," *Ann. Biomed. Eng.*, vol. 38, no. 3, pp. 1188–1203, 2010.

[66] G. Janiga, P. Berg, O. Beuing, M. Neugebauer, R. Gasteiger, B. Preim, G. Rose, M. Skalej, and D. Thévenin, "Recommendations for accurate numerical blood flow simulations of stented intracranial aneurysms," *Biomed. Eng.*, vol. 58, no. 3, pp. 303–314, 2013.

[67] S. Hodis, S. Uthamaraj, A. L. Smith, K. D. Dennis, D. F. Kallmes, and D. Dragomir-Daescu, "Grid convergence errors in hemodynamic solution of patient-specific cerebral aneurysms," *J. Biomech.*, vol. 45, no. 16, pp. 2907–2913, 2012.

[68] G. R. Stuhne and D. A. Steinman, "Finite-element modeling of the hemody-namics of stented aneurysms," *J. Biomech. Eng. T. ASME*, vol. 126, no. 3, pp. 382–387, 2004.

[69] I. Larrabide, A. J. Geers, H. G. Morales, P. Bijlenga, and D. A. Rüfenacht, "Change in aneurysmal flow pulsatility after flow diverter treatment," *Comput. Med. Imag. Grap.*, vol. 50, pp. 2–8, 2016.

[70] G. Janiga, C. Rössl, M. Skalej, and D. Thévenin, "Realistic virtual intracranial stenting and computational fluid dynamics for treatment analysis," *J. Biomech.*, vol. 46, no. 1, pp. 7–12, 2013.

[71] R. Löhner, *Applied computational fluid dynamics techniques: an introduction based on finite element methods*. John Wiley & Sons, 2008.

[72] J. R. Cebral and R. Lohner, "Efficient simulation of blood flow past complex endovascular devices using an adaptive embedding technique," *IEEE T. Med. Imaging*, vol. 24, no. 4, pp. 468–476, 2005.

[73] S. Appanaboyina, F. Mut, R. Löhner, C. Putman, and J. Cebral, "Computational fluid dynamics of stented intracranial aneurysms using adaptive embedded unstructured grids," *Int. J. Numer. Meth. Fl.*, vol. 57, no. 5, pp. 475–493, 2008.

[74] M. D. Ford, N. Alperin, S. H. Lee, D. W. Holdsworth, and D. A. Steinman, "Characterization of volumetric flow rate waveforms in the normal internal carotid and vertebral arteries," *Physiol. Meas.*, vol. 26, no. 4, p. 477, 2005.

[75] M. N. Gwilliam, N. Hoggard, D. Capener, P. Singh, A. Marzo, P. K. Verma, and I. D. Wilkinson, "Mr derived volumetric flow rate waveforms at locations within the common carotid, internal carotid, and basilar arteries," *J. Cerebr. Blood F. Met.*, vol. 29, no. 12, pp. 1975–1982, 2009.

[76] Y. Hoi, B. A. Wasserman, Y. J. Xie, S. S. Najjar, L. Ferruci, E. G. Lakatta, G. Gerstenblith, and D. A. Steinman, "Characterization of volumetric flow rate waveforms at the carotid bifurcations of older adults," *Physiol. Meas.*, vol. 31, no. 3, p. 291, 2010.

[77] W. Nichols, M. O'Rourke, and C. Vlachopoulos, *McDonald's blood flow in arteries: theoretical, experimental and clinical principles*. CRC Press, 2011.

[78] Y. Shi, P. Lawford, and R. Hose, "Review of zero-d and 1-d models of blood flow in the cardiovascular system," *Biomed. Eng. Online*, vol. 10, no. 1, p. 33, 2011.

[79] L. Grinberg and G. E. Karniadakis, "Outflow boundary conditions for arterial networks with multiple outlets," *Ann. Biomed. Eng.*, vol. 36(9), pp. 1496–1514, 2008.

[80] M. S. Olufsen, A. Nadim, and L. A. Lipsitz, "Dynamics of cerebral blood flow regulation explained using a lumped parameter model," *Am. J. Physiol. Reg. I.*, vol. 282, no. 2, pp. R611–R622, 2002.

[81] L. Formaggia, D. Lamponi, and A. Quarteroni, "One-dimensional models for blood flow in arteries," *J. Eng. Math.*, vol. 47, no. 3-4, pp. 251–276, 2003.

[82] P. Reymond, F. Merenda, F. Perren, D. Rüfenacht, and N. Stergiopulos, "Validation of a one-dimensional model of the systemic arterial tree," *Am. J. Physiol. Heart C.*, vol. 297, no. 1, pp. H208–H222, 2009.

[83] P. Reymond, Y. Bohraus, F. Perren, F. Lazeyras, and N. Stergiopulos, "Validation of a patient-specific one-dimensional model of the systemic arterial tree," *Am. J. Physiol. Heart C.*, vol. 301, no. 3, pp. H1173–H1182, 2011.

[84] P. Blanco, R. Feijóo, and S. Urquiza, "A unified variational approach for coupling 3d–1d models and its blood flow applications," *Comput. Meth. Appl. M.*, vol. 196, no. 41, pp. 4391–4410, 2007.

[85] L. Dempere-Marco, E. Oubel, M. Castro, C. Putman, A. Frangi, and J. Cebral, *CFD analysis incorporating the influence of wall motion: application to intracranial aneurysms.* Springer, 2006, pp. 438–445.

[86] R. Torii, M. Oshima, T. Kobayashi, K. Takagi, and T. E. Tezduyar, "Fluid–structure interaction modeling of aneurysmal conditions with high and normal blood pressures," *Comput. Mech.*, vol. 38, no. 4-5, pp. 482–490, 2006.

[87] R. Torii, M. Oshima, T. Kobayashi, K. Takagi, and T. E. Tezduyar, "Fluid–structure interaction modeling of a patient-specific cerebral aneurysm: influence of structural modeling," *Comput. Mech.*, vol. 43, no. 1, pp. 151–159, 2008.

[88] A. Radaelli, L. Augsburger, J. Cebral, M. Ohta, D. Rüfenacht, R. Balossino, G. Benndorf, D. Hose, A. Marzo, and R. Metcalfe, "Reproducibility of haemodynamical simulations in a subject-specific stented aneurysm model—a report on the virtual intracranial stenting challenge 2007," *J. Biomech.*, vol. 41, no. 10, pp. 2069–2081, 2008.

[89] D. A. Steinman, Y. Hoi, P. Fahy, L. Morris, M. T. Walsh, N. Aristokleous, A. S. Anayiotos, Y. Papaharilaou, A. Arzani, and S. C. Shadden, "Variability of computational fluid dynamics solutions for pressure and flow in a giant aneurysm: the asme 2012 summer bioengineering conference CFD challenge," *J. Biomech. Eng. T. ASME*, vol. 135, no. 2, p. 021016, 2013.

[90] D. G. Martin, E. W. Ferguson, S. Wigutoff, T. Gawne, and E. B. Schoomaker, "Blood viscosity responses to maximal exercise in endurance-trained and sedentary female subjects," *J. Appl. Physiol.*, vol. 59, no. 2, pp. 348–353, 1985.

[91] M. J. Kool, A. P. Hoeks, H. A. S. Boudier, R. S. Reneman, and L. M. Van Bortel, "Short and long-term effects of smoking on arterial wall properties in habitual smokers," *J. Am. Coll. Cardiol.*, vol. 22, no. 7, pp. 1881–1886, 1993.

[92] J. Bernsdorf and D. Wang, "Non-newtonian blood flow simulation in cerebral aneurysms," *Comput. Math. Appl.*, vol. 58, no. 5, pp. 1024–1029, 2009.

[93] A. Valencia, A. Zarate, M. Galvez, and L. Badilla, "Non-newtonian blood flow dynamics in a right internal carotid artery with a saccular aneurysm," *Int. J. Numer. Meth. Fl.*, vol. 50, no. 6, pp. 751–764, 2006.

[94] J. Xiang, M. Tremmel, J. Kolega, E. I. Levy, S. K. Natarajan, and H. Meng, "Newtonian viscosity model could overestimate wall shear stress in intracranial aneurysm domes and underestimate rupture risk," *J. Neurointerv. Surg.*, vol. 4, no. 5, pp. 351–357, 2011.

[95] J. Mazumdar, *Biofluid mechanics.* World Scientific, 2015.

[96] M. A. Castro, M. C. A. Olivares, C. M. Putman, and J. R. Cebral, "Unsteady wall shear stress analysis from image-based computational fluid dynamic aneurysm models under newtonian and casson rheological models," *Med. Biol. Eng. Comput.*, vol. 52, no. 10, pp. 827–839, 2014.

[97] C. Fisher and J. S. Rossmann, "Effect of non-newtonian behavior on hemodynamics of cerebral aneurysms," *J. Biomech. Eng. T. ASME*, vol. 131, no. 9, p. 091004, 2009.

[98] H. G. Morales, I. Larrabide, A. J. Geers, M. L. Aguilar, and A. F. Frangi, "Newtonian and non-newtonian blood flow in coiled cerebral aneurysms," *J. Biomech.*, vol. 46, no. 13, pp. 2158–2164, 2013.

[99] C. Huang, Z. Chai, and B. Shi, "Non-newtonian effect on hemodynamic characteristics of blood flow in stented cerebral aneurysm," *Commun. Comput. Phys.*, vol. 13, no. 03, pp. 916–928, 2013.

[100] M. Cavazzuti, M. Atherton, M. Collins, and G. Barozzi, "Beyond the virtual intracranial stenting challenge 2007: non-newtonian and flow pulsatility effects," *J. Biomech.*, vol. 43, no. 13, pp. 2645–2647, 2010.

[101] M. Cavazzuti, M. Atherton, M. Collins, and G. Barozzi, "Non-newtonian and flow pulsatility effects in simulation models of a stented intracranial aneurysm," *P. I. Mech. Eng. H*, vol. 225, no. 6, pp. 597–609, 2011.

[102] J. Cohen, "A power primer," *Psychol. Bull.*, vol. 112, no. 1, pp. 155–159, 1992.

[103] I. Jansen, J. Schneiders, W. Potters, P. van Ooij, R. van den Berg, E. van Bavel, H. Marquering, and C. Majoie, "Generalized versus patient-specific inflow boundary conditions in computational fluid dynamics simulations of cerebral aneurysmal hemodynamics," *Am. J. Neuroradiol.*, vol. 35, no. 8, pp. 1543–1548, 2014.

[104] A. Marzo, P. Singh, I. Larrabide, A. Radaelli, S. Coley, M. Gwilliam, I. D. Wilkinson, P. Lawford, P. Reymond, and U. Patel, "Computational hemodynamics in cerebral aneurysms: the effects of modeled versus measured boundary conditions," *Ann. Biomed. Eng.*, vol. 39, no. 2, pp. 884–896, 2011.

[105] P. M. McGah, M. R. Levitt, M. C. Barbour, R. P. Morton, J. D. Nerva, P. D. Mourad, B. V. Ghodke, D. K. Hallam, L. N. Sekhar, and L. J. Kim, "Accuracy of computational cerebral aneurysm hemodynamics using patient-specific endovascular measurements," *Ann. Biomed. Eng.*, vol. 42, no. 3, pp. 503–514, 2014.

[106] C. Karmonik, C. Yen, O. Diaz, R. Klucznik, R. G. Grossman, and G. Benndorf, "Temporal variations of wall shear stress parameters in intracranial aneurysms—importance of patient-specific inflow waveforms for CFD calculations," *Acta Neurochir.*, vol. 152, no. 8, pp. 1391–1398, 2010.

[107] T. Bowker, P. Watton, P. Summers, J. Byrne, and Y. Ventikos, "Rest versus exercise hemodynamics for middle cerebral artery aneurysms: a computational study," *Am. J. Neuroradiol.*, vol. 31, no. 2, pp. 317–323, 2010.

[108] A. Geers, I. Larrabide, H. Morales, and A. Frangi, "Approximating hemodynamics of cerebral aneurysms with steady flow simulations," *J. Biomech.*, vol. 47, no. 1, pp. 178–185, 2014.

[109] J. Xiang, A. Siddiqui, and H. Meng, "The effect of inlet waveforms on computational hemodynamics of patient-specific intracranial aneurysms," *J. Biomech.*, vol. 47, no. 16, pp. 3882–3890, 2014.

[110] A. Sarrami-Foroushani, T. Lassila, A. Gooya, A. J. Geers, and A. F. Frangi, "Uncertainty quantification of wall shear stress in intracranial aneurysms using a data-driven statistical model of systemic blood flow variability," *J. Biomech.*, vol. 49, no. 16, p. 3815–3823, 2016.

[111] H. G. Morales and O. Bonnefous, "Unraveling the relationship between arterial flow and intra-aneurysmal hemodynamics," *J. Biomech.*, vol. 48, no. 4, pp. 585–591, 2015.

[112] K. Valen-Sendstad, M. Piccinelli, R. KrishnankuttyRema, and D. A. Steinman, "Estimation of inlet flow rates for image-based aneurysm CFD models: where and how to begin?" *Ann. Biomed. Eng.*, vol. 43, no. 6, pp. 1422–1431, 2015.

[113] J. Cebral, M. Castro, C. Putman, and N. Alperin, "Flow–area relationship in internal carotid and vertebral arteries," *Physiol. Meas.*, vol. 29, no. 5, pp. 585–594, 2008.

[114] V. Pereira, O. Brina, A. M. Gonzales, A. Narata, P. Bijlenga, K. Schaller, K. Lovblad, and R. Ouared, "Evaluation of the influence of inlet boundary conditions on computational fluid dynamics for intracranial aneurysms: a virtual experiment," *J. Biomech.*, vol. 46, no. 9, pp. 1531–1539, 2013.

[115] S. Hodis, S. Kargar, D. F. Kallmes, and D. Dragomir-Daescu, "Artery length sensitivity in patient-specific cerebral aneurysm simulations," *Am. J. Neuroradiol.*, vol. 36, no. 4, pp. 737–743, 2015.

[116] P. Van Ooij, J. Schneiders, H. Marquering, C. Majoie, E. van Bavel, and A. Nederveen, "3d cine phase-contrast mri at 3t in intracranial aneurysms compared with patient-specific computational fluid dynamics," *Am. J. Neuroradiol.*, vol. 34, no. 9, pp. 1785–1791, 2013.

[117] J. Humphrey and C. Taylor, "Intracranial and abdominal aortic aneurysms: similarities, differences, and need for a new class of computational models," *Annu. Rev. Biomed. Eng.*, vol. 10, p. 221, 2008.

[118] R. Torii, M. Oshima, T. Kobayashi, K. Takagi, and T. E. Tezduyar, "Fluid–structure interaction modeling of blood flow and cerebral aneurysm: significance of artery and aneurysm shapes," *Comput. Meth. Appl. M.*, vol. 198, no. 45, pp. 3613–3621, 2009.

[119] K. Takizawa, T. Brummer, T. E. Tezduyar, and P. R. Chen, "A comparative study based on patient-specific fluid-structure interaction modeling of cerebral aneurysms," *J. Appl. Mech.*, vol. 79, no. 1, p. 010908, 2012.

[120] Y. Bazilevs, M.-C. Hsu, Y. Zhang, W. Wang, X. Liang, T. Kvamsdal, R. Brekken, and J. Isaksen, "A fully-coupled fluid-structure interaction simulation of cerebral aneurysms," *Comput. Mech.*, vol. 46, no. 1, pp. 3–16, 2010.

[121] Y. Bazilevs, M.-C. Hsu, Y. Zhang, W. Wang, T. Kvamsdal, S. Hentschel, and J. Isaksen, "Computational vascular fluid–structure interaction: methodology and application to cerebral aneurysms," *Biomech. Model. Mechan.*, vol. 9, no. 4, pp. 481–498, 2010.

[122] B. Chung and J. R. Cebral, "CFD for evaluation and treatment planning of aneurysms: review of proposed clinical uses and their challenges," *Ann. Biomed. Eng.*, vol. 43, no. 1, pp. 122–138, 2015.

[123] R. Torii, M. Oshima, T. Kobayashi, K. Takagi, and T. E. Tezduyar, "Influence of wall thickness on fluid–structure interaction computations of cerebral aneurysms," *Int. J. Numer. Meth. Bio.*, vol. 26, no. 3-4, pp. 336–347, 2010.

[124] H. G. Morales and O. Bonnefous, "Peak systolic or maximum intra-aneurysmal hemodynamic condition? implications on normalized flow variables," *J. Biomech.*, vol. 47, no. 10, pp. 2362–2370, 2014.

[125] Y. Mohamied, E. M. Rowland, E. L. Bailey, S. J. Sherwin, M. A. Schwartz, and P. D. Weinberg, "Change of direction in the biomechanics of atherosclerosis," *Ann. Biomed. Eng.*, vol. 43, no. 1, pp. 16–25, 2015.

[126] C. Wang, B. M. Baker, C. S. Chen, and M. A. Schwartz, "Endothelial cell sensing of flow direction," *Arterioscl. Throm. Vas.*, vol. 33, no. 9, pp. 2130–2136, 2013.

[127] J. Ando and K. Yamamoto, "Vascular mechanobiology endothelial cell responses to fluid shear stress," *Circ. J.*, vol. 73, no. 11, pp. 1983–1992, 2009.

[128] K. Wu, MD and P. Thiagarajan, MD, "Role of endothelium in thrombosis and hemostasis," *Annu. Rev. Med.*, vol. 47, no. 1, pp. 315–331, 1996.

[129] S. Ramalho, A. Moura, A. Gambaruto, and A. Sequeira, "Sensitivity to outflow boundary conditions and level of geometry description for a cerebral aneurysm," *Int. J. Numer. Meth. Bio.*, vol. 28, no. 6-7, pp. 697–713, 2012.

[130] D. Schiavazzi, G. Arbia, C. Baker, A. M. Hlavacek, T.-Y. Hsia, A. Marsden, and I. Vignon-Clementel, "Uncertainty quantification in virtual surgery hemodynamics predictions for single ventricle palliation," *Int. J. Numer. Meth. Bio.*, vol. 32, no. 3, p. e02737, 2015.

[131] G. Troianowski, C. A. Taylor, J. A. Feinstein, and I. E. Vignon-Clementel, "Three-dimensional simulations in glenn patients: clinically based boundary conditions, hemodynamic results and sensitivity to input data," *Ann. Biomed. Eng.*, vol. 133, no. 11, p. 111006, 2011.

[132] G. Janiga, P. Berg, S. Sugiyama, K. Kono, and D. Steinman, "The computational fluid dynamics rupture challenge 2013—phase i: prediction of rupture status in intracranial aneurysms," *Am. J. Neuroradiol.*, vol. 36, no. 3, pp. 530–536, 2015.

[133] K. Valen-Sendstad, M. Piccinelli, and D. A. Steinman, "High-resolution computational fluid dynamics detects flow instabilities in the carotid siphon: implications for aneurysm initiation and rupture?" *J. Biomech.*, vol. 47, no. 12, pp. 3210–3216, 2014.

[134] K. Valen-Sendstad and D. Steinman, "Mind the gap: impact of computational fluid dynamics solution strategy on prediction of intracranial aneurysm hemodynamics and rupture status indicators," *Am. J. Neuroradiol.*, vol. 35, no. 3, pp. 536–543, 2014.

[135] R. E. Feaver, B. D. Gelfand, and B. R. Blackman, "Human haemodynamic frequency harmonics regulate the inflammatory phenotype of vascular endothelial cells," *Nat. Commun.*, vol. 4, p. 1525, 2013.

[136] M. H. Babiker, B. Chong, L. F. Gonzalez, S. Cheema, and D. H. Frakes, "Finite element modeling of embolic coil deployment: multifactor characterization of treatment effects on cerebral aneurysm hemodynamics," *J. Biomech.*, vol. 46, no. 16, pp. 2809–2816, 2013.

[137] J. Dequidt, M. Marchal, C. Duriez, E. Kerien, and S. Cotin, "Interactive simulation of embolization coils: modeling and experimental validation," in *Med. Image Comput. Comput. Assist. Interv. – MICCAI 2008*. Springer, 2008, Conference Proceedings, pp. 695–702.

[138] J. Dequidt, C. Duriez, S. Cotin, and E. Kerrien, "Towards interactive planning of coil embolization in brain aneurysms," in *Med. Image Comput. Comput. Assist. Interv. – MICCAI 2009*. Springer, 2009, Conference Proceedings, pp. 377–385.

[139] Y. Wei, C. Duriez, E. Kerrien, J. Allard, J. Dequidt, and S. Cotin, *A (Near) real-time simulation method of aneurysm coil embolization*. InTech Open Access Publisher, 2012, pp. 223–248.

[140] K. S. Cha, E. Balaras, B. B. Lieber, C. Sadasivan, and A. K. Wakhloo, "Modeling the interaction of coils with the local blood flow after coil embolization of intracranial aneurysms," *J. Biomech. Eng. T. ASME*, vol. 129, no. 6, pp. 873–879, 2007.

[141] C. Groden, J. Laudan, S. Gatchell, and H. Zeumer, "Three-dimensional pulsatile flow simulation before and after endovascular coil embolization of a terminal cerebral aneurysm," *J. Cerebr. Blood F. Met.*, vol. 21, no. 12, pp. 1464–1471, 2001.

[142] L.-D. Jou, D. Saloner, and R. Higashida, "Determining intra-aneurysmal flow for coiled cerebral aneurysms with digital fluoroscopy," *Biomed. Eng. App. Bas. C.*, vol. 16, no. 02, pp. 43–48, 2004.

[143] N. M. Kakalis, A. P. Mitsos, J. V. Byrne, and Y. Ventikos, "The haemodynamics of endovascular aneurysm treatment: a computational modelling approach for

estimating the influence of multiple coil deployment," *IEEE T. Med. Imaging*, vol. 27, no. 6, pp. 814–824, 2008.

[144] Y. Wei, S. Cotin, J. Allard, L. Fang, C. Pan, and S. Ma, "Interactive blood-coil simulation in real-time during aneurysm embolization," *Comput. Graph.*, vol. 35, no. 2, pp. 422–430, 2011.

[145] H. S. Byun and K. Rhee, "CFD modeling of blood flow following coil embolization of aneurysms," *Med. Eng. Phys.*, vol. 26, no. 9, pp. 755–761, 2004.

[146] A. Narracott, S. Smith, P. Lawford, H. Liu, R. Himeno, I. Wilkinson, P. Griffiths, and R. Hose, "Development and validation of models for the investigation of blood clotting in idealized stenoses and cerebral aneurysms," *J. Artif. Organs*, vol. 8, no. 1, pp. 56–62, 2005.

[147] C. M. Schirmer and A. M. Malek, "Critical influence of framing coil orientation on intra-aneurysmal and neck region hemodynamics in a sidewall aneurysm model," *Neurosurgery*, vol. 67, no. 6, pp. 1692–1702, 2010.

[148] A. Bernardini, I. Larrabide, L. Petrini, G. Pennati, E. Flore, M. Kim, and A. Frangi, "Deployment of self-expandable stents in aneurysmatic cerebral vessels: comparison of different computational approaches for interventional planning," *Comput. Method. Biomec.*, vol. 15, no. 3, pp. 303–311, 2012.

[149] S. De Bock, F. Iannaccone, G. De Santis, M. De Beule, P. Mortier, B. Verhegghe, and P. Segers, "Our capricious vessels: the influence of stent design and vessel geometry on the mechanics of intracranial aneurysm stent deployment," *J. Biomech.*, vol. 45, no. 8, pp. 1353–1359, 2012.

[150] E. Flore, I. Larrabide, L. Petrini, G. Pennati, and A. Frangi, "Stent deployment in aneurysmatic cerebral vessels: assessment and quantification of the differences between fast virtual stenting and finite element analysis," in *MICCAI 2009 Workshop on Cardiovasc. Interv. Imaging and Biophys. Model.*, vol. 5242. Springer-Verlag, Berlin, Germany, 2009, Conference Proceedings, p. 790–797.

[151] J. H. Kim, T. J. Kang, and W.-R. Yu, "Mechanical modeling of self-expandable stent fabricated using braiding technology," *J. Biomech.*, vol. 41, no. 15, pp. 3202–3212, 2008.

[152] L. Augsburger, P. Reymond, D. Rufenacht, and N. Stergiopulos, "Intracranial stents being modeled as a porous medium: flow simulation in stented cerebral aneurysms," *Ann. Biomed. Eng.*, vol. 39, no. 2, pp. 850–863, 2011.

[153] H. G. Morales and O. Bonnefous, "Modeling hemodynamics after flow diverter with a porous medium," in *IEEE Int. Sympos. Biomed. Imaging (ISBI)*. IEEE, 2014, Conference Proceedings, pp. 1324–1327.

[154] L. Flórez-Valencia, M. Orkisz, and J. Montagnat, "3d graphical models for vascular-stent pose simulation," *Mach. Grap. Vision*, vol. 13, no. 3, pp. 235–248, 2004.

[155] K. Spranger and Y. Ventikos, "Which spring is the best? comparison of methods for virtual stenting," *IEEE. T. Biomed. Eng.*, vol. 61, no. 7, pp. 1998–2010, 2014.

[156] W. Jeong, M. H. Han, and K. Rhee, "Effects of framing coil shape, orientation, and thickness on intra-aneurysmal flow," *Med. Biol. Eng. Comput.*, vol. 51, no. 9, pp. 981–990, 2013.

[157] M. L. Aguilar, H. G. Morales, I. Larrabide, J. M. Macho, L. San Roman, and A. F. Frangi, "Effect of coil surface area on the hemodynamics of a patient-specific intracranial aneurysm: A computational study," in *IEEE Int. Sympos. Biomed. Imaging (ISBI)*. IEEE, 2012, Conference Proceedings, pp. 1180–1183.

[158] H. G. Morales, M. Kim, E. Vivas, M.-C. Villa-Uriol, I. Larrabide, T. Sola, L. Guimaraens, and A. Frangi, "How do coil configuration and packing density influence intra-aneurysmal hemodynamics?" *Am. J. Neuroradiol.*, vol. 32, no. 10, pp. 1935–1941, 2011.

[159] I. Larrabide, M. Aguilar, H. Morales, A. Geers, Z. Kulcsár, D. Rüfenacht, and A. Frangi, "Intra-aneurysmal pressure and flow changes induced by flow diverters: relation to aneurysm size and shape," *Am. J. Neuroradiol.*, vol. 34, no. 4, pp. 816–822, 2013.

[160] I. Larrabide, A. J. Geers, M. L. Aguilar, H. G. Morales, D. Rufenacht, and A. F. Frangi, "Influence of vascular morphology on hemodynamic changes after flow diverter placement in saccular intracranial aneurysms," *MICCAI-STENT 2012*, pp. 7–16, 2012.

[161] I. Larrabide, A. J. Geers, H. G. Morales, M. L. Aguilar, and D. A. Rüfenacht, "Effect of aneurysm and ica morphology on hemodynamics before and after flow diverter treatment," *J. Neurointerv. Surg.*, vol. 7, no. 4, pp. 272–280, 2014.

[162] Y.-F. Wu, P.-F. Yang, J. Shen, Q.-H. Huang, X. Zhang, Y. Qian, and J.-M. Liu, "A comparison of the hemodynamic effects of flow diverters on wide-necked and narrow-necked cerebral aneurysms," *J. Clin. Neurosci.*, vol. 19, no. 11, pp. 1520–1524, 2012.

[163] P. Bouillot, O. Brina, R. Ouared, H. Yilmaz, K.-O. Lovblad, M. Farhat, and V. M. Pereira, "Computational fluid dynamics with stents: quantitative comparison with particle image velocimetry for three commercial off the shelf intracranial stents," *J. Neurointerv. Surg.*, vol. 8, no. 3, pp. 309–315, 2016.

[164] M. Kim, D. B. Taulbee, M. Tremmel, and H. Meng, "Comparison of two stents in modifying cerebral aneurysm hemodynamics," *Ann. Biomed. Eng.*, vol. 36, no. 5, pp. 726–741, 2008.

[165] B. N. Roszelle, P. Nair, L. F. Gonzalez, M. H. Babiker, J. Ryan, and D. Frakes, "Comparison among different high porosity stent configurations: hemodynamic effects of treatment in a large cerebral aneurysm," *J. Biomech. Eng. T. ASME*, vol. 136, no. 2, p. 021013, 2014.

[166] M. Tremmel, J. Xiang, S. K. Natarajan, L. N. Hopkins, A. H. Siddiqui, E. I. Levy, and H. Meng, "Alteration of intraaneurysmal hemodynamics for flow diversion using enterprise and vision stents," *World Neurosurg.*, vol. 74, no. 2, pp. 306–315, 2010.

[167] M. H. Babiker, L. F. Gonzalez, J. Ryan, F. Albuquerque, D. Collins, A. Elvikis, and D. H. Frakes, "Influence of stent configuration on cerebral aneurysm fluid dynamics," *J. Biomech.*, vol. 45, no. 3, pp. 440–447, 2012.

[168] M. Kim, I. Larrabide, M.-C. Villa-Uriol, and A. F. Frangi, "Hemodynamic alterations of a patient-specific intracranial aneurysm induced by virtual deployment of stents in various axial orientation," in *IEEE Int. Sympos. Biomed. Imaging (ISBI)*. IEEE, 2009, Conference Proceedings, pp. 1215–1218.

[169] K. Kono and T. Terada, "Hemodynamics of 8 different configurations of stenting for bifurcation aneurysms," *Am. J. Neuroradiol.*, vol. 34, no. 10, pp. 1980–1986, 2013.

[170] L. Augsburger, M. Farhat, P. Reymond, E. Fonck, Z. Kulcsar, N. Stergiopulos, and D. A. Rüfenacht, "Effect of flow diverter porosity on intraaneurysmal blood flow," *Clin. Neuroradiol.*, vol. 19, no. 3, pp. 204–214, 2009.

[171] T.-M. Liou and Y.-C. Li, "Effects of stent porosity on hemodynamics in a sidewall aneurysm model," *J. Biomech.*, vol. 41, no. 6, pp. 1174–1183, 2008.

[172] F. Mut and J. Cebral, "Effects of flow-diverting device oversizing on hemodynamics alteration in cerebral aneurysms," *Am. J. Neuroradiol.*, vol. 33, no. 10, pp. 2010–2016, 2012.

[173] D. Ma, J. Xiang, H. Choi, T. M. Dumont, S. Natarajan, A. Siddiqui, and H. Meng, "Enhanced aneurysmal flow diversion using a dynamic push-pull technique: an experimental and modeling study," *Am. J. Neuroradiol.*, vol. 35, no. 9, pp. 1779–1785, 2014.

[174] G. Janiga, L. Daróczy, P. Berg, D. Thévenin, M. Skalej, and O. Beuing, "An automatic CFD-based flow diverter optimization principle for patient-specific intracranial aneurysms," *J. Biomech.*, vol. 48, no. 14, pp. 3846–3852, 2015.

[175] C. Li, S. Wang, J. Chen, H. Yu, Y. Zhang, F. Jiang, S. Mu, H. Li, and X. Yang, "Influence of hemodynamics on recanalization of totally occluded intracranial aneurysms: a patient-specific computational fluid dynamic simulation study: Laboratory investigation," *J. Neurosurg.*, vol. 117, no. 2, pp. 276–283, 2012.

[176] B. Luo, X. Yang, S. Wang, H. Li, J. Chen, H. Yu, Y. Zhang, Y. Zhang, S. Mu, and Z. Liu, "High shear stress and flow velocity in partially occluded aneurysms prone to recanalization," *Stroke*, vol. 42, no. 3, pp. 745–753, 2011.

[177] F. Graziano, V. Russo, W. Wang, D. Khismatullin, and A. Ulm, "3d computational fluid dynamics of a treated vertebrobasilar giant aneurysm: a multistage analysis," *Am. J. Neuroradiol.*, vol. 34, no. 7, pp. 1387–1394, 2013.

[178] W. Park, Y. Song, K. J. Park, H.-W. Koo, K. Yang, and D. C. Suh, "Hemodynamic characteristics regarding recanalization of completely coiled aneurysms: Computational fluid dynamic analysis using virtual models comparison," *Neurointervention*, vol. 11, no. 1, pp. 30–36, 2016.

[179] B. Chung, F. Mut, R. Kadirvel, R. Lingineni, D. F. Kallmes, and J. R. Cebral, "Hemodynamic analysis of fast and slow aneurysm occlusions by flow diversion in rabbits," *J. Neurointerv. Surg.*, vol. 7, no. 12, pp. 931–935, 2015.

[180] F. Mut, M. Raschi, E. Scrivano, C. Bleise, J. Chudyk, R. Ceratto, P. Lylyk, and J. R. Cebral, "Association between hemodynamic conditions and occlusion times after flow diversion in cerebral aneurysms," *J. Neurointerv. Surg.*, vol. 7, no. 4, pp. 286–290, 2014.

[181] Z. Kulcsár, L. Augsburger, P. Reymond, V. M. Pereira, S. Hirsch, A. S. Mallik, J. Millar, S. G. Wetzel, I. Wanke, and D. A. Rüfenacht, "Flow diversion treatment: intra-aneurismal blood flow velocity and wss reduction are parameters to predict aneurysm thrombosis," *Acta Neurochir.*, vol. 154, no. 10, pp. 1827–1834, 2012.

[182] R. Ouared, I. Larrabide, O. Brina, P. Bouillot, G. Erceg, H. Yilmaz, K.-O. Lovblad, and V. M. Pereira, "Computational fluid dynamics analysis of flow reduction induced by flow-diverting stents in intracranial aneurysms: a patient-unspecific hemodynamics change perspective," *J. Neurointerv. Surg.*, vol. 8, no. 12, pp. 1288–1293, 2016.

[183] K. T. Tan and G. Y. Lip, "Red vs white thrombi: treating the right clot is crucial," *Arch. Intern. Med.*, vol. 163, no. 20, pp. 2534–2535, 2003.

[184] M. R. Levitt, M. C. Barbour, S. R. du Roscoat, C. Geindreau, V. K. Chivukula, P. M. McGah, J. D. Nerva, R. P. Morton, L. J. Kim, and A. Aliseda, "Computational fluid dynamics of cerebral aneurysm coiling using high-resolution and high-energy synchrotron x-ray microtomography: comparison with the homogeneous porous medium approach," *J. Neurointerv. Surg.*, pp. Published Online First: 12 July 2016, doi: 10.1136/neurintsurg–2016–012 479, 2016.

[185] M. Raschi, F. Mut, R. Löhner, and J. Cebral, "Strategy for modeling flow diverters in cerebral aneurysms as a porous medium," *Int. J. Numer. Meth. Bio.*, vol. 30, no. 9, pp. 909–925, 2014.

[186] P. Bouillot, O. Brina, H. Yilmaz, M. Farhat, G. Erceg, K.-O. Lovblad, M. Vargas, Z. Kulcsar, and V. Pereira, "Virtual-versus-real implantation of flow diverters: Clinical potential and influence of vascular geometry," *Am. J. Neuroradiol.*, vol. 37, no. 11, pp. 2079–2086, 2016.

[187] B. Gao, M. Baharoglu, A. Cohen, and A. Malek, "Stent-assisted coiling of intracranial bifurcation aneurysms leads to immediate and delayed intracranial vascular angle remodeling," *Am. J. Neuroradiol.*, vol. 33, no. 4, pp. 649–654, 2012.

[188] R. King, J.-Y. Chueh, I. van der Bom, C. Silva, S. Carniato, G. Spilberg, A. Wakhloo, and M. Gounis, "The effect of intracranial stent implantation on the curvature of the cerebrovasculature," *Am. J. Neuroradiol.*, vol. 33, no. 9, pp. 1657–1662, 2012.

[189] K. Kono, A. Shintani, and T. Terada, "Hemodynamic effects of stent struts versus straightening of vessels in stent-assisted coil embolization for sidewall cerebral aneurysms," *PloS One*, vol. 9, no. 9, p. e108033, 2014.

[190] D. Fiorella, H. H. Woo, F. C. Albuquerque, and P. K. Nelson, "Definitive reconstruction of circumferential, fusiform intracranial aneurysms with the pipeline embolization device," *Neurosurgery*, vol. 62, no. 5, pp. 1115–1121, 2008.

[191] F. Mut, D. Ruijters, D. Babic, C. Bleise, P. Lylyk, and J. R. Cebral, "Effects of changing physiologic conditions on the in vivo quantification of hemodynamic variables in cerebral aneurysms treated with flow diverting devices," *Int. J. Numer. Meth. Bio.*, vol. 30, no. 1, pp. 135–142, 2014.

[192] I. Whittle, N. W. Dorsch, and M. Besser, "Spontaneous thrombosis in giant intracranial aneurysms," *J. Neurol. Neurosur. Ps.*, vol. 45, no. 11, pp. 1040–1047, 1982.

[193] W. Brinjikji, D. F. Kallmes, and R. Kadirvel, "Mechanisms of healing in coiled intracranial aneurysms: a review of the literature," *Am. J. Neuroradiol.*, vol. 36, no. 7, pp. 1216–1222, 2015.

[194] I. Szikora, Z. Berentei, Z. Kulcsar, M. Marosfoi, Z. Vajda, W. Lee, A. Berez, and P. K. Nelson, "Treatment of intracranial aneurysms by functional reconstruction of the parent artery: the budapest experience with the pipeline embolization device," *Am. J. Neuroradiol.*, vol. 31, no. 6, pp. 1139–1147, 2010.

[195] P. Lylyk, C. Miranda, R. Ceratto, A. Ferrario, E. Scrivano, H. R. Luna, A. L. Berez, Q. Tran, P. K. Nelson, and D. Fiorella, "Curative endovascular reconstruction of cerebral aneurysms with the pipeline embolization device: the buenos aires experience," *Neurosurgery*, vol. 64, no. 4, pp. 632–643, 2009.

[196] E. Crobeddu, G. Lanzino, D. F. Kallmes, and H. Cloft, "Review of 2 decades of aneurysm-recurrence literature, part 2: managing recurrence after endovascular coiling," *Am. J. Neuroradiol.*, vol. 34, no. 3, pp. 481–485, 2013.

[197] E. Crobeddu, G. Lanzino, D. F. Kallmes, and H. Cloft, "Review of 2 decades of aneurysm-recurrence literature, part 1: reducing recurrence after endovascular coiling," *Am. J. Neuroradiol.*, vol. 34, no. 2, pp. 266–270, 2013.

[198] A. H. Siddiqui, A. A. Abla, P. Kan, T. M. Dumont, S. Jahshan, G. W. Britz, L. N. Hopkins, and E. I. Levy, "Panacea or problem: flow diverters in the treatment of symptomatic large or giant fusiform vertebrobasilar aneurysms: Clinical article," *J. Neurosurg.*, vol. 116, no. 6, pp. 1258–1266, 2012.

[199] S. Fischer, Z. Vajda, M. A. Perez, E. Schmid, N. Hopf, H. Bäzner, and H. Henkes, "Pipeline embolization device (PED) for neurovascular reconstruction: initial experience in the treatment of 101 intracranial aneurysms and dissections," *Neuroradiology*, vol. 54, no. 4, pp. 369–382, 2012.

[200] J. Frösen, R. Tulamo, A. Paetau, E. Laaksamo, M. Korja, A. Laakso, M. Niemelä, and J. Hernesniemi, "Saccular intracranial aneurysm: pathology and mechanisms," *Acta Neuropathol.*, vol. 123, no. 6, pp. 773–786, 2012.

[201] M. Hoffman, "A cell-based model of coagulation and the role of factor viia," *Blood Rev.*, vol. 17, pp. S1–S5, 2003.

[202] H. A. Himburg, S. E. Dowd, and M. H. Friedman, "Frequency-dependent response of the vascular endothelium to pulsatile shear stress," *Am. J. Physiol. Heart C.*, vol. 293(1), pp. H645–H653, 2007.

[203] Y.-D. Li, B.-Q. Ye, S.-X. Zheng, J.-T. Wang, J.-G. Wang, M. Chen, J.-G. Liu, X.-H. Pei, L.-J. Wang, and Z.-X. Lin, "Nf-κb transcription factor p50 critically regulates tissue factor in deep vein thrombosis," *J. Biol. Chem.*, vol. 284, no. 7, pp. 4473–4483, 2009.

[204] N. Mackman, "Role of tissue factor in hemostasis, thrombosis, and vascular development," *Arterioscl. Throm. Vas.*, vol. 24, no. 6, pp. 1015–1022, 2004.

[205] J. Biasetti, T. C. Gasser, M. Auer, U. Hedin, and F. Labruto, "Hemodynamics of the normal aorta compared to fusiform and saccular abdominal aortic aneurysms with emphasis on a potential thrombus formation mechanism," *Ann. Biomed. Eng.*, vol. 38, no. 2, pp. 380–390, 2010.

[206] J. Biasetti, F. Hussain, and T. C. Gasser, "Blood flow and coherent vortices in the normal and aneurysmatic aortas: a fluid dynamical approach to intra-luminal thrombus formation," *J. R. Soc. Interface*, vol. 8, no. 63, p. 1449–1461, 2011.

[207] P. F. Davies, "Flow-mediated endothelial mechanotransduction," *Physiol. Rev.*, vol. 75, no. 3, pp. 519–560, 1995.

[208] T. Bodnár, A. Fasano, and A. Sequeira, *Mathematical models for blood coagulation.* Springer, 2014, pp. 483–569.

[209] M. S. Chatterjee, W. S. Denney, H. Jing, and S. L. Diamond, "Systems biology of coagulation initiation: kinetics of thrombin generation in resting and activated human blood," *PloS Comput. Biol.*, vol. 6, no. 9, p. e1000950, 2010.

[210] W. Chong, Y. Zhang, Y. Qian, L. Lai, G. Parker, and K. Mitchell, "Computational hemodynamics analysis of intracranial aneurysms treated with flow diverters: correlation with clinical outcomes," *Am. J. Neuroradiol.*, vol. 35, no. 1, pp. 136–142, 2014.

[211] O. Malaspinas, A. Turjman, D. R. de Sousa, G. Garcia-Cardena, M. Raes, P.-T. Nguyen, Y. Zhang, G. Courbebaisse, C. Lelubre, and K. Z. Boudjeltia, "A spatio-temporal model for spontaneous thrombus formation in cerebral aneurysms," *J. Theor. Biol.*, vol. 394, pp. 68–76, 2016.

[212] C. Ou, W. Huang, and M. M.-F. Yuen, "A computational model based on fibrin accumulation for the prediction of stasis thrombosis following flow-diverting treatment in cerebral aneurysms," *Med. Biol. Eng. Comput.*, pp. 1–11, 2016.

[213] K. C. Koskinas, Y. S. Chatzizisis, A. P. Antoniadis, and G. D. Giannoglou, "Role of endothelial shear stress in stent restenosis and thrombosis: pathophysiologic mechanisms and implications for clinical translation," *J. Am. Coll. Cardiol.*, vol. 59, no. 15, pp. 1337–1349, 2012.

[214] V. Rayz, L. Boussel, L. Ge, J. Leach, A. Martin, M. Lawton, C. McCulloch, and D. Saloner, "Flow residence time and regions of intraluminal thrombus deposition in intracranial aneurysms," *Ann. Biomed. Eng.*, vol. 38, no. 10, pp. 3058–3069, 2010.

[215] R. Ouared and B. Chopard, "Lattice boltzmann simulations of blood flow: non-newtonian rheology and clotting processes," *J. Stat. Phys.*, vol. 121, no. 1-2, pp. 209–221, 2005.

[216] S. Zimny, B. Chopard, O. Malaspinas, E. Lorenz, K. Jain, S. Roller, and J. Bernsdorf, "A multiscale approach for the coupled simulation of blood flow and thrombus formation in intracranial aneurysms," *Procedia Comput. Sci.*, vol. 18, pp. 1006–1015, 2013.

[217] J. Biasetti, P. G. Spazzini, J. Swedenborg, and T. C. Gasser, "An integrated fluid-chemical model toward modeling the formation of intra-luminal thrombus in abdominal aortic aneurysms," *Front. Physiol.*, vol. 3, p. 266, 2012.

[218] S. Cito, M. D. Mazzeo, and L. Badimon, "A review of macroscopic thrombus modeling methods," *Thromb. Res,*, vol. 131, no. 2, pp. 116–124, 2013.

[219] C. M. Danforth, T. Orfeo, K. G. Mann, K. E. Brummel-Ziedins, and S. J. Everse, "The impact of uncertainty in a blood coagulation model," *Math. Med. Biol.*, vol. 26, no. 4, pp. 323–336, 2009.

[220] D. Luan, M. Zai, and J. D. Varner, "Computationally derived points of fragility of a human cascade are consistent with current therapeutic strategies," *PloS Comput. Biol.*, vol. 3, no. 7, p. e142, 2007.

[221] G. Moiseyev and P. Z. Bar-Yoseph, "Computational modeling of thrombosis as a tool in the design and optimization of vascular implants," *J. Biomech.*, vol. 46, no. 2, pp. 248–252, 2013.

[222] C. S. Ogilvy, M. H. Chua, M. R. Fusco, A. S. Reddy, and A. J. Thomas, "Stratification of recanalization for patients with endovascular treatment of intracranial aneurysms," *Neurosurgery*, vol. 76, no. 4, pp. 390–395, 2015.

[223] C. S. Ogilvy, M. H. Chua, M. R. Fusco, C. J. Griessenauer, M. R. Harrigan, A. Sonig, A. H. Siddiqui, E. I. Levy, K. Snyder, and M. Avery, "Validation of a system to predict recanalization after endovascular treatment of intracranial aneurysms," *Neurosurgery*, vol. 77, no. 2, pp. 168–174, 2015.

[224] A. Arzani, A. M. Gambaruto, G. Chen, and S. C. Shadden, "Lagrangian wall shear stress structures and near-wall transport in high-schmidt-number aneurysmal flows," *J. Fluid Mech.*, vol. 790, pp. 158–172, 2016.

[225] J. R. Cebral and H. Meng, "Counterpoint: realizing the clinical utility of computational fluid dynamics—closing the gap," *Am. J. Neuroradiol.*, vol. 33, no. 3, pp. 396–398, 2012.

[226] P. Hennig, M. A. Osborne, and M. Girolami, "Probabilistic numerics and uncertainty in computations," in *P. Roy. Soc. A Math. Phy.*, vol. 471, 2015, Conference Proceedings, p. 20150142.

[227] S. Sankaran, L. Grady, and C. A. Taylor, "Impact of geometric uncertainty on hemodynamic simulations using machine learning," *Comput. Meth. Appl. M.*, vol. 297, pp. 167–190, 2015.

[228] J. Mikhal, D. Kroon, C. Slump, and B. Geurts, "Flow prediction in cerebral aneurysms based on geometry reconstruction from 3d rotational angiography," *Int. J. Numer. Meth. Bio.*, vol. 29, no. 7, pp. 777–805, 2013.

[229] J. Schneiders, H. Marquering, L. Antiga, R. Van den Berg, E. VanBavel, and C. Majoie, "Intracranial aneurysm neck size overestimation with 3d rotational angiography: the impact on intra-aneurysmal hemodynamics simulated with computational fluid dynamics," *Am. J. Neuroradiol.*, vol. 34, no. 1, pp. 121–128, 2013.

[230] D. M. Sforza, R. Löhner, C. Putman, and J. R. Cebral, "Hemodynamic analysis of intracranial aneurysms with moving parent arteries: basilar tip aneurysms," *Int. J. Numer. Meth. Bio.*, vol. 26, no. 10, pp. 1219–1227, 2010.

[231] P. F. Davies, "Hemodynamic shear stress and the endothelium in cardiovascular pathophysiology," *Nat. Rev. Cardiol.*, vol. 6(1), pp. 16–26, 2009.

[232] J.-J. Chiu and S. Chien, "Effects of disturbed flow on vascular endothelium: pathophysiological basis and clinical perspectives," *Physiol. Rev.*, vol. 91(1), pp. 327–387, 2011.

[233] S.-W. Lee, L. Antiga, and D. A. Steinman, "Correlations among indicators of disturbed flow at the normal carotid bifurcation," *J. Biomech. Eng. T. ASME*, vol. 131(6), p. 061013, 2009.

[234] D. N. Ku, D. P. Giddens, C. K. Zarins, and S. Glagov, "Pulsatile flow and atherosclerosis in the human carotid bifurcation. positive correlation between plaque location and low oscillating shear stress." *Arterioscl. Throm. Vas.*, vol. 5(3), pp. 293–302, 1985.

[235] N. DePaola, M. Gimbrone, P. F. Davies, and C. Dewey, "Vascular endothelium responds to fluid shear stress gradients." *Arterioscl. Throm. Vas.*, vol. 12(11), pp. 1254–1257, 1992.

[236] J. M. Dolan, J. Kolega, and H. Meng, "High wall shear stress and spatial gradients in vascular pathology: a review," *Ann. Biomed. Eng.*, vol. 41(7), pp. 1411–1427, 2013.

[237] H. A. Himburg and M. H. Friedman, "Correspondence of low mean shear and high harmonic content in the porcine iliac arteries," *J. Biomech. Eng. T. ASME*, vol. 128(6), pp. 852–856, 2006.

[238] L. Boussel, V. Rayz, A. Martin, G. Acevedo-Bolton, M. T. Lawton, R. Higashida, W. S. Smith, W. L. Young, and D. Saloner, "Phase-contrast magnetic resonance imaging measurements in intracranial aneurysms in vivo of flow patterns, velocity fields, and wall shear stress: comparison with computational fluid dynamics," *Magn. Reson. Med.*, vol. 61(2), no. 2, pp. 409–417, 2009.

[239] V. Peiffer, S. J. Sherwin, and P. D. Weinberg, "Computation in the rabbit aorta of a new metric–the transverse wall shear stress–to quantify the multidirectional character of disturbed blood flow," *J. Biomech.*, vol. 46(15), pp. 2651–2658, 2013.

[240] J. Xiang, V. Tutino, K. Snyder, and H. Meng, "CFD: computational fluid dynamics or confounding factor dissemination? The role of hemodynamics in intracranial aneurysm rupture risk assessment," *Am. J. Neuroradiol.*, vol. 35(10), pp. 1849–1857, 2014.

[241] J. Xiang, S. K. Natarajan, M. Tremmel, D. Ma, J. Mocco, L. N. Hopkins, A. H. Siddiqui, E. I. Levy, and H. Meng, "Hemodynamic–morphologic discriminants for intracranial aneurysm rupture," *Stroke*, vol. 42(1), pp. 144–152, 2011.

[242] J. Bisbal, G. Engelbrecht, M.-C. Villa-Uriol, and A. F. Frangi, "Prediction of cerebral aneurysm rupture using hemodynamic, morphologic and clinical features: a data mining approach," in *Int. Conf. Database Expert Syst. Applic.* Springer, 2011, pp. 59–73.

[243] M. Villa-Uriol, G. Berti, D. Hose, A. Marzo, A. Chiarini, J. Penrose, J. Pozo, J. Schmidt, P. Singh, R. Lycett *et al.*, "@neurIST: complex information processing toolchain for the integrated management of cerebral aneurysms," *Interface Focus*, vol. 1, no. 3, pp. 308–319, 2011.

[244] C. E. Rasmussen, "Gaussian processes in machine learning," in *Advanced lectures on machine learning.* Springer, 2004, pp. 63–71.

[245] A. G. Brown, Y. Shi, A. Marzo, C. Staicu, I. Valverde, P. Beerbaum, P. V. Lawford, and D. R. Hose, "Accuracy vs. computational time: translating aortic simulations to the clinic," *J. Biomech.*, vol. 45(3), pp. 516–523, 2012.

[246] N. Stergiopulos, D. Young, and T. Rogge, "Computer simulation of arterial flow with applications to arterial and aortic stenoses," *J. Biomech.*, vol. 25(12), pp. 1477–1488, 1992.

[247] I. E. Vignon-Clementel, C. Figueroa, K. Jansen, and C. Taylor, "Outflow boundary conditions for 3d simulations of non-periodic blood flow and pressure fields in deformable arteries," *Comput. Method. Biomec.*, vol. 13(5), pp. 625–640, 2010.

[248] V. Peiffer, S. J. Sherwin, and P. D. Weinberg, "Does low and oscillatory wall shear stress correlate spatially with early atherosclerosis? a systematic review," *Cardiovasc. Res.*, 2013, dOI: http://dx.doi.org/10.1093/cvr/cvt044.

[249] A. Arzani and S. C. Shadden, "Characterizations and correlations of wall shear stress in aneurysmal flow," *J. Biomech. Eng. T. ASME*, vol. 138(1), p. 014503, 2016.

[250] U. Morbiducci, D. Gallo, S. Cristofanelli, R. Ponzini, M. A. Deriu, G. Rizzo, and D. A. Steinman, "A rational approach to defining principal axes of multidirectional wall shear stress in realistic vascular geometries, with application to the study of the influence of helical flow on wall shear stress directionality in aorta," *J. Biomech.*, vol. 48(6), pp. 899–906, 2015.

[251] D. A. Steinman, *Assumptions in modelling of large artery hemodynamics.* Springer, 2012, pp. 1–18.

[252] T. Yagi, A. Sato, M. Shinke, S. Takahashi, Y. Tobe, H. Takao, Y. Murayama, and M. Umezu, "Experimental insights into flow impingement in cerebral aneurysm by stereoscopic particle image velocimetry: transition from a laminar regime," *J. R. Soc. Interface*, vol. 10, no. 82, p. 20121031, 2013.

[253] T. Becske, D. Kallmes, I. Saatci, C. McDougall, I. Szikora, G. Lanzino, C. Moran, H. Woo, D. Lopes, A. Berez *et al.*, "Pipeline for uncoilable or failed aneurysms: results from a multicenter clinical trial," *Radiology*, vol. 267, no. 3, pp. 858–868, 2013.

[254] Z. Kulcsár and I. Szikora, "The ESMINT retrospective analysis of delayed aneurysm ruptures after flow diversion (RADAR) study," *EJMINT*, vol. 2012, p. 1244000088, 2012.

[255] B. Turowski, S. Macht, Z. Kulcsár, D. Hänggi, and W. Stummer, "Early fatal hemorrhage after endovascular cerebral aneurysm treatment with a flow diverter (silk-stent)," *Neuroradiology*, vol. 53, no. 1, pp. 37–41, 2011.

[256] R. Kadirvel, Y.-H. Ding, D. Dai, I. Rezek, D. Lewis, and D. Kallmes, "Cellular mechanisms of aneurysm occlusion after treatment with a flow diverter," *Radiology*, vol. 270, no. 2, pp. 394–399, 2014.

[257] I. Szikora, E. Turányi, and M. Marosfoi, "Evolution of flow-diverter endothelialization and thrombus organization in giant fusiform aneurysms after flow diversion: a histopathologic study," *Am. J. Neuroradiol.*, vol. 36, no. 9, pp. 1716–1720, 2015.

[258] A. Undas and R. Ariëns, "Fibrin clot structure and function: a role in the pathophysiology of arterial and venous thromboembolic diseases," *Arterioscl. Throm. Vas.*, vol. 31, no. 12, pp. e88–e99, 2011.

[259] J. Weisel and R. Litvinov, "The biochemical and physical process of fibrinolysis and effects of clot structure and stability on the lysis rate," *Cardiovasc. Hematol. Agents Med. Chem.*, vol. 6, no. 3, pp. 161–180, 2008.

[260] Z. Kulcsár, E. Houdart, A. Bonafe, G. Parker, J. Millar, A. Goddard, S. Renowden, G. Gal, B. Turowski, K. Mitchell *et al.*, "Intra-aneurysmal thrombosis as a possible cause of delayed aneurysm rupture after flow-diversion treatment," *Am. J. Neuroradiol.*, vol. 32, no. 1, pp. 20–25, 2011.

[261] M. Chow, C. McDougall, C. O'Kelly, R. Ashforth, E. Johnson, and D. Fiorella, "Delayed spontaneous rupture of a posterior inferior cerebellar artery aneurysm following treatment with flow diversion: a clinicopathologic study," *Am. J. Neuroradiol.*, vol. 33, no. 4, pp. E46–E51, 2012.

[262] G. Kuzmik, T. Williamson, A. Ediriwickrema, A. Andeejani, and K. Bulsara, "Flow diverters and a tale of two aneurysms," *J. Neurointerv. Surg.*, vol. 5, no. 4, pp. e23–e23, 2013.

[263] J. Xiang, D. Ma, K. Snyder, E. Levy, A. Siddiqui, and H. Meng, "Increasing flow diversion for cerebral aneurysm treatment using a single flow diverter," *Neurosurgery*, vol. 75, no. 3, pp. 286–294, 2014.

[264] T. Bodnár, A. Fasano, and A. Sequeira, "Mathematical models for blood coagulation," in *Fluid-Structure Interaction and Biomedical Applications*. Springer, 2014, pp. 483–569.

[265] H. Versteeg, J. Heemskerk, M. Levi, and P. Reitsma, "New fundamentals in hemostasis," *Physiol. Rev.*, vol. 93, no. 1, pp. 327–358, 2013.

[266] D. de Sousa, C. Vallecilla, K. Chodzynski, R. Jerez, O. Malaspinas, O. Eker, R. Ouared, L. Vanhamme, A. Legrand, B. Chopard *et al.*, "Determination of a shear rate threshold for thrombus formation in intracranial aneurysms," *J. Neurointerv. Surg.*, vol. 8, pp. 853–858, 2015.

[267] Y. Aida and K. Shimano, "Modelling of blood coagulation in cerebral aneurysms," *WIT Trans. Biomed. Health*, vol. 17, pp. 51–62, 2013.

[268] K. Shimano, Y. Aida, and Y. Nakagawa, "Slowness of blood flow and resultant thrombus formation in cerebral aneurysms," *J. Biorheol.*, vol. 24, no. 2, p. 47, 2010.

[269] W. Nesbitt, E. Westein, F. Tovar-Lopez, E. Tolouei, A. Mitchell, J. Fu, J. Carberry, A. Fouras, and S. Jackson, "A shear gradient–dependent platelet aggregation mechanism drives thrombus formation," *Nat. Med.*, vol. 15, no. 6, p. 665, 2009.

[270] M. Ngoepe and Y. Ventikos, "Computational modelling of clot development in patient-specific cerebral aneurysm cases," *J. Thromb. Haemost.*, vol. 14, no. 2, pp. 262–272, 2016.

[271] C. Ou, W. Huang, and M.-F. Yuen, "A computational model based on fibrin accumulation for the prediction of stasis thrombosis following flow-diverting treatment in cerebral aneurysms," *Med. Biol. Eng. Comput.*, vol. 55, no. 1, pp. 89–99, 2017.

[272] J. Cebral, F. Mut, M. Raschi, S. Hodis, Y.-H. Ding, B. Erickson, R. Kadirvel, and D. Kallmes, "Analysis of hemodynamics and aneurysm occlusion after flow-diverting treatment in rabbit models," *Am. J. Neuroradiol.*, vol. 35, no. 8, pp. 1567–1573, 2014.

[273] R. Ouared, I. Larrabide, O. Brina, P. Bouillot, G. Erceg, H. Yilmaz, K.-O. Lovblad, and V. Pereira, "Computational fluid dynamics analysis of flow reduction induced by flow-diverting stents in intracranial aneurysms: a patient-unspecific hemodynamics change perspective," *J. Neurointerv. Surg.*, pp. neurintsurg–2015, 2016.

[274] V. Rayz, L. Boussel, L. Ge, J. Leach, A. Martin, M. Lawton, C. McCulloch, and D. Saloner, "Flow residence time and regions of intraluminal thrombus deposition in intracranial aneurysms," *Ann. Biomed. Eng.*, vol. 38, no. 10, pp. 3058–3069, 2010.

[275] A. Kuharsky and A. Fogelson, "Surface-mediated control of blood coagulation: the role of binding site densities and platelet deposition," *Biophys. J.*, vol. 80, no. 3, pp. 1050–1074, 2001.

[276] M. Anand, K. Rajagopal, and K. Rajagopal, "A model incorporating some of the mechanical and biochemical factors underlying clot formation and dissolution in flowing blood," *Comput. Math. Method. M.*, vol. 5, no. 3-4, pp. 183–218, 2003.

[277] K. Leiderman and A. Fogelson, "Grow with the flow: a spatial–temporal model of platelet deposition and blood coagulation under flow," *Math. Med. Biol.*, vol. 28, no. 1, pp. 47–84, 2011.

[278] E. Sorensen, G. Burgreen, W. Wagner, and J. Antaki, "Computational simulation of platelet deposition and activation: I. Model development and properties," *Ann. Biomed. Eng.*, vol. 27, no. 4, pp. 436–448, 1999.

[279] B. Ingalls, *Mathematical modeling in systems biology: an introduction.* MIT Press, 2013.

[280] A. Wufsus, N. Macera, and K. Neeves, "The hydraulic permeability of blood clots as a function of fibrin and platelet density," *Biophys. J.*, vol. 104, no. 8, pp. 1812–1823, 2013.

[281] J. Taylor, R. Meyer, S. Deutsch, and K. Manning, "Development of a computational model for macroscopic predictions of device-induced thrombosis," *Biomech. Model. Mechan.*, vol. 15, no. 6, pp. 1713–1731, 2016.

[282] I. Larrabide, M. Kim, L. Augsburger, M. Villa-Uriol, D. Rüfenacht, and A. Frangi, "Fast virtual deployment of self-expandable stents: method and in vitro evaluation for intracranial aneurysmal stenting," *Med. Image Anal.*, vol. 16, no. 3, pp. 721–730, 2012.

[283] S. Appanaboyina, F. Mut, R. Löhner, C. Putman, and J. Cebral, "Simulation of intracranial aneurysm stenting: techniques and challenges," *Comput. Meth. Appl. M.*, vol. 198, no. 45-46, pp. 3567–3582, 2009.

[284] M. Anand, K. Rajagopal, and K. Rajagopal, "A model for the formation, growth, and lysis of clots in quiescent plasma. a comparison between the effects of antithrombin III deficiency and protein C deficiency," *J. Theor. Biol.*, vol. 253, no. 4, pp. 725–738, 2008.

[285] B. Chung, F. Mut, R. Kadirvel, R. Lingineni, D. Kallmes, and J. Cebral, "Hemodynamic analysis of fast and slow aneurysm occlusions by flow diversion in rabbits," *J. Neurointerv. Surg.*, vol. 7, no. 12, pp. 931–935, 2015.

[286] F. Mut, M. Raschi, E. Scrivano, C. Bleise, J. Chudyk, R. Ceratto, P. Lylyk, and J. Cebral, "Association between hemodynamic conditions and occlusion times after flow diversion in cerebral aneurysms," *J. Neurointerv. Surg.*, vol. 7, no. 4, pp. 286–290, 2015.

[287] L. Augsburger, M. Farhat, P. Reymond, E. Fonck, Z. Kulcsar, N. Stergiopulos, and D. Rüfenacht, "Effect of flow diverter porosity on intraaneurysmal blood flow," *Clin. Neuroradiol.*, vol. 19, no. 3, pp. 204–214, 2009.

[288] A. Gooya, K. Lekadir, X. Alba, A. J. Swift, J. M. Wild, and A. F. Frangi, "Joint clustering and component analysis of correspondenceless point sets: application to cardiac statistical modeling," in *Inform. Process Med. Imaging – IPMI 2015*. Springer, 2015, pp. 98–109.

[289] S. Sankaran and A. L. Marsden, "A stochastic collocation method for uncertainty quantification and propagation in cardiovascular simulations," *J. Biomech. Eng. T. ASME*, vol. 133, no. 3, p. 031001, 2011.

[290] J. Xiang, L. Antiga, N. Varble, K. V. Snyder, E. I. Levy, A. H. Siddiqui, and H. Meng, "AView: an image-based clinical computational tool for intracra-

nial aneurysm flow visualization and clinical management," *Ann. Biomed. Eng.*, vol. 44, no. 4, pp. 1085–1096, 2016.

[291] I. Larrabide, M.-C. Villa-Uriol, R. Cárdenes, V. Barbarito, L. Carotenuto, A. J. Geers, H. G. Morales, J. M. Pozo, M. D. Mazzeo, H. Bogunović *et al.*, "Angiolab—a software tool for morphological analysis and endovascular treatment planning of intracranial aneurysms," *Comput. Methods Programs Biomed.*, vol. 108, no. 2, pp. 806–819, 2012.

[292] Lassila, T., L. Di Marco, M. Mitolo, V. Iaia, G. Levedianos, A. Venneri, and A. Frangi, "Screening for cognitive impairment by model assisted cerebral blood flow estimation," *IEEE. T. Biomed. Eng.*, 2017, dOI: http://dx.doi.org/10.1109/TBME.2017.2759511.

[293] Mader, G., M. Olufsen, and A. Mahdi, "Modeling cerebral blood flow velocity during orthostatic stress," *Ann. Biomed. Eng.*, vol. 43(8), pp. 1748–1758, 2015.

[294] K. J., P. Szydlik, D. Liebeskind, J. Kochanowicz, O. Bronov, Z. Mariak, and E. Melhem, "Age and sex variability and normal reference values for the VMCA/VICA index," *Am. J. Neuroradiol.*, vol. 26, no. 4, pp. 730–735, 2005.

[295] Boccadifuoco, A., A. Mariotti, S. Celi, N. Martini, and M. Salvetti, "Impact of uncertainties in outflow boundary conditions on the predictions of hemodynamic simulations of ascending thoracic aortic aneurysms," *Comput. Fluids*, vol. 165, pp. 96–115, 2018.

[296] Vlak, M.H.M., G. Rinkel, P. Greebe, and A. Algra, "Risk of rupture of an intracranial aneurysm based on patient characteristics: a case–control study," *Stroke*, vol. 44, no. 5, pp. 1256–1259, 2013.

[297] Vlak, M.H.M., G. Rinkel, P. Greebe, J. van der Bom, and A. Algra, "Trigger factors and their attributable risk for rupture of intracranial aneurysms: a case-crossover study," *Stroke*, vol. 42, no. 7, pp. 1878–1882, 2011.

[298] Villa-Uriol, M.C., G. Berti, D. Hose, A. Marzo, A. Chiarini, J. Penrose, J. Pozo, J. Schmidt, P. Singh, R. Lycett *et al.*, "@neurIST: complex information processing toolchain for the integrated management of cerebral aneurysms," *Interface Focus*, vol. 1, no. 3, pp. 308–319, 2011.

[299] Ogoh, S., P. Fadel, R. Zhang, C. Selmer, Ø. Jans, N. Secher, and P. B. Raven, "Middle cerebral artery flow velocity and pulse pressure during dynamic exercise in humans," *Am. J. Physiol. Heart C.*, vol. 288, no. 4, pp. H1526–H1531, 2005.

[300] K. Wolstencroft, R. Haines, D. Fellows, A. Williams, D. Withers, S. Owen, S. Soiland-Reyes, I. Dunlop, A. Nenadic, P. Fisher *et al.*, "The taverna workflow suite: designing and executing workflows of web services on the desktop, web or in the cloud," *Nucleic Acids Res.*, vol. 41, no. W1, pp. W557–W561, 2013.

[301] Sarrami-Foroushani, A., T. Lassila, and A. Frangi, "Virtual endovascular treatment of intracranial aneurysms: models and uncertainty," *Wiley Interdiscip. Rev. Syst. Biol. Med.*, vol. 9, no. 4, 2017.

[302] L. Boussel, V. Rayz, C. McCulloch, A. Martin, G. Acevedo-Bolton, M. Lawton, R. Higashida, W. S. Smith, W. L. Young, and D. Saloner, "Aneurysm growth occurs at region of low wall shear stress patient-specific correlation of hemodynamics and growth in a longitudinal study," *Stroke*, vol. 39, no. 11, pp. 2997–3002, 2008.

[303] M. E. Tipping and C. M. Bishop, "Mixtures of probabilistic principal component analyzers," *Neural Comput.*, vol. 11, no. 2, pp. 443–482, 1999.

[304] Miller, K.L., F. Alfaro-Almagro, N. Bangerter, D. Thomas, E. Yacoub, J. Xu, A. Bartsch, S. Jbabdi, S. Sotiropoulos, J. Andersson *et al.*, "Multimodal population brain imaging in the uk biobank prospective epidemiological study," *Nat. Neurosci.*, vol. 19, no. 11, p. 1523, 2016.

[305] J. Clauser, M. S. Knieps, M. Büsen, A. Ding, T. Schmitz-Rode, U. Steinseifer, J. Arens, and G. Cattaneo, "A novel plasma-based fluid for particle image velocimetry (PIV): In-vitro feasibility study of flow diverter effects in aneurysm model," *Ann. Biomed. Eng.*, vol. 46, no. 6, pp. 841–848, 2018.

[306] J. Cebral, E. Ollikainen, B. J. Chung, F. Mut, V. Sippola, B. R. Jahromi, R. Tulamo, J. Hernesniemi, M. Niemelä, A. Robertson *et al.*, "Flow conditions in the intracranial aneurysm lumen are associated with inflammation and degenerative changes of the aneurysm wall," *Am. J. Neuroradiol.*, vol. 38, no. 1, pp. 119–126, 2017.

Curriculum Vitae

Ali Sarrami Foroushani was born in 1988 in Esfahan (Isfahan), Iran. In 2011, he obtained a BSc degree in Chemical Engineering at the Isfahan University of Technology, Iran. His BSc dissertation focused on computational fluid dynamics simulation of pneumatic transport of particles under the supervision of Prof. Mohsen Nasr Esfahany. In 2011, he moved to Barcelona, Spain. In a 6-month stay in Barcelona, he attended some Erasmus Mundus Masters level courses in Computational Mechanics at the Polytechnic University of Catalonia. In 2014, he obtained a MSc degree in Chemical Engineering at the Isfahan University of Technology. He wrote his MSc thesis under the supervision of Prof. Mohsen Nasr Esfahany and Prof. Alejandro F. Frangi about computational simulation of blood flow in cerebral aneurysms. Afterwards, he joined the Centre for Computational Imaging and Simulation Technologies in Biomedicine (CISTIB) at The University of Sheffield, UK as a research assistant and began his PhD studies under the supervision of Prof. Alejandro Frangi and Dr. Toni Lassila. In CISTIB, Ali continued working on computational simulation of blood flow in cerebral aneurysms. Through his work, he has gained interest and expertise in computational fluid dynamics, statistical data analysis, uncertainty quantification in cardiovascular flow simulations, and medical device and thrombosis modelling.

Permissions and Authorisations

Alejandro Frangi, PhD, FIEEE
Professor of Biomedical Image Computing
Electronic & Electrical Engineering Department
University of Sheffield
Pam Liversidge Building, C04 Office
Mappin Street, S1 3JD Sheffield, UK
Email: a.frangi@sheffield.ac.uk

To whom it may concern

I, Prof. Alejandro F. Frangi, hereby authorise Ali Sarrami Foroushani with passport number (N95884016) to include all or portions of the publications listed below in any research thesis or dissertation that he writes. I also give him the right to make oral presentation of the listed publications and to include a summary and/or highlights of them in papers distributed at such presentations.

1) Sarrami-Foroushani, A.; Lassila, T.; Gooya, A.; Geers, A. G.; Frangi A. F., Uncertainty quantification of wall shear stress in intracranial aneurysms using a data-driven statistical model of systemic blood ow variability. Journal of Biomechanics 49(11): 3815-3823, 2016.
2) Sarrami-Foroushani, A.; Lassila, T.; Frangi A. F., Virtual endovascular treatment of intracranial aneurysms: models and uncertainty. Wiley Interdisciplinary Reviews: Systems Biology and Medicine 9(4): e1385, 2017.
3) Sarrami-Foroushani, A.; Lassila, T.; Hejazi, S. M.; Nagaraja, S.; Bacon A.; Frangi A. F., A computational model for prediction of clot platelet content in flow diverted intracranial aneurysms. Journal of Biomechanics, submitted, 2018.
4) Lassila, T.; Sarrami-Foroushani, A.; Hejazi, S. M.; Frangi A. F., Population-Specific Flow Modelling: Between/Within-Subject Variability in the Internal Carotid Arteries of Elderly Volunteers. Annals of Biomedical Engineering, submitted, 2018.
5) Sarrami-Foroushani, A.; Lassila, T.; Pozo J. M., Gooya, A.; Frangi A. F., Direct Estimation of Wall Shear Stress from Aneurysmal Morphology: A Statistical Approach. International Conference on Medical Image Computing and Computer-Assisted Intervention (MICCAI) pp. 201-209, 2016

I also confirm that Mr. Sarrami Foroushani was the primary contributor to the papers number 1, 2, 3 and 5 of the above list, including design and conduct of the reported research.

This also confirms that Mr. Sarrami Foroushani was the primary contributor to the portion of the paper number 4 from the above list, which he reused in chapter 5 of his PhD thesis. His contribution included design and conduct of the reported research.

Sincerely,

24 July 2018

Alejandro F. Frangi, Ph.D.

To whom it may concern,

I, Dr. Toni Lassila, with passport number (FP1543841) hereby authorise Ali Sarrami Foroushani with passport number (N95884016) to include all or portions of the publications listed below in any research thesis or dissertation that he writes. I also give him the right to make oral presentation of the listed publications and to include a summary and/or highlights of them in papers distributed at such presentations.

1) Sarrami-Foroushani, A.; Lassila, T.; Gooya, A.; Geers, A. G.; Frangi A. F., Uncertainty quantification of wall shear stress in intracranial aneurysms using a data-driven statistical model of systemic blood
ow variability. Journal of Biomechanics 49(11): 3815-3823, 2016.

2) Sarrami-Foroushani, A.; Lassila, T.; Frangi A. F., Virtual endovascular treatment of intracranial aneurysms: models and uncertainty. Wiley Interdisciplinary Reviews: Systems Biology and Medicine 9(4): e1385, 2017.

3) Sarrami-Foroushani, A.; Lassila, T.; Hejazi, S. M.; Nagaraja, S.; Bacon A.; Frangi A. F., A computational model for prediction of clot platelet content in flow diverted intracranial aneurysms. Journal of Biomechanics, submitted, 2018.

4) Lassila, T.; Sarrami-Foroushani, A.; Hejazi, S. M.; Frangi A. F., Population-Specific Flow Modelling: Between/Within-Subject Variability in the Internal Carotid Arteries of Elderly Volunteers. Annals of Biomedical Engineering, submitted, 2018.

5) Sarrami-Foroushani, A.; Lassila, T.; Pozo J. M., Gooya, A.; Frangi A. F., Direct Estimation of Wall Shear Stress from Aneurysmal Morphology: A Statistical Approach. International Conference on Medical Image Computing and Computer-Assisted Intervention (MICCAI) pp. 201-209, 2016

I also confirm that Mr. Sarrami Foroushani was the primary contributor to the papers number 1, 2, 3 and 5 of the above list, including design and conduct of the reported research.

This also confirms that Mr. Sarrami Foroushani was the primary contributor to the portion of the paper number 4 from the above list, which he reused in chapter 5 of his PhD thesis. His contribution included design and conduct of the reported research.

Sincerely,

23 July 2018
Dr. Toni Lassila
Research associate, D.Sc. (Tech.)
Computational Imaging & Simulation Technologies in Biomedicine
University of Sheffield
E-mail: t.lassila@sheffield.ac.uk

To whom it may concern,

I, Dr. Ali Gooya, with passport number (E960137274) hereby authorise Ali Sarrami Foroushani with passport number (N95884016) to include all or portions of the publications listed below in any research thesis or dissertation that he writes. I also give him the right to make oral presentation of the listed publications and to include a summary and/or highlights of them in papers distributed at such presentations.

1) Sarrami-Foroushani, A.; Lassila, T.; Gooya, A.; Geers, A. G.; Frangi A. F., Uncertainty quantification of wall shear stress in intracranial aneurysms using a data-driven statistical model of systemic blood
ow variability. Journal of Biomechanics 49(11): 3815-3823, 2016.

2) Sarrami-Foroushani, A.; Lassila, T.; Pozo J. M., Gooya, A.; Frangi A. F., Direct Estimation of Wall Shear Stress from Aneurysmal Morphology: A Statistical Approach. International Conference on Medical Image Computing and Computer-Assisted Intervention (MICCAI) pp. 201-209, 2016

I also confirm that Mr. Sarrami Foroushani was the primary contributor to the papers of the above list, including design and conduct of the reported research.

Sincerely,
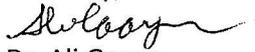
Al Gooya   23/07/2018

Dr. Ali Gooya,
Lecturer,
Department of Electronic and Electrical Engineering
The University of Sheffield
Email: a.gooya@sheffield.ac.uk

RightsLink®

Copyright Clearance Center

Journal of Biomechanics

Title: Uncertainty quantification of wall shear stress in intracranial aneurysms using a data-driven statistical model of systemic blood flow variability

Author: Ali Sarrami-Foroushani, Toni Lassila, Ali Gooya, Arjan J. Geers, Alejandro F. Frangi

Publication: Journal of Biomechanics

Publisher: Elsevier

Date: 8 December 2016

© 2016 Elsevier Ltd. All rights reserved.

LOGIN

If you're a copyright.com user, you can login to RightsLink using your copyright.com credentials.

Already a RightsLink user or want to learn more?

BACK | CLOSE WINDOW

JOHN WILEY AND SONS LICENSE
TERMS AND CONDITIONS

Jul 23, 2018

This Agreement between Mr. Ali Sarrami ("You") and John Wiley and Sons ("John Wiley and Sons") consists of your license details and the terms and conditions provided by John Wiley and Sons and Copyright Clearance Center.

License Number	4394620435751
License date	Jul 23, 2018
Licensed Content Publisher	John Wiley and Sons
Licensed Content Publication	Wiley Interdisciplinary Reviews: Systems Biology and Medicine
Licensed Content Title	Virtual endovascular treatment of intracranial aneurysms: models and uncertainty
Licensed Content Author	Ali Sarrami-Foroushani, Toni Lassila, Alejandro F. Frangi
Licensed Content Date	May 10, 2017
Licensed Content Volume	9
Licensed Content Issue	4
Licensed Content Pages	31
Type of use	Dissertation/Thesis
Requestor type	Author of this Wiley article
Format	Print and electronic
Portion	Full article
Will you be translating?	No
Title of your thesis / dissertation	In-silico clinical trials for assessment of intracranial flow diverters
Expected completion date	Jul 2018
Expected size (number of pages)	200
Requestor Location	Mr. Ali Sarrami-Foroushani Room C15, CISTIB Pam Liversidhe Building University of Sheffield Sheffield, South Yorkshire S1 3JD United Kingdom Attn: Mr. Ali Sarrami-Foroushani
Publisher Tax ID	EU826007151
Total	0.00 GBP
Terms and Conditions	

TERMS AND CONDITIONS

This copyrighted material is owned by or exclusively licensed to John Wiley & Sons, Inc. or one of its group companies (each a"Wiley Company") or handled on behalf of a society with which a Wiley Company has exclusive publishing rights in relation to a particular work (collectively "WILEY"). By clicking "accept" in connection with completing this licensing transaction, you agree that the following terms and conditions apply to this transaction (along with the billing and payment terms and conditions established by the Copyright Clearance Center Inc., ("CCC's Billing and Payment terms and conditions"), at the time that you opened your RightsLink account (these are available at any time at http://myaccount.copyright.com).

SPRINGER NATURE LICENSE
TERMS AND CONDITIONS

Jul 23, 2018

This Agreement between Mr. Ali Sarrami ("You") and Springer Nature ("Springer Nature") consists of your license details and the terms and conditions provided by Springer Nature and Copyright Clearance Center.

License Number	4394620827153
License date	Jul 23, 2018
Licensed Content Publisher	Springer Nature
Licensed Content Publication	Springer eBook
Licensed Content Title	Direct Estimation of Wall Shear Stress from Aneurysmal Morphology: A Statistical Approach
Licensed Content Author	Ali Sarrami-Foroushani, Toni Lassila, Jose M. Pozo et al
Licensed Content Date	Jan 1, 2016
Type of Use	Thesis/Dissertation
Requestor type	non-commercial (non-profit)
Format	print and electronic
Portion	full article/chapter
Will you be translating?	no
Circulation/distribution	<501
Author of this Springer Nature content	yes
Title	In-silico clinical trials for assessment of intracranial flow diverters
Instructor name	n/a
Institution name	n/a
Expected presentation date	Jul 2018
Requestor Location	Mr. Ali Sarrami-Foroushani Room C15, CISTIB Pam Liversidhe Building University of Sheffield Sheffield, South Yorkshire S1 3JD United Kingdom Attn: Mr. Ali Sarrami-Foroushani
Billing Type	Invoice
Billing Address	Mr. Ali Sarrami-Foroushani Room C15, CISTIB Pam Liversidhe Building University of Sheffield Sheffield, United Kingdom S1 3JD Attn: Mr. Ali Sarrami-Foroushani
Total	0.00 GBP

Terms and Conditions

Springer Nature Terms and Conditions for RightsLink Permissions
Springer Customer Service Centre GmbH (the Licensor) hereby grants you a non-exclusive, world-wide licence to reproduce the material and for the purpose and requirements specified in the attached copy of your order form, and for no other use, subject to the conditions below: